**DE-SC0005038**

9/1/10 - 5/31/17

**FINAL TECHNICAL REPORT**

# CRYSTALLIZATION AND THERMOELECTRIC TRANSPORT IN SEMICONDUCTOR MICRO- AND NANOSTRUCTURES UNDER EXTREME CONDITIONS

*Submitted August 30, 2017*

Ali Gokirmak
Helena Silva

University of Connecticut

## 1. Abstract

This project focused on thermoelectric transport in semiconductor micro and nanostructures where moderate and typical operating voltages and currents lead to extreme thermal gradients and current densities. Models that describe behavior of semiconducting materials typically assume an equilibrium condition or slight deviations from it. In these cases the generation-recombination processes are assumed to have reached a local equilibrium for a given temperature. Hence, free carrier concentrations and their mobilities, band-gap, thermal conductivity, thermoelectric properties, mobility of atoms and mechanical properties of the material, can be described as a function of temperature. In the case of PN junctions under electrical bias, carrier concentrations can change up to ~ $10^{20}$ $cm^{-3}$ and a drift-diffusion approximation is typically used to obtain the carrier concentrations while assuming that the material properties do not change.

In non-equilibrium conditions, the assumption that the material properties remain the same may not be valid. While the increased conduction-band electron concentration may not have a drastic effect on the material, large hole concentration is expected to soften the material as 'a hole' comes into existence as a broken bond in the lattice. As the hole density approaches $10^{22}$ $cm^{-3}$, the number of bonds holding the lattice together is significantly reduced, making it easier to break additional bonds, reduce band-gap and inhibit phonon transport. As these holes move away from where they were generated, local properties are expected to deviate significantly from the equilibrium case. Hence, temperature alone is not sufficient to describe the behavior of the material. The behavior of the solid material close to a molten region (liquid-solid interfaces) is also expected to deviate from the equilibrium case as a function of hole injection rate, which can be drastically increased or decreased in the presence of an electric field.

In the past years we have investigated the possible thermoelectric explanation of asymmetric melting of self-heated Si micro-structures using equilibrium materials' properties that exist in the literature. We have analyzed the contribution of the electrons and the holes and identified the generation-transport-recombination of minority carriers (GTR) as the reason for an extreme change in the thermal profile in presence of strong generation and electric field. A more complete analysis required construction of models that capture the individual generation and recombination processes to understand the thermal profile as well as the possibility of electronic softening and non-equilibrium melting of the structure below melting temperature. The possibility of melting a material at a lower temperature breaks the correlation between the atomic mobility and the kinetic energy in the system for a given temperature and may allow alternative growth processes. This may also be the mechanism behind 'amorphization-without-melting in layered structures heated with laser pulses' that has been reported earlier.

The conventional models for semiconductors are constructed for low temperature operation and their projections to higher temperatures do not yield reasonable carrier concentrations. Using these models, the free hole concentrations are calculated to be on the order of $10^{19}$ $cm^{-3}$ at melting, which also do not correlate well with the latent heat of fusion. The melt is expected to correspond to broken bond concentrations on the order of the atomic density (~$5x10^{22}$ $cm^{-3}$ for Silicon). Hence, using conventional models the thermoelectric contribution expected from the GTR process is estimated to be much smaller than it likely is. Our work focused on improving the computational models and electrical characterization of materials and devices to better understand thermoelectric trabsport under extremen thermal gradients and current densities. Specifically, during this project, we have

- Expanded our computational models to include self-consistent solution of Poisson charge equation (together with current and heat equations currently solved) for improved accuracy of role of bipolar conduction,
- Developed a crystallization model incorporating experimentally determined nucleation rates and growth velocities to enable simulation of grain growth, growth-from-melt, filament formation and retention,
- Performed high-temperature characterization of relevant materials (including metal contacts, interfacial and insulation layers); electrical and thermal conductivities, Seebeck coefficient, carrier mobility and concentration,
- Performed High-speed device-level characterization of metastable amorphous and crystalline phases, crystallization and amorphization dynamics, melting and crystalline growth-from-melt,
- Observed and characterized formation of microplasmas in electrically stressed ZnO nanoforests.

## 2. Award period 9/1/2010 to 3/1/2013

### *Crystallization and thermoelectric transport in Si micro-/nanostructures under extreme electrical stress*

### Summary of objectives and accomplishments

*Objectives*

**A.** To evaluate the possibility of using electrical pulses to achieve single crystal μ-structures with preferred crystal orientation from lithographically defined Si thin films deposited on arbitrary substrates.

**B.** To conduct research on thermoelectric phenomena in μ-/nano-structures under extreme conditions.

*Accomplishments*

- Experimental and computational analysis of high temperature thermoelectric phenomena that lead to significant asymmetric self-heating; *generation-transport-recombination of minority carriers* is the dominant process and results in the hottest spot shifted towards the drain of minority carriers,
- Extraction of high-temperature electrical resistivity and thermal conductivity of nano-crystalline (nc) Si up to high-temperatures and under extreme thermal gradients (up to ~ 1700 K, ~ 1 K/nm),
- Computational granularity models for percolation and nanoscale filament formation during self-heating;
- Analysis of crystallization of silicon micro/nano-structures through self-heating and impact of thermoelectric effects on crystallization (relative importance of Joule and thermoelectric heating),
- Development of high-temperature measurement setups for resistivity and Seebeck coefficient (~ 30 C - 600 C) and Hall carrier mobility and concentration (~ 30 C to ~ 450 C) for thin films,
- Application of electrothermal transport models to phase-change memory devices,
- Training of students in experimental and computational methods related to crystallization and electro-thermal transport at small scales.

### High-temperature thermoelectric transport at small scales

Electrothermal phenomena have been typically studied in the context of thermoelectric energy conversion or solid-state cooling using large-scale devices, and electronic transport at small-scales has been mostly studied in the lower temperature range (< 400 K) where the behavior of the charge carriers can be understood by examining the potential energy profiles. Thermoelectric studies at high-temperatures (~1000

K), where the thermal energy of the carriers in semiconductors becomes comparable to their potential energy, and at small scales which lead to extreme thermal gradients (> 1 K/nm) and uncommon electrothermal phenomena, have been limited due to difficulties in performing controlled experiments. We have shown the significance of thermoelectric effects for high-temperature small-scale electronics through self-heating of current-carrying highly-doped silicon micro-wires which consistently start melting at one end.

The experiments were performed with highly doped ($n$ ~ 6 x$10^{19}$ cm$^{-3}$) silicon microwires self-heated to very high temperatures (up to melting, ~ 1690 K). These wires with large contact extensions were lithographically defined and the underlying $SiO_2$ layer was partially removed, suspending the wires between the contact-extensions anchored to the substrate. Tungsten probes were used to make electrical contact at these large extension regions. Extremely asymmetric partial melting of these symmetric nc-Si wires is observed for voltage levels and durations that are not sufficient to melt the whole wires. Melting is consistently observed closer to the lower potential end, where the electrons (majority carriers) enter the wires. We attribute this extreme asymmetry to thermoelectric effects that come into play due to extreme thermal gradients during self-heating (~1 K/nm). The polarity of the asymmetry – hottest point is where the majority charge carriers enter the wire – is in agreement with our optical observations of asymmetric self-heating in *n-* and *p-type* silicon wires as well as with observations by other groups on silicon micro-structures and PCM nano-bridges, all attributed to thermoelectric Thomson heat. However, there has been very little or no explanation in the literature for the underlying physical phenomena giving rise to this asymmetry, largely due to difficulties in performing reliable and repeatable measurements at elevated temperatures. The surprisingly large degree of asymmetry seen in these results point to interesting physical phenomena that take place in highly doped semiconductors experiencing high temperatures and strong thermal gradients as a result of self-heating that are distinctly different from what is expected of metals. The polarity in the thermal profile is expected to be opposite if the self-heated wires were composed of a metal.

In order to understand the electro-thermal phenomena in these self-heated microwires, we have revisited the general formulations for electrical and thermal transport in current carrying structures and commonly known thermoelectric effects.

The thermoelectric effects, Seebeck and Peltier effects at junctions of two different materials, and Thomson effect (heat) in uniform materials experiencing a thermal gradient, are the results of the energy exchange between the charge carriers and the lattice in presence of an electric current. The average energy of a charge carrier, or the magnitude of the Peltier coefficient $\Pi(T)$, is the product of the Seebeck coefficient $S(T)$ of the material and the local temperature. Strong $\Pi(T)$ gradients lead to increased energy exchange as the carriers move along the temperature gradient (large Thomson effect).

The electrical current density can be expressed as the sum of drift and diffusion components using a drift-diffusion model: $J = J_{Drift} + J_{Diff}$. The drift current is due to the electric field acting on the carriers and the diffusion current comes into existence due to gradients in carrier concentrations and their velocities (diffusivities, $D$). The general forms (in linear approximation) for these components are:

$$J_{Drift} = \sigma E\ ,\ J_{Diff} = q\nabla(Dn) \qquad (0a),$$

where $\sigma$ is electrical conductivity, $E$ is the electric field and $n$ is the carrier concentration. In the case of constant temperature (or small variations in T), hence an approximately constant $D$, diffusion current takes the more recognizable form of $J_{Diff} = qD\nabla n$. However, in our case the thermal gradients are very strong

and *D(T)* cannot be assumed to be constant across the device. The individual components of the diffusion current can be formulated by expansion:

$$J_{Diff} = q\nabla Dn = qn\nabla D + qD\nabla n \tag{0b}$$

Additionally, if the material is uniform (as in our case), temperature is the only driver for gradients of carrier concentration *n(T)* and gradients of *D(T)*. Hence the diffusion current can be rewritten in terms of temperature derivatives and thermal gradients:

$$J_{Diff} = qn\frac{dD}{dT}\nabla T + qD\frac{dn}{dT}\nabla T = q(n\frac{dD}{dT} + D\frac{dn}{dT})\nabla T \tag{0c}$$

This expression describes the diffusion current as a function of gradient of temperature, assuming that the material is uniform (using an effective media approximation with no variations in doping concentration, composition or crystallinity). In an open-circuit case ($J$ = 0), the drift and the diffusion currents are balanced, resulting in an open-circuit electric field driven by the thermal gradient:

$$J_{Drift} + J_{Diff} = \sigma E + q(n\frac{dD}{dT} + D\frac{dn}{dT})\nabla T = 0$$

$$\sigma E = -\sigma\nabla V = -q(n\frac{dD}{dT} + D\frac{dn}{dT})\nabla T \tag{0d}$$

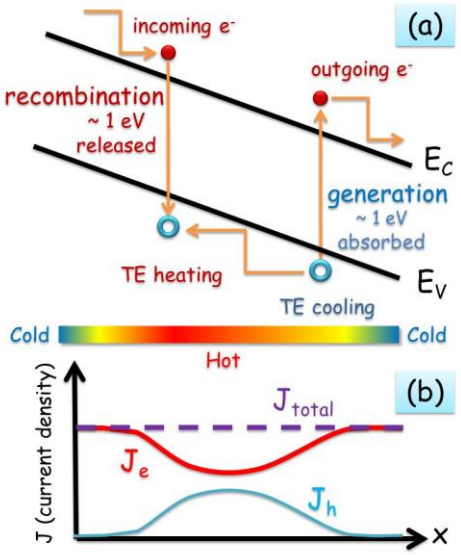


**Figure 1.** A simplified illustration of the generation-transport-recombination concept and the electron and hole contributions to current flow. (a) A generation event on the right side gives rise to a hole that is drifted to left where it recombines with an incoming electron. Generation takes place with absorption of energy from the local area while recombination leads to energy release. (b) The total current remains constant. The increased hole current contribution in the hot regions leads to reduced electron current.

The voltage ($\Delta V$) generated by a difference in temperature ($\Delta T$) is the definition of Seebeck voltage and their ratio is defined as the Seebeck coefficient ($S$):

$$-\frac{\nabla V}{\nabla T} = -\frac{q}{\sigma}(n\frac{dD}{dT} + D\frac{dn}{dT}) = -\frac{\Delta V}{\Delta T} = S \tag{0e}$$

Hence the diffusion expression can be written in terms of Seebeck coefficient as

$$J_{Diff} = -\sigma S\nabla T \tag{0f}$$

where experimental values can be used for $S$. Assuming steady state (current continuity), charge transport including the thermoelectric contribution for a uniform material can be described by:

$$\nabla \cdot J = \nabla \cdot (-\sigma\nabla V - \sigma S\nabla T) = 0 \tag{1}$$

Temperature changes can be modeled by accounting for heat generation by joule heating (energy loss from the charge carriers to the lattice), and heat flow by thermal conduction and by charge carriers:

$$\underbrace{d\,C_P\frac{dT}{dt}}_{\text{heat absorbed by lattice}} - \underbrace{\nabla\cdot(k\nabla T)}_{\text{heat loss through conduction}} = \underbrace{-\nabla V\cdot J}_{\text{Joule heating}} - \underbrace{\nabla\cdot(JST)}_{\text{Thermoelectric heat release}} \qquad (2),$$

where $d$ is the mass density, $C_P$ is the specific heat, and $k$ is the thermal conductivity and $ST=\Pi$ is the average energy per charge carrier. The thermoelectric term describing energy flow by charge carriers can be broken down as the specific electron and hole contributions:

$$\nabla\cdot(JST) = \nabla\cdot(J_eS_eT + J_hS_hT)$$
$$= \left[J_e\cdot\nabla(S_eT) + J_h\cdot\nabla(S_hT) + S_eT\nabla\cdot J_e + S_hT\nabla\cdot J_h\right]\cdot \qquad (3a)$$

Since each generation event results in one electron and one hole, and the total electrical current is constant (Figure 1), $\nabla\cdot J_e = -\nabla\cdot J_h$, allowing us to rearrange the terms for a more intuitive expression where *electronic convective heat flow* and *generation-transport-recombination (GTR)* terms appear as the two components of thermoelectric energy flow in the structure:

$$\underbrace{\nabla\cdot(JST)}_{\text{heat transfer between carriers and lattice}} = \underbrace{\underbrace{J_e\cdot\nabla(S_eT)}_{\text{convective heat flow by e}^-} + \underbrace{J_h\cdot\nabla(S_hT)}_{\text{convective heat flow by holes}}}_{\textit{electronic-convective}} + \underbrace{\underbrace{(\nabla\cdot J_h)}_{\text{local gen. rate}}\underbrace{(S_hT - S_eT)}_{\text{energy of an e}^-\text{ - hole}^+\text{ pair}}}_{\textit{generation-transport-recombination}} \qquad (4)$$

The electronic convective term is purely due to carriers moving in a thermal profile exchanging energy with the surrounding. The *GTR* term is due to energy absorption associated with electron-hole pair generation (breaking of chemical bonds and bringing these electrons and the holes to the average local kinetic energy), separation of those carriers by the electric field and their recombination elsewhere (Figure 1). While generation and recombination take place in the whole structure, generation rate is a strong function of temperature and the recombination is limited by availability of minority carriers.

## Finite element simulations & materials parameters

We have performed 3D finite element simulations of $n^+$ nc-Si wires solving (1) and (2) self-consistently using temperature dependent materials properties (Figure 2) and compared them to the experimental results (Figure 3a-d). In these simulations, we assume that the charge carriers remain in local thermal equilibrium with the lattice ($T_{electron} = T_{lattice}$) and use an effective medium approximation, neglecting the impact of individual grain boundaries. The thermal boundary conditions are set as 300 K at the bottom of the Si substrate and on the 1 µm radius metal contacts that are used to model the probes placed ~50 µm away from the wire ends. The Si latent heat of fusion during the solid-to-liquid phase transition is accounted for by incorporating a 10 K wide peak in $C_p$ around melting temperature where all the material parameters linearly transition to their liquid-state values. The liquid state values $\rho_{liquid}$, $k_{liquid}$ and $S_{liquid}$ are obtained from the literature. *ρ, k and S* of nanocrystalline thin films depend on deposition conditions and are not easy to measure directly at elevated temperatures.

We have measured *ρ(T)* and *S(T)* simultaneously in the 300 - 650 K range – using the high-temperature Seebeck setup developed as a part of this project (described in a later section) - and extracted *k(T)* in this range by using the measured *ρ(T)* and matching simulated and experimental I-V curves. We

have extracted *ρ(T)* beyond 650 K using the same approach by extrapolating *k(T)*. This method effectively accounts for the expected reduction in *k(T)* due to ballistic or non-local transport under extreme thermal gradients and is described in the next section. *S(T)* beyond 650 K is extrapolated based on calculations for single-crystal silicon (x-Si) using the Boltzmann transport model and Fermi-Dirac statistics. Figure 2 shows all the physical parameters used in the simulations, including the measured *ρ(T), S(T)* and extracted *k(T)*. Details on the calculations of carrier concentrations *n* and *p* for calculation of *S(T)* beyond 650 K based on Boltzmann transport can be found in Ref.

The voltage pulse amplitudes in the simulations (25 V) in Figure 3 are chosen so that the experimental and simulated current density levels are matched ($J$ ~ 3.5 MA/cm$^2$, experimental $V_{pulse}$ = 30 V). The simulation results show melting of approximately half of a 2.5 µm long wire at the source for majority carriers (lower potential) side for 1 µs pulses, in agreement with the experiments, the experimental asymmetry being stronger (Figure 3a-d). The charge carriers transport energy in their flow directions, which increases with temperature for electrons ($TS_e$) and decreases for holes ($TS_h$) as the Fermi level approaches mid-gap and the band-gap shrinks (Figure 3e,f). On the other hand, the minority carrier concentration increases exponentially with temperature. Hence, the net energy transported by the charge carriers ($TS_e\ \sigma_e/\sigma + TS_h\ \sigma_h/\sigma$) sharply decreases as the material turns intrinsic, diminishing to metallic values upon melting (Si $T_{melt}$ = 1690 K). The contribution of the minority carriers becomes significant at elevated temperatures

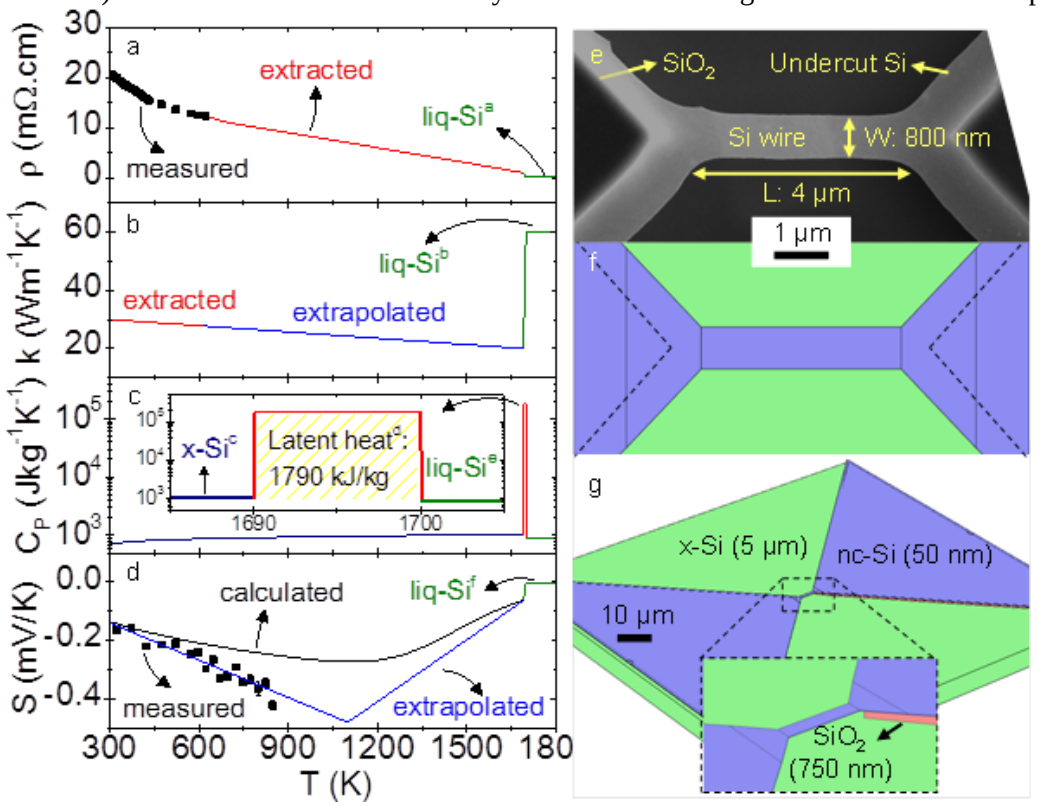


**Figure 2.** Temperature dependent physical parameters used for the modeling: (a) Measured and extracted electrical resistivity ($\rho$) of the nc-Si film. Liquid silicon (liq-Si) resistivity from Ref. (b) Extracted and extrapolated thermal conductivity ($k$) of the nc-Si wires. Liq-Si value of $k$ from Ref. (c) Heat capacity of crystalline silicon (x-Si) under constant pressure ($C_P$), from Ref., liq-Si value of $C_P$ is obtained from Ref. (d) Calculated (for n-type x-Si, 6x10$^{19}$ cm$^{-3}$), measured (n+ nc-Si film) and extrapolated Seebeck curve. Liq-Si value of $S$ from Ref. (e) SEM image of an as-fabricated suspended nc-Si wire with indicated dimensions. Lighter color regions show where the underlying oxide is removed. (f, g) Structure drawn for the simulations. Electrical contacts are at the end of the triangular pads.

for highly doped semiconductors (at ~ 1300 K for *n*-Si with $[N_D] = 6x10^{19}$ cm$^{-3}$). Moreover, significant reduction of the band-gap with increasing temperature exacerbates thermal generation of electron-hole pairs, leading to a considerable distortion in the conduction and valance band edges in presence of a strong thermal gradient (up to 1 K/nm). Individual contributions of the *electronic-convective* heat flow by electrons and holes are in the same direction (energy release at the higher potential end) and are opposed by the *GTR* term (Figure 3g,h).

It is not possible to obtain thermal profile information in these microstructures in µs time scales to compare experimental and simulated profiles. Therefore, we have performed experiments on *n*- and *p-type* microwires (Figure 4) using lower amplitude, low frequency AC signals (~1 Hz, $J \sim 1$ MA/cm$^2$) which heat the wires sufficiently to result in observable black-body radiation in visible range but without melting or breaking (Figure 4). The emitted light is captured using a commercial digital camera mounted on a microscope objective to obtain emission profiles of the structures. The use of AC signals allows verification of structural integrity and consistency in repeated cycles, and eliminates the uncertainty in hottest spot location with respect to the wire center. The glow is more intense close to the terminal where the majority carriers enter the wire for both *n*- and *p-type* wires – in agreement with the pulse experiments and simulations. Simulated thermal profiles (for $T_{peak}$ = 1640 K) for an *n-type* wire are used to calculate the

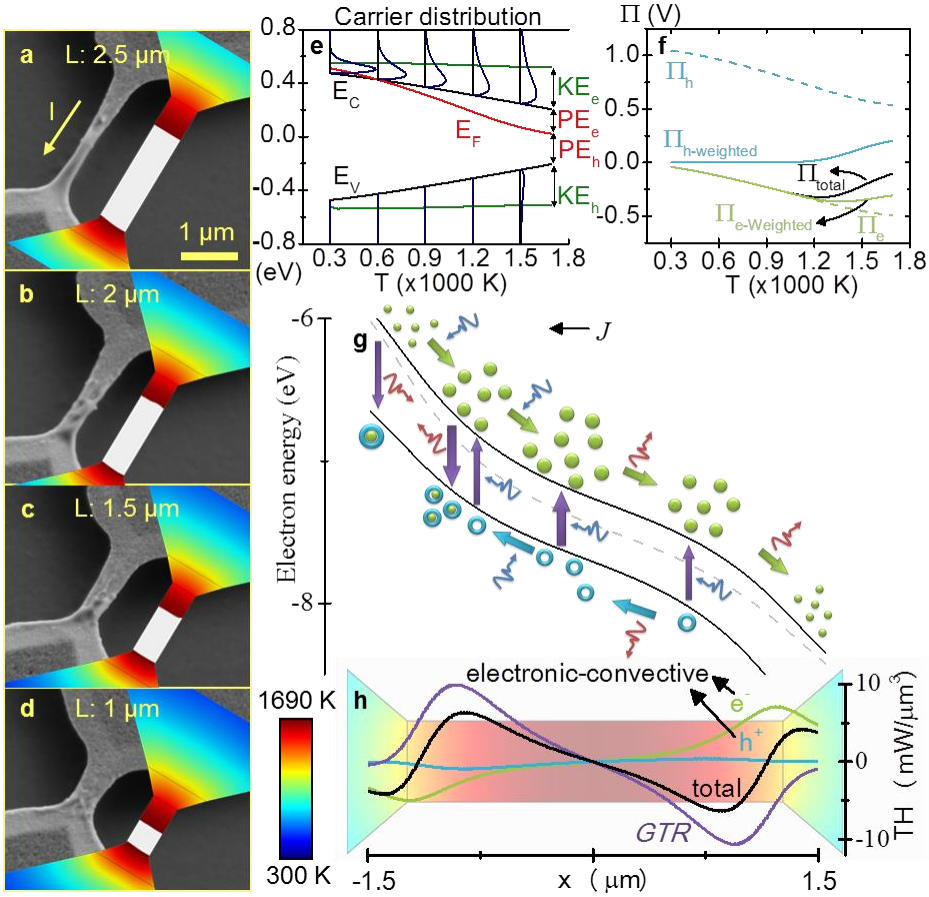


Figure 3. (a-d) Partially crystallized wires with indicated lengths after 30 V, 1 µs pulse, and corresponding simulated temperature profiles (white > $T_{melt}$ = 1690 K). The current direction is indicated in (a). (e) Calculated energy-band diagram of $6x10^{19}$ cm$^{-3}$ doped n-type Si with electron and hole distributions from 300 to 1500 K. (f) Calculated electron, hole (both unweighted and weighted) and total Peltier coefficients (sum of weighted $\Pi_h$ and $\Pi_e$). (g) Cartoon illustration of carrier generation, transport and recombination (*GTR*), and energy exchange with lattice for a hypothetical wire with initially symmetric temperature profile. (h) Breakdown of thermoelectric heat (TH) leading to asymmetric melting: convective transport by electrons, by holes, and *GTR* of holes.

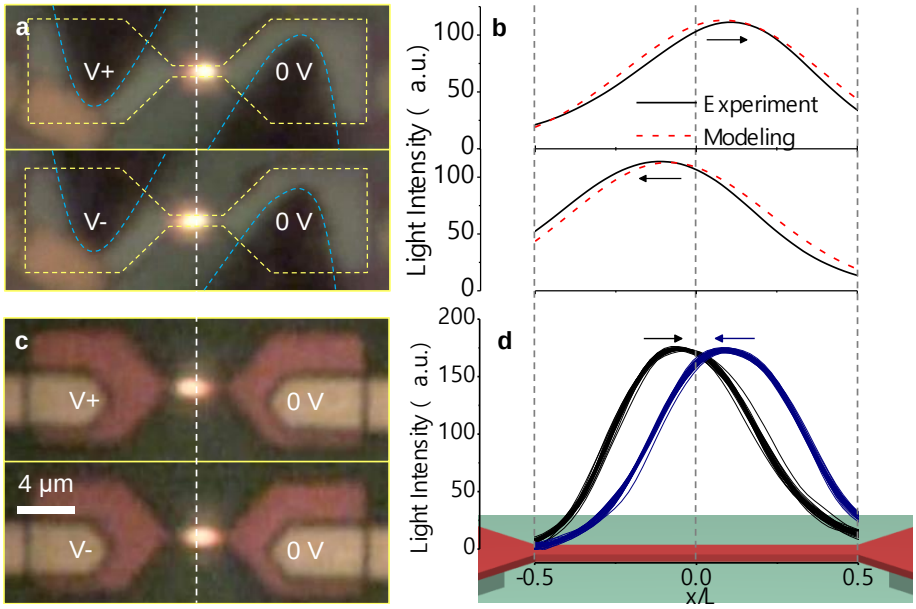


**Figure 4.** (a) Optical images of a 2.5 µm long, suspended, *n-type* wire biased with shown current levels and directions. Dashed lines indicate the edges the Si structures and metal probes. (b) Averaged light intensity profiles along the *n-type* wire for each direction of current compared to simulated light intensity profiles. (c) Optical images of a 4 µm long, suspended, *p-type* wire. (d) Light intensity profiles along the *p-type* wire for both direction of current (30 curves per polarity). Arrows indicate current directions. Vertical dashed lines show wire center and ends.

corresponding black-body radiation, assuming the wire consists of many small light sources with Gaussian profiles to model the diffraction limit of the optics used in the experimental setup. The simulated and experimental radiation intensity profiles are in good agreement, again with the observed experimental asymmetry being stronger (Figure 4).

To visualize the heat associated with the GTR process, the electric current is separated into its electron and hole components for an example simulation of self-heating of a 2.5 µm $n^+$ nc-Si wire during a microsecond pulse for the peak temperature of 1686 K (Figure 5a). The hole and electron current densities are found from the respective conductivities which are calculated from the experimental and extracted total conductivity function and the ratio of electron and hole conductivities obtained from the general expressions for conductivity based on the Boltzman transport equation.

The hole current density peaks at ~ 0.5 µm away from the lower potential end of the wire. The electron current density responds to the varying hole current to establish the constant total current density along the wire. Towards the ends of the wire, temperature decreases, lowering the contribution of the hole current to zero. The hole current density is further broken down into its drift and diffusion (thermoelectric) components in Figure 5b, showing that the hole current is dominated by the drift component:

$$J_h = \underbrace{\sigma_h E}_{J_{h-drift}} \underbrace{-\sigma_h S_h \nabla T}_{J_{h-TE}} \tag{5}$$

The net carrier generation rate is calculated as the divergence of the hole current density and plotted together with hole carrier density along the wire in Figure 5c.

$$\frac{\nabla \cdot J_h}{q} = -\frac{\nabla \cdot J_e}{q} = \text{net generation rate} \qquad (6)$$

Net generation (cooling) occurs along most of the wire starting ~ 0.5 μm from the lower potential end, while stronger net recombination (heating) occurs within a shorter distance around the lower potential end of the wire. This GTR heat is the dominant thermoelectric contribution and determines the overall asymmetry polarity *as the hottest spot shifted towards the drain for minority carriers*.

The model used so far (Eqs. 1 and 2) includes drift and diffusion (thermoelectric) currents but assumes charge neutrality, which is not very accurate due to some charge separation and build-in fields under thermal gradients (thermoelectric effects). This effect is relatively small (~ 100 mV for a 1000K thermal gradient along a 1 μm of Si wire) compared to the external voltages applied for self-heating (~ 10 V/μm). However, it is expected to affect drift and recombination of minority carriers which play a critical role in the GTR contribution to the thermoelectric heat and charge buildup in time. In the existing model, carrier densities are calculated based on the temperature using Fermi-Dirac statistics and assuming charge neutrality. This modeling approach is commonly used for single material systems with a strongly dominant single carrier type (electrons or holes). Poisson equation must also be solved in a self-consistent manner with the drift-diffusion current and heat models to account for charging along the structures (Figure 6).

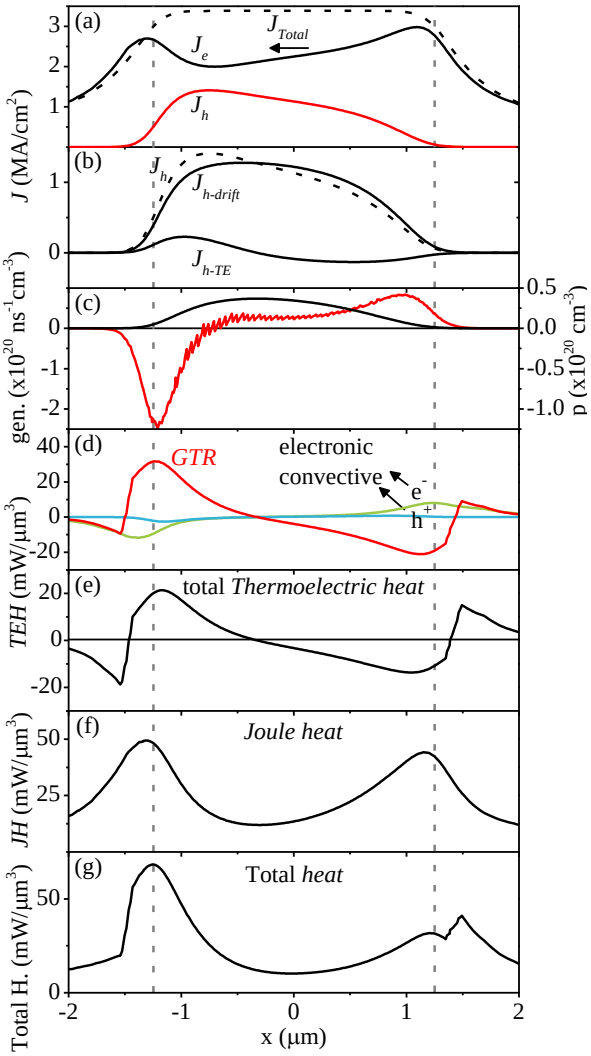


**Figure 5.** Simulation results along a 2.5 μm long wire for the peak temperature of 1686 K: (a) Total current ($J_{Total}$) density and its electron ($J_e$) and hole ($J_h$) components, (b) breakdown of the hole current into drift ($J_{h\text{-}drift}$) and diffusion ($J_{h\text{-}TE}$) components, (c) net carrier generation rate per ns and hole carrier density (p), (d) breakdown of thermoelectric heat (*TEH*) in to *GTR* and electronic convective heat components, (e) total *TEH*, (f) Joule heat (*JH*), (b) total heat dissipation (sum of Joule and thermoelectric heat).

In our existing model, we also neglect the directionality of momentum transfer between charge carriers and phonons (phonon-drag) typically observed at low temperatures (< 100 K) and low doping levels. We have estimated the phonon-drag contribution on Seebeck coefficient to be negligible using Herring's model. Under extreme thermal gradients, however, phonon-drag may also result in reduced thermal and electrical conductivity at the source side of the wire where incoming majority carriers scatter phonons back into the wire (reduced $k_{phonon}$) and lose momentum (reduced $\sigma$), leading to increased heating. Similarly, thermal and electrical conductivity would be enhanced at the opposite end as phonons and majority carriers travel in the same direction and tend to forward-scatter each other. The resulting increase

in Joule heating and reduced thermal conductivity at the source side for majority carriers (and decrease in Joule heating and increased thermal conductivity at the other side) are also expected to contribute to the asymmetry in heating.

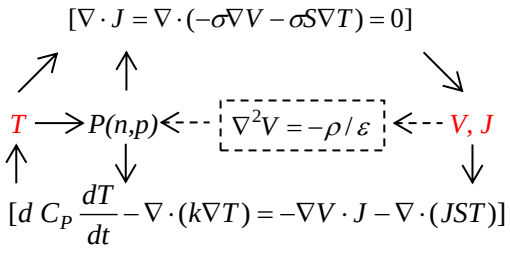


**Figure 6.** Current model equations (in solid lines) and missing link between V, J and n/p (Poisson equation, in dashed lines) that will be included in the next model for more accurate calculations.

The small but noticeable discrepancy between the simulations and the experiments may also be explainable by other second order effects such as electron-hole generation and scattering at the grain boundaries and non-linear thermoelectric transport which is expected to become significant at thermal gradients ≥ 1 K/nm. Carrier generation and recombination at the defect sites at the grain boundaries is expected to result in increased minority carrier concentration and reduced minority carrier lifetimes. Grain boundary scattering is also expected to be different for electrons and holes which will impact carrier and thermoelectric transport characteristics. Non-linear contributions are expected to enhance thermoelectric transport.

## Extraction of temperature dependent electrical resistivity and thermal conductivity under extreme thermal gradients

We have extracted *ρ(T)* and *k(T)* of nanocrystalline silicon (nc-Si) microwires up to melting temperature by matching numerically simulated *I-V* characteristics to experimental *I-V* characteristics. The simulated *I-V* characteristics are obtained using numerical modeling described above. A similar method was used recently by Pop et al.[1] to extract thermal conductance (up to ~ 800 K) of a suspended single-wall carbon nanotube by matching modeled and measured *I-V* characteristics for different substrate temperatures. Earlier, Tai et al.[2] had extracted a constant *k* as the only fitting parameter to match approximated analytical *I-V* expressions to experimental *I-V* curves.

In our extraction of *ρ(T)* and *k(T)* of silicon wires, two example cases are considered: 1) Extraction of *ρ(T)* from highly-doped p-type wires on silicon dioxide in which the heat losses are predominantly to the substrate and the self-heating characteristics depend mainly on *ρ(T)* of the wires and 2) extraction of both *ρ(T)* and *k(T)* from suspended highly-doped n-type silicon wires in which the heat losses are predominantly through the wires and both *ρ(T)* and *k(T)* are important in the self-heating process. If both non-suspended and suspended wires made of the same material were available, *ρ(T)* and *k(T)* could be extracted independently from different experimental *I-V* characteristics: *ρ(T)* could be extracted from a non-suspended wire *I-V* assuming a constant *k* and this *ρ(T)* could then be used to extract *k(T)* from a suspended wire *I-V*. *This technique allows for extraction of electrical resistivity and thermal conductivity up to very high temperatures (1690 K for Si) and temperature gradients (~ 1 K/nm) which is not possible, or very difficult to achieve otherwise.* Details on the device fabrication, experiments and simulations can be found in Ref.[3].

*Extraction of Electrical Resistivity for Silicon Wires on Oxide*: Figure 7b shows experimental *I-V* curves of two different wires on oxide with similar dimensions (L: 15 µm, W: 1.43 µm) together with the matched simulated *I-V* curve (for the *ρ(T)* extraction) using a constant *k* value of 30 $Wm^{-1}K^{-1}$. The experimental *I-V* curves show similar trends up to high voltage levels, however they split at high temperatures despite their similar dimensions, possibly due to different geometry changes (e.g., cracking, formation of voids) that happen close to melting. Plotted in the same graph are two additional simulated *I-V* curves using the extracted *ρ(T)* and two constant *k* values of 10 and 50 $Wm^{-1}K^{-1}$. The simulated *I-V* curves using all three *k* values (10, 30, 50 $Wm^{-1}K^{-1}$) are identical up to very high voltage/temperature levels, verifying the assumption that wire *k* affects self-heating of the wires on oxide only slightly. The extracted *ρ(T)* is tested by modeling three other wires on oxide with different dimensions (using the same constant *k* of 30 $Wm^{-1}K^{-1}$) (Figure 7d-e).

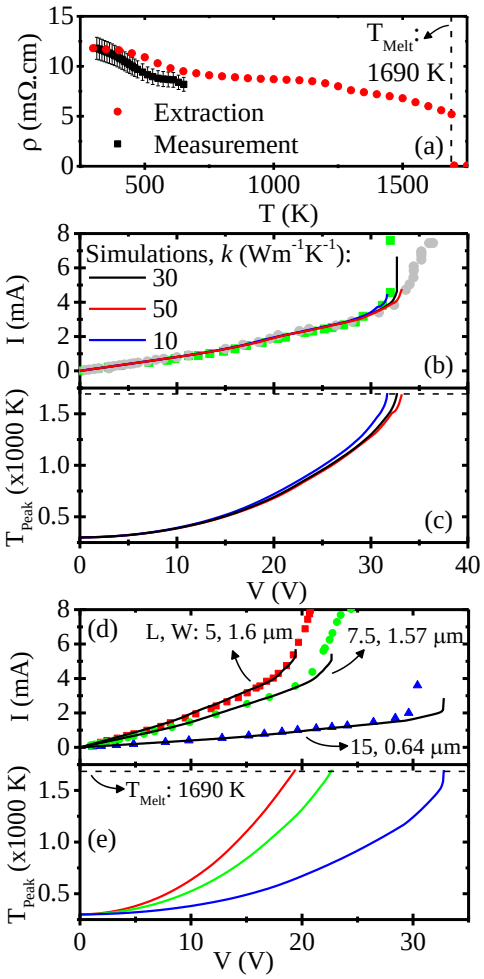


**Figure 7.** (a) Extracted and measured *ρ(T)* for the wire on oxide. (b) Experimental *I-V* curves (symbols: ■, ●) of p-type nc-Si wires on oxide with similar dimensions (L: 15 µm, W: 1.43 µm) and matched simulated I-V curve (black line) to extract *ρ(T)* for *k*: 30 $Wm^{-1}K^{-1}$. Simulated *I-V* curves for *k*: 10 (blue line) and 50 $Wm^{-1}K^{-1}$ (red line) using the extracted *ρ(T)*. (c) Simulated peak temperatures on the wire as functions of voltage for the indicated constant k values. Horizontal dashed line indicates the melting temperature level. (d) Experimental (symbols) and simulated (black lines) *I-V* curves of three p-type wires on oxide with shown dimensions using the extracted *ρ(T)* and constant *k* of 30 $Wm^{-1}K^{-1}$. (e) Simulated peak temperatures on the wires.

*Extraction of Electrical Resistivity and Thermal Conductivity for Suspended Silicon Wires*: For the suspended silicon wires the heat losses are predominantly toward the large contact pads through the wires, and the wire *k* becomes important. We extract *k(T)* in the temperature range for which measured *ρ(T)* is available (300 - 620 K for this case) by matching simulated to experimental *I-V* curves (Figure 8) and extrapolate it up to melting temperature (1690 K). *ρ(T)* is extracted from 620 to 1690 K using the extrapolated *k(T)*.

Figure 8c-d show the measured and extracted *ρ(T)* and the extracted and extrapolated *k(T)* for the entire temperature range. The extracted *k(T)* is compared to values for bulk x-Si, thin-film poly-Si and bulk nano-structured silicon (nb-Si). The extracted *k(T)* is in between the values reported for highly-doped ($n \sim 2x10^{20}$ $cm^{-3}$) polycrystalline silicon (poly-Si) (t < 300 nm) at low temperatures, and the extrapolated *k(T)* approaches the x-Si value at high temperatures. The modeling of the suspended wire is also performed using the same parameters (Figure 8c-d). The measured/extracted *ρ(T)* and extracted-extrapolated *k(T)* are tested by modeling another suspended wire (WxL: 840nm x 4µm) (Figure 9).

The experimental and simulated *I-V* curves are in good agreement indicating the extracted temperature-dependent parameters are close to the actual ones. The small discrepancies between the experimental and simulations results are attributed to the unknown exact location of the electrical contacts in the experiments and physical phenomena that are expected to become more important at high temperatures such as temperature dependent physical parameters of $SiO_2$, thermal

boundary resistances, or physical changes of the wires. The use of integrated metal contacts on the silicon pads for well-defined location of the electrical boundaries will improve the extraction process. Suspended wires are less susceptible to physical changes at high temperatures due to reduced mechanical stress (the temperature on wires on oxide is more uniform leading to stronger thermal gradients at the ends). The use of suspended wires also eliminates the need for temperature dependent parameters of silicon dioxide or thermal boundary resistance in the modeling.

Experimental values for electrical resistivity and thermal conductivity can be used for the low temperature range, as available experimentally, and would lead to more accurate extraction of these parameters at the high temperatures (as shown for extraction of thermal conductivity from suspended wires). The iterative matching of experimental and simulated I-V characteristics is a time consuming process.

This method can be applied to extract electrical resistivity and thermal conductivity up to very high temperatures of any micro/nano-scale structure which can be self-heated while preserving its geometry. The extracted parameters under these conditions reflect any effects that may arise due to the large temperature gradients (~ 1 K/nm for the Si wire case presented here).

## Percolation transport and filament formation in nanocrystalline silicon nanowires

During rapid self-heating, melting, and growth from melt using microsecond voltage pulses, electron percolation along a preferred path in nc-Si leads to rapid self-heating and the formation of a highly conductive, molten filament (Figure 10d). Filament formation leads to fast melting (and fast crystallization) in nc-Si, but localized crystallization of randomly determined pathways may lead to inconsistent crystallization as sample size increases. Percolation transport is very significant in all nanocomposite devices intended for electronics applications including resistive memory technologies and in spark-plasma sintering of nanoparticles to form nanocrystalline-bulk materials such as nanobulk Si intended for thermoelectric applications. We have performed 2-D simulations to model the evolution of current-induced filaments in nc-Si nanowires during fast pulses.

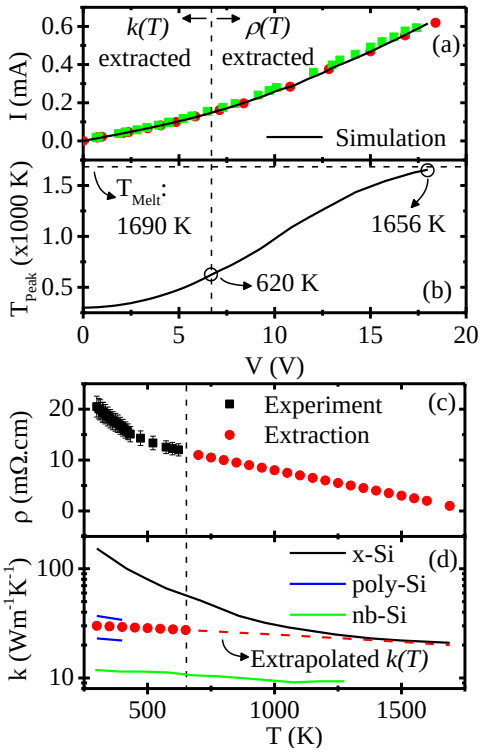


**Figure 8.** (a) Experimental *I-V* curves (symbols: ■, ●) of two suspended n-type nc-Si wires of similar dimensions (L: 5 µm, W: 0.9 µm), and matched simulated *I-V* curve (black line) for the extraction of *ρ(T)* and *k(T)*. (b) Simulated peak temperature on the wire. (c) Measured and extracted *ρ(T)* for the suspended wire. (d) Extracted and extrapolated *k(T)* for the suspended wire and experimental results from the literature for bulk x-Si[90], two highly-doped poly-Si films[91] and nano-bulk Si[92].

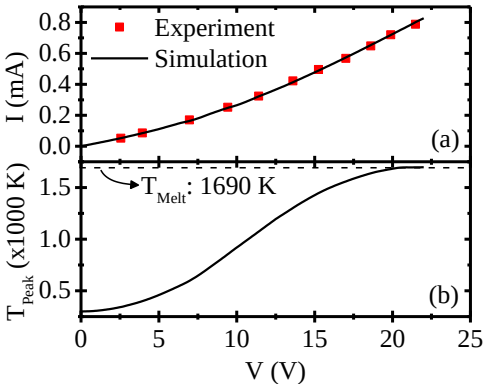


**Figure 9.** (a) Experimental *I-V* of a suspended n-type nc-Si wire (L: 4 µm, W: 840 nm) compared to the simulated *I-V* using *ρ(T)* and *k(T)* extracted from a different wire *I-V* (shown in Figure 8c-d). (b) Simulated peak temperature on the wire.

nc-Si material is modeled as c-Si grains randomly distributed within an a-Si matrix. Random distributions of circular grains are generated using MATLAB (random 'nucleation' followed by a 'crystal growth' algorithm) and imported into COMSOL Multiphysics to solve the current continuity and the heat transfer equations self-consistently. Simulations include temperature dependent material parameters for specific heat ($C_P$), thermal conductivity (κ), and electrical resistivity ($\rho$) for both a-Si and c-Si (Figure 10a,b). Temperature dependent electrical resistivity and thermal conductivity for heavily doped, n-type c-Si ([As] = $10^{19}$ $cm^{-3}$) are obtained from Synopsys Sentaurus TCAD suite. Latent heat during phase transition from solid to liquid Si is modeled as a ~1000 times increase in specific heat between 1687 and 1697 K (Figure 10c).

The amount of crystalline material per sample volume of nc-Si, or the fill factor, is varied between zero (totally amorphous) and one (totally crystalline). nc-Si nano-wires of various fill factors were generated using MATLAB and simulated in COMSOL to calculate the thin film resistivity values (Figure 10e). A maximum fill factor of 0.7 has been achieved using the nanocrystalline algorithm, which is used to generate the simulated nc-Si wires. A resistivity of 17.5 Ω·cm at 300 K was calculated for a simulated wire with 0.7 fill factor. An exponential fit to the data points of Figure 10e is used to extrapolate simulated resistivity values for large fill factors that are impractical to generate and simulate. A fill factor of 0.995 is required to match the measured resistivity of nc-Si wires (23 mΩ·cm) using this model which does not account for field dependent electrical breakdown.

The 2-D model of fabricated nc-Si wires (Figure 11a) includes a series load resistor to prevent current/thermal runaway during filament formation. Suspended wires are modeled to have electrically and thermally insulating boundaries whereas wires resting on $SiO_2$ are approximated by surrounding the Si wire

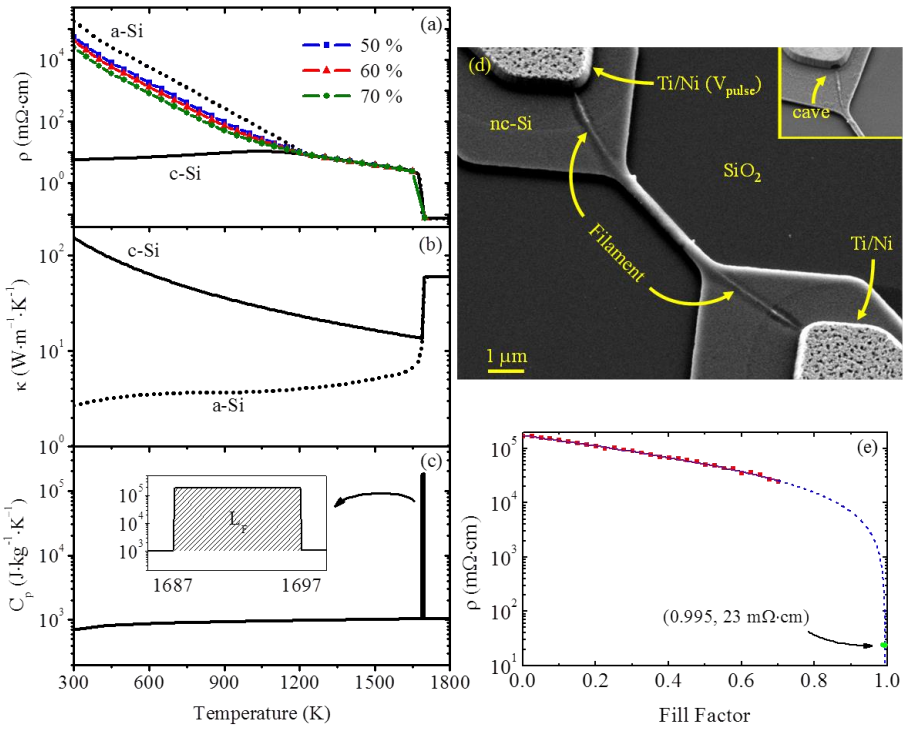


Figure 10. (a) Resistivity (b) thermal conductivity and (c) specific heat as a function of temperature for a-Si, c-Si, and nc-Si of various fill factors. (d) Percolation along a preferred path in nc-Si wires leads to rapid self-heating and the formation of a highly conductive, molten filament which crystallizes while cooling ($V_{pulse}$ ~15 V). (e) Simulated thin film resistivity as a function of fill factor (red squares) and first-order exponential fit to data (blue). Extrapolated curve indicates a fill factor of 0.995 required to match measured resistivity of 23 mΩ·cm.

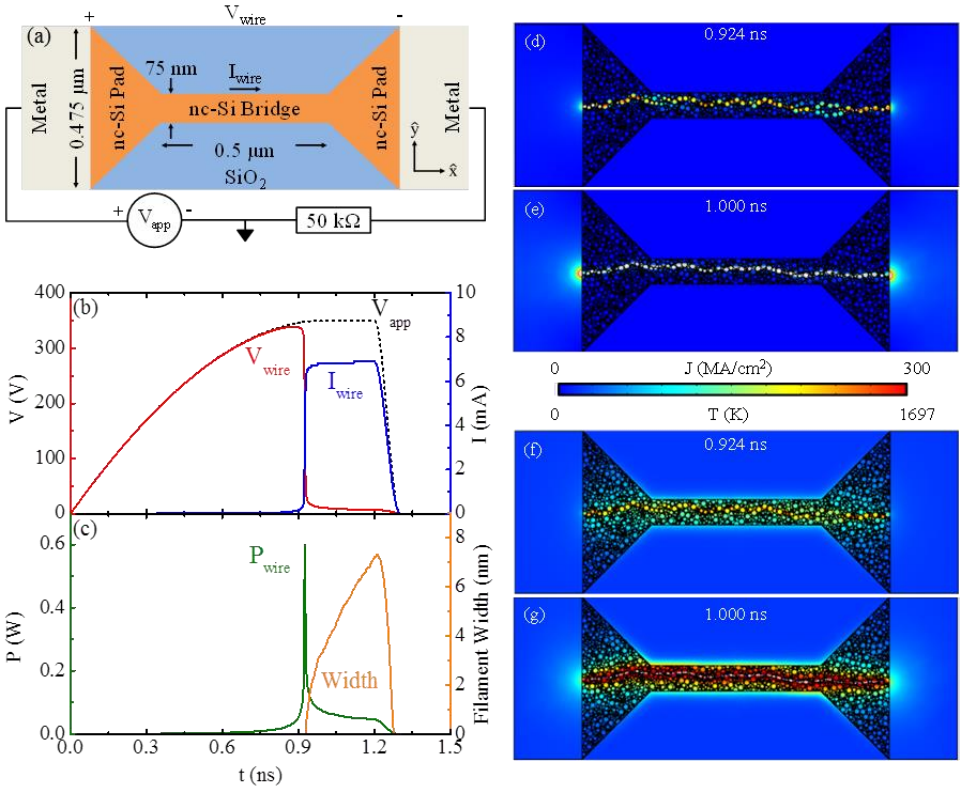


**Figure 11.** (a) 2-D structure used to model nc-Si wires. Simulations of suspended nc-Si wires do not use $SiO_2$ (blue). (b) Applied voltage across nc-Si wire on $SiO_2$ and 50 kΩ load resistor ($V_{app}$), voltage across wire ($V_{wire}$), and current through wire ($I_{wire}$) as a function of time. (b) Power dissipated within wire ($P_{wire}$) and average filament width as a function of time. (d-e) Current density and (f-g) temperature throughout nc-Si wire on $SiO_2$ during molten filament formation for $\tau$ = 1.5 ns. White regions indicate T > 1697 K (molten) and J > 300 MA/cm$^2$.

structure with a $SiO_2$ block with thermal boundary conditions set on the outer perimeter of the $SiO_2$ block. Simulated filaments are observed in both suspended and on-$SiO_2$ wires for 1.5 and 15 ns pulses. The wires completely melt with 150 ns pulses. Simulated voltage, current, power, and filament width are shown in Figure 11b-c for an example simulation ($\tau$ = 1.5 ns, on-$SiO_2$).

Multiple percolation pathways get initiated within the wire prior to filament formation (Figure 11d,f). Since electrical resistivity decreases with increasing temperature (Figure 10), self-heating leads to positive feedback and the percolation path that carries the largest current experiences thermal runaway, forms the molten filament extending from contact-to-contact while all other percolation paths vanish. The initial filament confines a current density of ~100 MA/cm$^2$ (Figure 11d,f) to 10-30% of the width, and its formation can be sensed as a rapid decrease in wire resistance (Figure 11b). The filament widens in the wire while remaining narrow near the metal contacts, which have thermal conductivity significantly larger than that of the surrounding nc-Si. Heat diffusion to surrounding $SiO_2$ in the on-$SiO_2$ cases leads to narrower filaments in the wire. Molten filaments typically form along the edges in suspended wires,

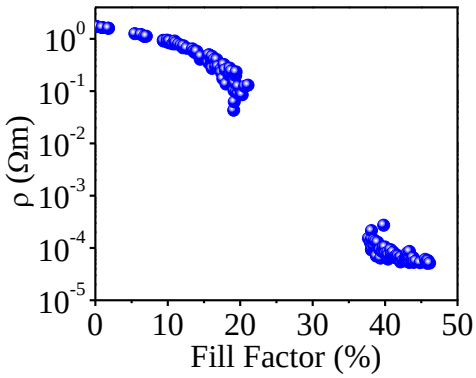


**Figure 12.** Resistivity of nc-Si versus fill factor we have extracted from 2D simulations using a mesh based crystallinity model, where electrical conductivity depends on both temperature and electric field. Percolation transport gives rise to significant reduction in resistivity at ~ 20% fill factor, rather than 99.5%.

as we have verified by simulating a square structure with uniform crystalline distribution for two different current directions. If the initial location of a filament is near an edge, the molten filament typically relocates to the nearest edge over time. Repeated simulations show that edge melting has little dependence on grain distribution for suspended wires. However, if initial filament formation is approximately in the center of a suspended wire, a symmetrical temperature profile about the molten filament is achieved, and no tendency to shift towards an edge is observed. The same is observed for wires on $SiO_2$, where the lateral heat diffusion into $SiO_2$ gives rise to a symmetric profile.

The models used for this analysis do not account for dielectric breakdown of the a-Si regions separating c-Si grains, conductivity dependence on crystal orientations, diffusion currents, movement of impurities, dynamic crystallization (growth-from-melt), mechanical deformations or stress, thermoelectric effects, thermal boundary resistances, and nanoscale thermal phenomena. Dielectric breakdown leads to increased joule heating and accelerated filament formation in the direction of the highest field (Figure 12). Neglecting dielectric breakdown, therefore, increases the thin film resistivity of simulated nc-Si and may alter the location of filament formation. In this model crystal grains lack specific orientations, which would contribute to additional electrical and thermal conductivity variations among the crystalline grains. Diffusion currents are expected to give rise to wider filaments due to lateral diffusion of the charge carriers. Movement of the impurities across the liquid-solid interfaces and crystallization (or amorphization) upon cooling, which are expected to change the dynamics of filament formation and the final resistance profile of the structure, are not captured by the static material definitions of impurity concentration and crystallinity used in this model. Thermal expansion of the heated regions, 5% volume reduction in liquid phase and piezo-resistivity of silicon is expected to result in mechanical deformations, voids and changes in the conductivity profile, which are also not yet modeled. Thermoelectric effects are expected to introduce an asymmetry in the melting profile while thermal boundary resistances and reduced thermal conductivity in nanostructures is expected to increase the heating rate.

Modeling percolation transport and filament formation in nanocrystalline materials or nanocomposites is important for understanding electro-thermal processes at nanometer scale for development of novel electronic components including phase-change and resistive memories.

### Crystallization of silicon microstructures through rapid self-heating

We have been investigating electrical self-heating of nc-Si micro-wires to achieve single crystal silicon micro-structures on arbitrary substrates with lithographic placement and geometry control. The wires are the same as described in previous sections. Results from numerous experiments showed that self-heating through long-duration, low-amplitude voltage stresses does not lead to solid phase epitaxial growth but typically leads to formation of larger crystalline grains and fracture of the structures. However, self-heating of suspended structures through short duration (~ μs) large-amplitude (~ 20-40 V) pulses leads to rapid melting (1690 K for Si) and growth from the melt as the wires re-solidify (Figure 13). A significant texture and shape change observed in the SEM images accompanied by ~ 4-10x reduction in resistance suggest formation of two large single-crystal grains on either side of the wire as two solid-liquid interfaces move in from the contact pads. Transmission electron microscopy analysis of a crystallized section of a wire also indicates single-crystal formation.

Non-suspended structures require more power for melting due to the thermal loss to the substrate, and may be less immune to nucleation along the wire that can result in additional grain boundaries. In suspended structures re-solidification starts from the cold pads - not favoring nucleation from multiple points on the structure - and it is observed to result in a 'growth-from-melt' from each contact pad. Since suspended structures melt at lower current densities, it is relatively easy to control the melting of these structures without forming liquid filaments on the contact extensions (Figure 13). The contact extensions can serve as in-situ resistors which can be utilized to self-terminate the melting process.

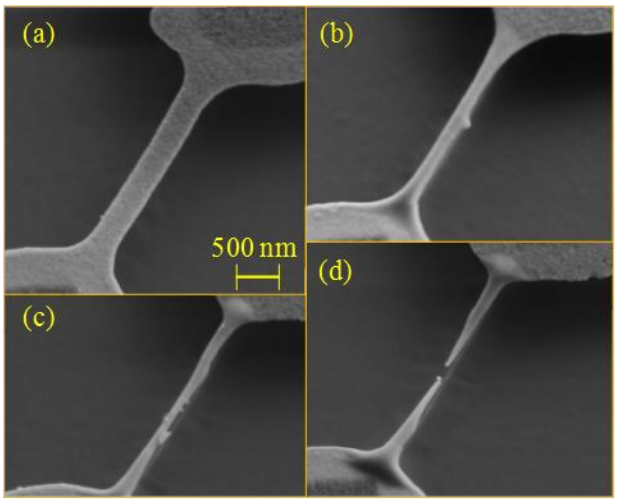


**Figure 13.** Four 2.5 μm long suspended Si microwires (a) as-fabricated (no electrical stress) and after (b) 40 V, 1 μs pulse, (c) 40 V, 2 μs pulse, (d) 40 V, 5 μs pulses.

Two distinct crystallization results have been achieved on suspended structures depending on the wire geometry and electrical stress conditions. In shorter wires the re-solidified segments acquire a cylindrical shape (Figure 13) and in longer wires (5.5 μm), they acquire a flat ribbon shape with extremely smooth surfaces and no visible line edge roughness (Figure 14). It appears that if a wire remains molten for a sufficient period of time it acquires a cylindrical shape due to surface tension. Otherwise, it tends to retain the as-fabricated shape and it crystallizes as a faceted, highly uniform ribbon. In both cases, the crystallized wires are under tensile stress and all have a lump at the center. This lump is expected to form as the two ends of the wire are crystallizing in their liquid shape and expanding upon solidification due to reduced mass density in solid state, forcing the excess material to the center and out (Figure 13b, Figure 14). Accumulation of material on the pads is also typically observed in wires crystallized with cylindrical form, likely due to mass diffusion from hot to cold if the wire remains molten for a sufficiently long period (Figure 13, Figure 14).

Numerical simulations of Joule heating in nanocrystalline silicon structures similar to those used in the experiments show good agreement in terms of electrical stress conditions and temperatures reached, and indicate that the underlying layer and anchors remain at room temperature, making this crystallization technique compatible with low temperature substrates. Radiation (far and near field) and convection heat contributions were determined to be negligible and are not included in these simulations. Thermoelectric effects are expected to significantly change the location of the hottest spot along the wire but not the temperatures reached and are not included in this simulation.

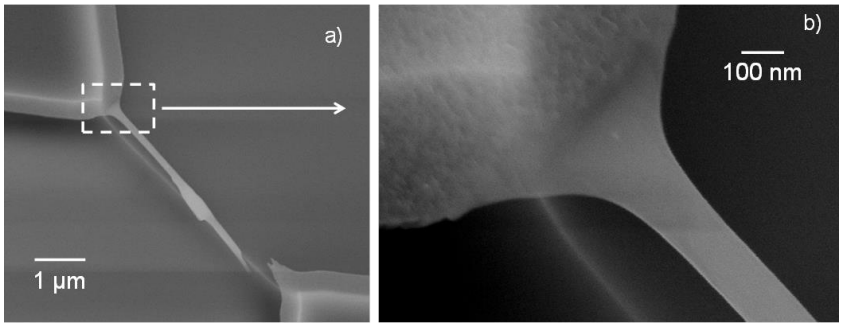


**Figure 14.** (a) 4 μm long suspended silicon wire after a 30 V, 1 μs pulse. (b) Higher magnification image of the wire end showing a significant change in texture and extremely smooth surface and edges of the crystallized section.

In these experiments the starting silicon films were highly doped (~ $10^{20}$ $cm^{-3}$). Lower doping levels are required for most electronic devices (~$10^{17}$-$10^{19}$ $cm^{-3}$) and the corresponding conductivity may not be large enough for sufficient Joule self-heating within practical voltage levels. However, melting followed by re-solidification starting from the cold ends of the wire after termination of the pulse is expected to segregate the dopants to the center upon complete resolidification, a micro-version of the *zone refinement* process which is used as a purification method in semiconductor processing. This dopant segregation or zone refinement process would leave either side of the wire with lower doping concentration, where the active electronic devices would be fabricated. Alternatively, crystallization of lower doped structures may be achieved by applying a field sufficient for electrical breakdown that would initiate self-heating and thermal runaway which can be practical for smaller structures.

Crystallization of suspended, lithographically defined silicon structures by local, rapid self-heating shows promise for formation of large single-crystal domains for high performance electronics on arbitrary substrates, such as complete systems on glass or plastics, photovoltaics, 3D integration of CMOS or integration of silicon devices with different material systems. Planar transistors can be fabricated on crystallized ribbons and partially or fully wrapped gate transistors can be fabricated on cylindrically crystallized wires. A variety of structure geometries and electrical stress conditions can be used which can potentially lead to different crystallization results.

### Significance of thermoelectric effects on self-heating crystallization depending on electrical conditions - relative impact of Joule and Thomson heat

We have performed electrical stress experiments with voltage pulses with varying amplitudes and durations (30 ns to 1 µs) to study the impact of thermoelectric effects in crystallization of silicon wires depending on the electrical conditions. Applied voltage pulse and current through the wire were acquired using a fast oscilloscope. Observed changes on the wires vary from surface modifications (Figure 15b) or partial melting to full melting and crystallization (Figure 15c) with increasing current (Figure 15d). For 30 ns and 100 ns pulses, changes on the wires are approximately symmetric with respect to the wire center ((Figure 15a-h)). 1 µs pulses, however, result in asymmetric wire modifications and melting/crystallization (Figure 15i-l). These experiments show that, *for similar peak temperatures, hence thermal gradients* (as shown in each row in Figure 15), asymmetric self-heating of symmetric structures is only significant for relatively lower, long duration electric current. In general, the importance of asymmetric Thomson heat in comparison to that of symmetric Joule heating increases as the electric current decreases.

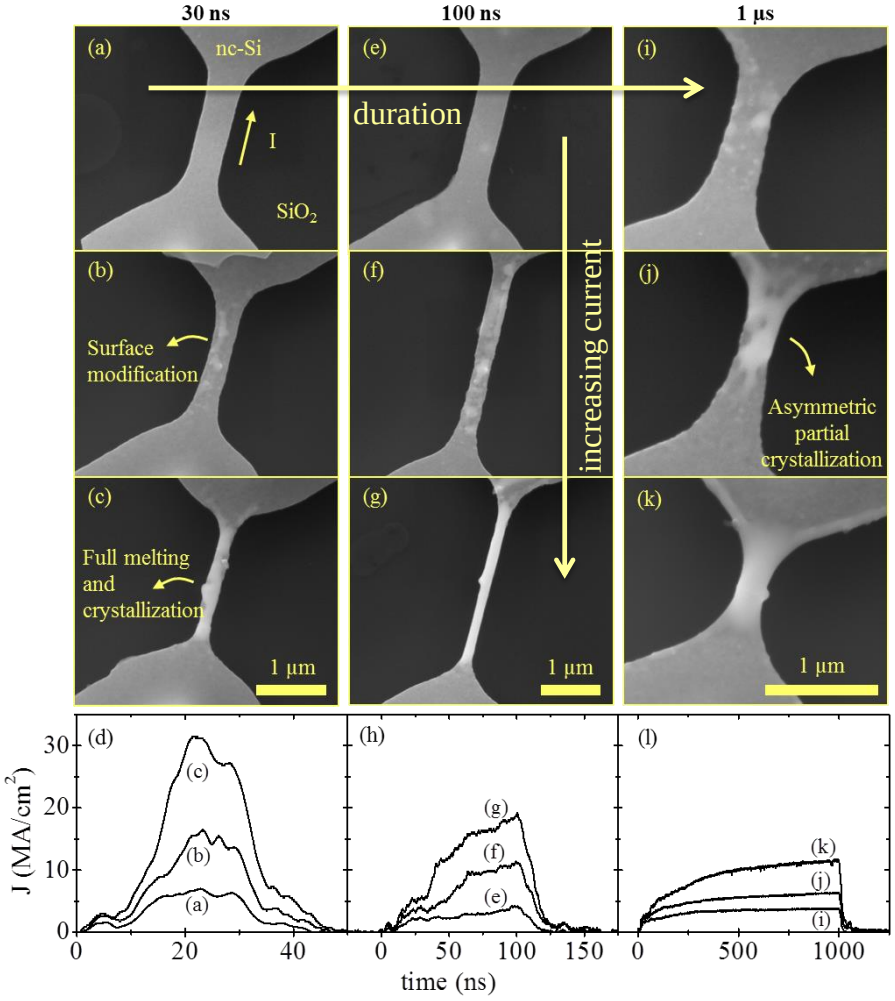


**Figure 15.** SEM images of nc-Si wires after single voltages pulses with durations of ~ 30 ns (a-c), ~ 100 ns (e-g) and 1 µs (i-k), all with ~ 8 ns rise and fall times. Images in the same column share the same pulse duration and scale bar, with increasing current. (d, h and l) Current vs. time for each case.

Joule heating is always positive ($j^2/\sigma$) and alone would result in a symmetric temperature profile; on the other hand, thermoelectric Thomson heat (Eq. 2) can be positive or negative (heating or cooling) depending on the sign of the Seebeck gradient hence causes an asymmetric temperature profile; Joule heating increases with $J^2$, whereas Thomson heat increases with $J$. Therefore, symmetric Joule heating dominates for large current levels. When a lower current density is applied (for a longer duration to achieve similar peak temperatures) the effect of Thomson heat increases, causing significantly asymmetric self-heating. The relative roles of Joule and Thomson heating can be seen through numerical modeling of the structures (Figure 16): A large amplitude pulse results in nearly symmetric heat generation along the wire, whereas a longer lower amplitude pulse results in a significantly distorted profile. For all cases, increased heating takes place at the cooler (more resistive) ends of the wires.

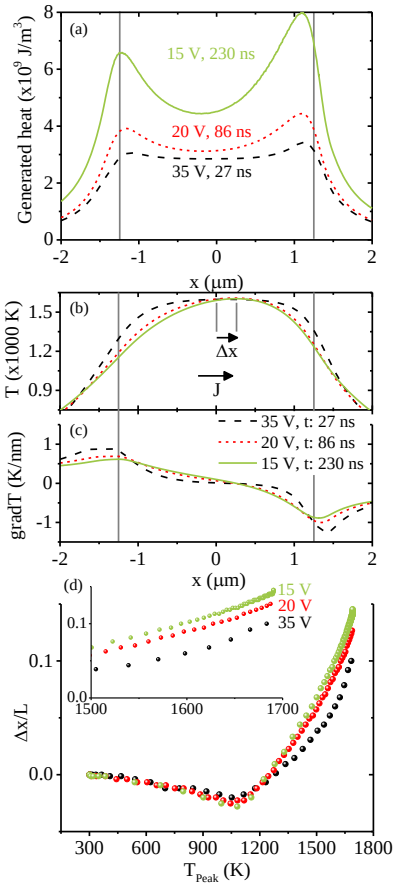


**Figure 16.** (a) Simulated heat (Joule and Thomson heat) along a 2.5 μm wire for different voltage, times. Vertical lines show wire ends. (b) Temperature, (c) temperature gradient for peak T~ 1600 K and (d) Shift in the hottest spot.

## Related publications (9/2010 to 3/2013)

### *Journal Articles Submitted/In Preparation*

[9] G. Bakan, A. Gokirmak and H. Silva, "Thermoelectric effects in self-heating crystallization of silicon microwires: relative impact of Joule and Thomson heating," to be submitted April 2013, material partially included in this report (Figures 19-21).

[8] G. Bakan, N. Khan, H. Silva and A. Gokirmak, "High-temperature thermoelectric transport at small scales," to be submitted March 2013, material partially included in this report (Figures 4, 6-8).

[7] S. Fischer, C. Osorio, S. Ayas, N. Williams, H. Silva, A. Gokirmak, "Finite Element Modeling of Current-Induced Filaments in Nanocrystalline Silicon nanowires," *under review*, *Applied Physics Letters* March 2013, material partially included in this report (Figures 14, 15).

### *Journal Articles Published/Accepted*

[6] N. Kanan, A. Faraclas, N. Williams, H. Silva and A. Gokirmak, "Computational Analysis of Rupture Oxide Phase Change Memory Cells," IEEE Trans. on Electron Devices 2013, accepted with minor revisions, revised version submitted.

[5] K. Cil, Y. Zhu, J. Li, C. H. Lam, H. Silva, "Assisted cubic to hexagonal phase transition in GeSbTe thin films on silicon nitride," *Thin Solid Films,* accepted with minor revisions, revised version submitted.

[4] G. Bakan, L. Adnane, A. Gokirmak, H. Silva, "Extraction of temperature dependent electrical resistivity and thermal conductivity from silicon microwires self-heated to melting temperature," *Journal of Applied Physics* 112, 063527 (2012).

[3] N. Williams, H. Silva, A. Gokirmak, "Finite Element Analysis of Scaling of Micro Thermoelectric Generators," AIP *Journal of Renewable and Sustainable Energy* 4**,** 043110 (2012).

[2] H. Silva, G. Bakan, A. Cywar, N. Williams, N. Henry, F. Dirisaglik, A. Gokirmak, "Crystallization of silicon microstructures through rapid self-heating for high-performance electronics on arbitrary substrates," *Nanoscience and Nanotechnology Letters* 4, 10, pp. 970-976(7) (2012).

[1] G. Bakan, N. Khan, A. Cywar, K. Cil, M. Akbulut, A. Gokirmak and H. Silva, "Self-heating of silicon microwires: Crystallization and thermoelectric effects," *Journal of Materials Research*, 26: 1061-1071, *Invited Feature Paper* (2011).

### *Full-length proceedings*

[6] A. Faraclas, N. Williams, G. Bakan, A. Gokirmak, H. Silva, "Comparison of Instantaneous Crystallization and Metastable Models in Phase Change Memory Cells," Proc. 2012 IEEE Device Research Conference (2012).

[5] N. Williams, A. Gokirmak, H. Silva, "Finite Element Simulations on Scaling Effects of 3D SiGe Thermoelectric Generators," Mater. Res. Soc. Symp. Proc. Vol. 1388 (2012).

[4] S. Fischer, C. Osorio, N. Williams, H. Silva, A. Gokirmak, "Finite element modeling of current-induced filaments in nanocrystalline silicon", IEEE 2011 Intl. Semiconductor Device Research Symposium (ISDRS) (2011).

[3] A. Cywar, G. Bakan, A. Gokirmak, H. Silva, "Silicon nanowire-based oscillator achieved through solid-liquid phase switching," IEEE 2011 Intl. Semicond. Device Research Symposium (ISDRS) (2011).

[2] F. Dirisaglik, G. Bakan, A. Gokirmak, H. Silva, "Modeling of thermoelectric effects in phase change memory cells," IEEE 2011 Intl. Semiconductor Device Research Symposium (ISDRS) (2011).

[1] G. Bakan, N. Khan, H. Silva and A. Gokirmak, "Thermoelectric effects in current induced crystallization of silicon microstructures," in *MEMS and Nanotechnology, Vol.4, Springer,* 2011, 9-16.

### *Conference Presentations*

[13] F. Dirisaglik, G. Bakan, A. Gokirmak, H. Silva, "Finite Element Analysis of Thermoelectric Effect in Phase-change Memory Cells," *Mat. Res. Soc. Spring Meeting* F2.4 (2012).

[12] L. Adnane, F. Dirisaglik, M. Akbulut, Y. Zhu, C. Lam, A. Gokirmak, H. Silva, "High Temperature Seebeck Coefficient and Electrical Resistivity of GeSbTe Thin Films," American Physical Society March Meeting 2012, http://meetings.aps.org/link/BAPS.2012.MAR.Q28.6 (2012).

[11] S. Fischer, C. Osorio, N. Williams, H. Silva, A. Gokirmak, "Finite Element Modeling of Current-Induced Filaments in Nanocrystalline Silicon," American Physical Society March Meeting 2012, http://meetings.aps.org/link/BAPS.2012.MAR.L18.5 (2012).

[10] S. Fischer, N. E. Williams, C. Osorio, A. Gokirmak, H. Silva, "Finite Element Simulations of Current-Induced Filamentations in Nanocrystalline Silicon," *Mat. Res. Soc. Fall Meeting,* BB20.2, 2011.

[9] G. Bakan, A. Gokirmak, H. Silva, "Thermoelectric Transport under Large Temperature Gradients in Self-Heated Silicon Microwires," *Mat. Res. Soc. Fall Meeting,* W6.10, 2011.

[8] L. Adnane, N. E. Williams, A. Gokirmak, H. Silva, "High Temperature Seebeck Coefficient and Resistivity Measurement Setup," *Mat. Res. Soc. Fall Meeting,* O8.12, 2011.

[7] N. Khan, G. Bakan, A. Gokirmak and H. Silva, " Analysis of Light Emission from Self-Heated Nanocrystalline Silicon Microwires," *Mat. Res. Soc. Fall Meeting,* W7.5, 2011.

[6] N. E. Williams, A. Gokirmak and H. Silva, "Finite Element Simulations on Scaling Effects of Thermoelectric Generators," *Mat. Res. Soc. Fall Meeting,* F4.1, 2011.

[5] C. Osorio, G. Bakan, H. Silva and A. Gokirmak, "Two-dimensional Numerical Modeling of Nanocrystalline Silicon Structures Generating Randomly Distributed Circular Crystalline Domains in an Amorphous Matrix," *Mat. Res. Soc. Spring Meeting,* A8.8, 2011.

[4] N. E. Williams, A. Gokirmak and H. Silva, "Finite Element Analysis of Micro/Nano Thermoelectric Generators," *Mat. Res. Soc. Spring Meeting*, I3.4, 2011.

[3] N. Khan, G. Bakan, H. Silva and A. Gokirmak, "Optical observations of thermoelectric effects on self-heated nanocrystalline microwires," *Mat. Res. Soc. Fall Meeting*. AA12.5 ,2010

[2] S. Ayas, G. Bakan, N. E. Williams, A. Gokirmak and H. Silva, "Finite element simulation of filamentation in nanocrystalline silicon films under electrical stress," *Mat. Res. Soc. Fall Meeting*. AA17.64, 2010

[1] G. Bakan, N. Khan, H. Silva and A. Gokirmak, "Optical observations and numerical modeling of the thermoelectric Thomson effect on self-heating silicon microwires," *Mat. Res. Soc. Fall Meeting*. LL8.2, 2010.

## 3. Non-equilibrium semiconductor finite element modeling – Generation-Transport-Recombination of Minority Carriers

The finite element simulation model used in the previous award period handles charge transport using drift and diffusion (thermoelectric) currents assuming steady state (current continuity) for a uniform material,

$$\nabla \cdot \bar{J} = \nabla \cdot (-\sigma \nabla \psi - \sigma S \nabla T) = 0 \tag{4}$$

where $\bar{J}$ is the current density ($Am^{-2}$), σ is the electrical conductivity ($Sm^{-1}$), $\psi$ is the electrical potential ($V$), $T$ is the temperature ($K$), and $S$ is the Seebeck coefficient ($VK^{-1}$).

Temperature changes was modeled by accounting for heat generation by joule heating (energy loss from the charge carriers to the lattice), and heat flow by thermal conduction and by charge carriers,

$$\overbrace{dCp\frac{dT}{dt}}^{\text{heat absorbed by material}} \quad \overbrace{-\nabla.(k\nabla T)}^{\text{Fourier heat conduction}} = \overbrace{-\nabla\psi.\bar{J}}^{\text{Joule heating}} \quad \overbrace{-\nabla.(\bar{J}\Pi)}^{\text{Thermoelectric heat}} \tag{5}$$

where $d$ is the mass density, $C_P$ is the specific heat, and $k$ is the thermal conductivity and $\Pi = ST$ is the average energy per charge carrier.

The latent heat of fusion during the solid-to-liquid phase transition for silicon is accounted for by incorporating a 10 K wide peak in $C_p$ around melting temperature where all the material parameters linearly transition to their liquid-state values.

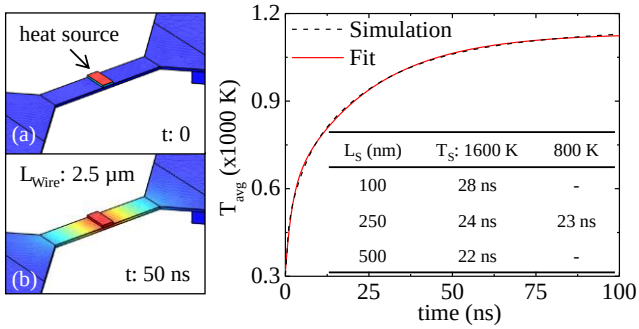


**Figure 17.** Example simulated heat diffusion in a Si microwire from a small heat source placed at the center, top surface of the wire. (a) Change in average temperature for a 2.5 µm x 0.5 µm x 50 nm suspended wire (750 nm above silicon substrate) for various constant heat source temperatures and heat source lengths. At t=0 the wire is at 300 K. (b) Heat diffusion time constants (1st time constant of a 2nd order exponential fit to the simulated temperature).

The thermoelectric heat term in (5) was broken down in two parts (6), *electronic convective heat flow* and *generation-transport-recombination (GTR)*, the relative contribution of each gives rise to the asymmetric heating in Si microwire.

$$\overbrace{-\nabla.\left(\bar{J}\Pi\right)}^{\text{Heat transfer between carriers and lattice}} = \underbrace{\overbrace{\bar{J}_n.\nabla\left(S_nT\right)}^{\text{Convective heat flow by electrons}} + \overbrace{\bar{J}_p.\nabla\left(S_pT\right)}^{\text{Convective heat flow by holes}}}_{\text{Electronic-convective}} + \underbrace{\overbrace{\left(\nabla.\bar{J}_p\right)}^{\text{Local generation rate}}\overbrace{\left(S_pT-S_nT\right)}^{\text{Energy of an electron-hole pair}}}_{\text{Generation-transport-recombination}} \quad (6)$$

where subscript '*n*' and '*p*' refers to electrons and holes respectively.

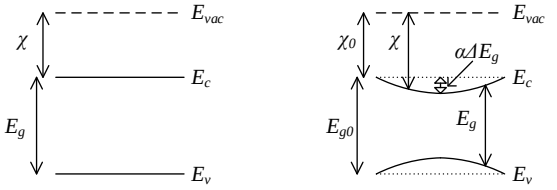


Figure 18. Definition of energy levels, (left) with and (right) without bandgap degradation.

Although the previous model could describe the underlying physical mechanism quite satisfactorily, the assumption of charge neutrality is not very accurate due to some charge separation and build-in fields under thermal gradients (thermoelectric effects). This effect is relatively small (~ 100 mV for a 1000K thermal gradient along a 1 μm of Si wire) compared to the external voltages applied for self-heating (~ 10 V/μm). However, it is expected to affect drift and recombination of minority carriers which play a critical role in the GTR contribution to the thermoelectric heat and charge buildup in time. In the previous model, carrier densities are calculated based on the temperature using Fermi-Dirac statistics and assuming charge neutrality. This modeling approach is commonly used for single material systems with a strongly dominant single carrier type (electrons or holes). Poisson equation must also be solved in a self-consistent manner with the drift-diffusion current and heat models to account for charging along the structures.

During the second period of the project we developed a computational model to solve the three equations self-consistently so that carrier densities can be found more accurately based on the Poisson charge equation using COMSOL Multiphysics finite element simulator.

The transport of carriers in any semiconductor material is generally described by Poisson's equation (7) and continuity equations for both carriers, electron (8) and hole (9) [4], [5],

$$\nabla.\bar{D} = \nabla.\left(\varepsilon\bar{E}\right) = -\nabla.\left(\varepsilon\nabla\psi\right) = q(p - n + N_D^+ - N_A^-) \quad (7)$$

$$\frac{\partial n}{\partial t} = \frac{1}{q}\nabla.\bar{J}_n - U_n \quad (8)$$

$$\frac{\partial p}{\partial t} = -\frac{1}{q}\nabla.\bar{J}_p - U_p \quad (9)$$

where, *n(p)* is the electron (hole) concentration ($m^{-3}$), $N_D^+$ ($N_A^-$) is the Ionized donor (acceptor) concentration ($m^{-3}$), $\bar{D}$ is the electric flux density ($Cm^{-2}$), $\varepsilon$ is the Permittivity ($Fm^{-1}$), $\bar{E}$ is the Electric field ($Vm^{-1}$), $\psi$ is the electric potential ($V$), $q$ is the electron charge ($C$), $\bar{J}_n$ ($\bar{J}_p$) is the electron (hole) current density ($Am^{-2}$).

Figure 18a defines the relationship between different energy levels is a semiconductor. The vacuum energy level ($E_{vac}$) in a material depends on the potential energy at different locations. $E_{vac}$ can be found by subtracting the potential energy from a reference energy level ($E_{ref}$) [5],

$$E_{vac} = E_{ref} - q\psi \tag{10}$$

If we consider $E_{ref} = 0$, then vacuum energy level becomes,

$$E_{vac} = -q\psi \tag{11}$$

The difference between $E_{vac}$ and the conduction band edge ($E_c$) is called the electron affinity ($\chi$). Therefore, the expression of $E_c$ is,

$$E_c = E_{vac} - \chi \tag{12}$$

$$E_c = -q\psi - \chi \tag{13}$$

The inclusion of electron affinity in the calculation provides with the flexibility of choosing different materials in the simulation.

If we now subtract the bandgap energy ($E_g$) from $E_c$ we will get the expression for the valence band energy level ($E_v$),

$$E_v = E_c - E_g \tag{14}$$

$$E_v = -q\psi - \chi - E_g \tag{15}$$

Figure 18b is a modified version of Figure 18a where bandgap reduction ($\Delta E_g$), due to doping or temperature, is accounted for. $\alpha$ is the conduction band reduction, therefore, 1-$\alpha$ is the valence band reduction. In the simulation, α is kept equal to 0.5, maintaining equal reduction of conduction and valence band. Therefore,

$E_g = E_{g0}\text{-}\Delta E_g$ = Effective bandgap (eV)

$E_c = E_{c0} - \alpha\Delta E_g$ = Effective conduction band (eV)

$E_v = E_{v0} + (1\text{-}\alpha)\Delta E_g$ = Effective valence band (eV)

The subscript '0' is referred to the quantities at a particular temperature ($T_0$ = 300 K for all the simulations) and doping density ($N_0$).

The intrinsic energy level ($E_i$) now can be found from the following expression,

$$E_i = \frac{E_c + E_v}{2} + \frac{k_B T}{2}\ln\left(\frac{N_V}{N_C}\right) \tag{16}$$

$$E_i = -q\psi - \chi - \frac{E_g}{2} + \frac{k_B T}{2}\ln\left(\frac{N_V}{N_C}\right) \tag{17}$$

where $k_B$ is Boltzmann constant.

We will derive the expression of current density from the gradient of the Fermi level. The definition of electron and hole quasi-Fermi level ($F_n$ and $F_p$) are defined as follows:

$$F_n = E_c + k_B T \Im_{1/2}^{-1}\left(\frac{n}{N_c}\right) \tag{18}$$

$$F_p = E_v - k_B T \Im_{1/2}^{-1}\left(\frac{p}{N_v}\right) \tag{19}$$

where

$k_B$ = Boltzmann's constant

$\Im_{1/2}^{-1}(\ )$ = Inverse Fermi level of the order of ½.

Using Boltzmann's approximation, (18) and (19) can be written as:

$$F_n = E_c + k_B T \ln\left(\frac{n}{N_c}\right) \tag{20}$$

$$F_p = E_v - k_B T \ln\left(\frac{p}{N_v}\right) \tag{21}$$

In terms of intrinsic Fermi level, (20) and (21) can be further written as:

$$F_n = E_i + k_B T \ln\left(\frac{n}{n_i}\right) \tag{22}$$

$$F_p = E_i - k_B T \ln\left(\frac{p}{n_i}\right) \tag{23}$$

We will use (22) and (23) to derive the expression of current densities ( $\bar{J}_n$ and $\bar{J}_p$ ) used in (8) and (9) respectively. There would be a flow of charge carriers (electrons or holes) once there is a gradient in their respective quasi Fermi levels. The expression of the electron and hole current densities are expressed as,

$$\bar{J}_n = \mu_n n \nabla F_n \tag{24}$$

$$\bar{J}_p = \mu_p p \nabla F_p \tag{25}$$

where, $\mu_n$ ($\mu_p$) is electron (hole) mobility ($m^2V^{-1}s^{-1}$).

Using (22), (23), (24) and (25) we find,

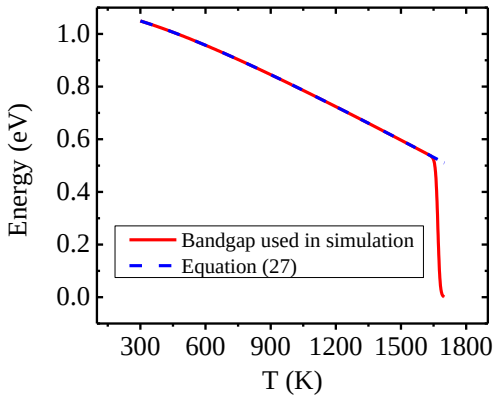


Figure 19. Bandgap function used in the simulation.

| Parameter | Value |
|---|---|
| $\tau_{n=}\tau_p$ | 1 μs |
| $C_n$ | $2.8 \times 10^{-31}$ $cm^6s^{-1}$ |
| $C_p$ | $0.99 \times 10^{-31}$ $cm^6s^{-1}$ |

Table 1. The recombination parameters used in the model.

$$\bar{J}_n = \overbrace{-\mu_n n\left\{q\nabla\psi + \nabla\chi + \frac{\nabla E_g}{2} - \frac{k_B T}{2}\left(\frac{\nabla N_v}{N_v} - \frac{\nabla N_c}{N_c} - \frac{2\nabla n_i}{n_i}\right)\right\}}^{drift} + \overbrace{\mu_n k_B T \nabla n}^{diffusion} + \underbrace{\frac{\mu_n n k_B}{2}\left\{\ln\left(\frac{N_v}{N_c}\right) + 2\ln\left(\frac{n}{n_i}\right)\right\}\nabla T}_{thermal\ diffusion} \tag{26}$$

$$\bar{J}_p = \overbrace{-\mu_p p\left\{q\nabla\psi + \nabla\chi + \frac{\nabla E_g}{2} - \frac{k_B T}{2}\left(\frac{\nabla N_v}{N_v} - \frac{\nabla N_c}{N_c} + \frac{2\nabla n_i}{n_i}\right)\right\}}^{drift} - \overbrace{\mu_p k_B T \nabla p}^{diffusion} + \underbrace{\frac{\mu_p p k_B}{2}\left\{\ln\left(\frac{N_v}{N_c}\right) - 2\ln\left(\frac{p}{n_i}\right)\right\}\nabla T}_{thermal\ diffusion} \tag{27}$$

## Bandgap degradation

In this model, we have implemented temperature and doping dependent bandgap. The general expression of bandgap for Si is [4], [6]:

$$E_g(N,T) = 1.166 - 22.5\times10^{-3}\sqrt{\frac{N}{10^{24}}} - \frac{4.73\times10^{-4}T^2}{T+636} \quad (eV) \tag{28}$$

The usual bandgap reduction model failed to account for the near zero bandgap at melting. Hence an exponential decrease is added to the bandgap function so that the bandgap reduces to a very small number from 1680 K to 1700 K Figure 19.

## Recombination mechanisms

The recombination of minority carriers is of great importance to the GTR theory. We added the well-known SRH [7] and Auger [8] recombination mechanisms to the model.

$$SRH = \frac{np - n_i^2}{\tau_n(n+n_i) + \tau_p(p+n_i)} \tag{29}$$

$$Auger = C_n\left(n^2 p - n n_i^2\right) + C_p\left(np^2 - p n_i^2\right) \tag{30}$$

The high electric field effect, such as: impact ionization has not been added in the model as the maximum electric field calculated for this homogeneous silicon wire is around $10^4$ V/cm which is one order

of less than the threshold electric field [9]. Nevertheless, these high electric field effects can be easily incorporated in the model.

### Heat transfer equation

In contrast to (5), the heat transfer equation used in the non-equilibrium non-isothermal semiconductor model is,

$$\underbrace{dC_p\frac{\partial T}{\partial t}}_{\text{Heat absorbed}} + \underbrace{\nabla.(-\kappa\nabla T)}_{\text{Heat loss through conduction}} = \underbrace{-\nabla\psi.\bar{J}}_{\text{Joule heat}} + \underbrace{(E_G+3k_BT)U}_{\text{Recombination heat}} - \underbrace{(\bar{j}_n+\bar{j}_p).\nabla\left(\frac{3}{2}\frac{k_BT}{q}+\frac{E_G}{q}\right)}_{\text{Electronic convective heat}} \qquad (31)$$

The second term in the right-hand side of (31) represents the recombination heat, which is the product of net recombination rate ($U$) and total energy associated per recombination event ($E_G + 3k_BT$), and the third term represents the electronic convective heat [10].

It is to be noted here that unlike the previous model, there is no latent heat of fusion inserted in $C_p$. The latent heat of fusion is an effective media approximation of the energy needed to sustain bond breakage at melting point. In the new model this energy is directly added to the system using the recombination heat term in (31).

### Results

Figure 20a shows the SEM image of an n-type silicon microwire and corresponding simulated thermal profile (white colored region signifies temperature higher than melting point) that provides excellent agreement between experiment and simulation in terms of melting direction and amount. Figure 20b shows the electron and hole concentrations along the middle of the wire during melt. The carrier concentration reached to ~ $5\times10^{22}$ $cm^{-3}$ which corresponds to one free carrier per atom in silicon [12]. Figure 20c shows the total current density ($J$) which is the summation of electron current ($J_n$) and hole current ($J_p$). Figure 20d shows the conduction band edge ($E_c$) and valence band edge ($E_v$). The merge of $E_c$ and $E_v$ in the middle of the wire corresponds to the near zero bandgap at melting.

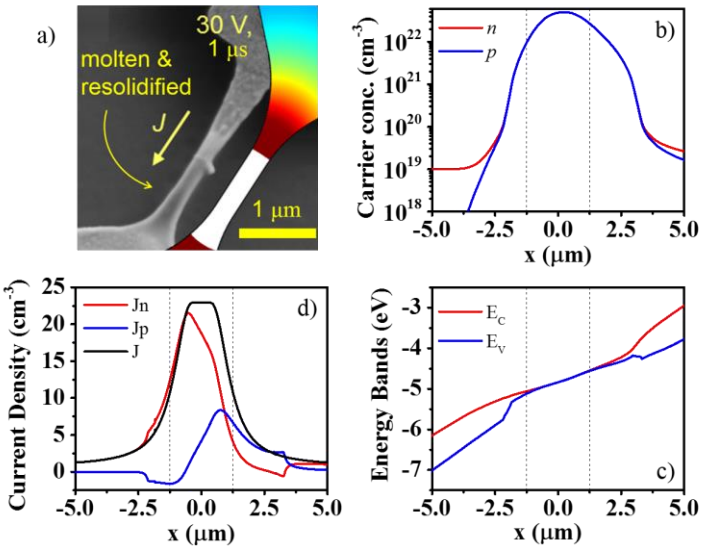


Figure 20. a) SEM image of asymmetrically molten and resolidified Si micro-wire (length: ~2.5 µm) by a 30 V, 1 µs electrical pulse [11] along with simulated temperature profile (molten region marked white), calculated carrier concentrations (b), band energy levels (c), and current densities (b) along the middle of the wire form the simulation. The dashed lines in b-c denotes the edge of the wire.

### Publications related to this work

#### Conference presentations

Sadid Muneer, Gokhan Bakan, Helena Silva, and Ali Gokirmak, “Computational Analysis Framework to Include the Effect of Generation-Transport-Recombination of Minority Carriers in Semiconductor”, ISDRS proceeding, Maryland 2017.

Nafisa Noor, Raihan Sayeed Khan, Sadid Muneer, Lhacene Adnane, Ryanne Ramadan, Faruk Dirisaglik, Adam Cywar, Chung Lam, Yu Zhu, Ali Gokirmak, and Helena Silva; “Short and Long Time Resistance Drift Measurement in Intermediate States of $Ge_2Sb_2Te_5$ Phase Change Memory Line Cells”, Mat. Res. Soc. Spring Meeting, 2017.

Nafisa Noor, Sadid Muneer, Lhacene Adnane, Raihan Sayeed Khan, Ryanne Ramadan, Faruk Dirisaglik, Adam Cywar, Chung Lam, Yu Zhu, Ali Gokirmak, and Helena Silva, “Pulse-mode Electrical Resistance Trimming of $Ge_2Sb_2Te_5$ Phase Change Memory (PCM) Line Cells”, International Semiconductor Device Research Symposium (ISDRS), 2016.

Raihan Sayeed Khan, Nafisa Noor, Aaron Ciardullo, Sadid Muneer, Lhacene Adnane, Faruk Dirisaglik, Adam Cywar, Chung Lam, Yu Zhu, Helena Silva, and Ali Gokirmak; “A Study on Stochasticity in Hexagonal Close Packed $Ge_2Sb_2Te_5$ Nanowires”, International Semiconductor Device Research Symposium (ISDRS), 2016.

Nafisa Noor, Kadir Cil, Lindsay Sullivan, Sadid Muneer, Faruk Dirisaglik, Adam Cywar, Chung Lam, Yu Zhu, Ali Gokirmak, and Helena Silva; “An experimental study on waveform engineering for $Ge_2Sb_2Te_5$ phase change memory cells”, Mat. Res. Soc. Fall Meeting, 2015.

F. Dirisaglik, G. Bakan, Z. Jurado, L. Sullivan, S. Muneer, M. Akbulut, K. Cil, Y. Zhu, C. Lam, H. Silva, A. Gokirmak, “High Speed, High Temperature Electrical Characterization of Meta-Stable Phases and Crystallization Dynamics of $Ge_2Sb_2Te_5$,” HH5.06, Mat. Res. Soc. Spring Meeting, 2014.

A. J. Deschenes, M. Akbulut, S. Muneer, H. Silva, and A. Gokirmak, “An Electrothermal Analysis of Magnetic Tunnel Junction MRAM Devices,” M7.02, Mat. Res. Soc. Fall Meeting, 2014.

S. Muneer, N. Noor, G. Bakan, Y. Zhu, A. Gokirmak and H. Silva, "Extraction of Electrical Resistivity and Thermal Conductivity of Self-heated GST Micro-bridges," Mat. Res. Soc. Spring Meeting, 2013.

F. Dirisaglik, J. Rarey, K. Cil, S. Muneer, L. Zhang, Y. Zhu, C. Lam, A. Gokirmak and H. Silva, "Metastable Electrical Resistivity of Amorphous Ge2Sb2Te5 at Elevated Temperatures," Mat. Res. Soc. Spring Meeting, 2013.

F. Dirisaglik, J. Rarey, K. Cil, S. Muneer, L. Zhang, Y. Zhu, C. Lam, A. Gokirmak and H. Silva, "Crystallization Times of Ge2Sb2Te5 Nanostructures as a Function of Temperature," Mat. Res. Soc. Spring Meeting, 2013.

## 4. Fast measurement of metastable resistivity, crystallization dynamics, extraction of activation energy, and its implication in carrier transport

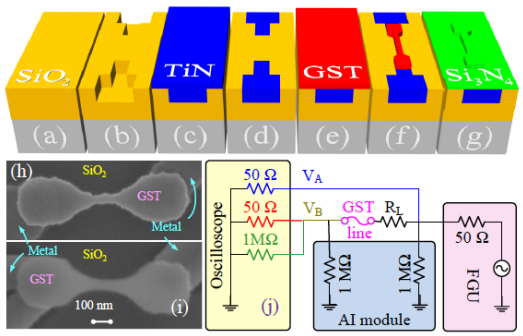


Figure 21. Schematic illustrations of the GST line cell fabrication steps: 700 nm $SiO_2$ grown on Si (a), 250 nm deep trench formation (b), 300 nm TiN fill (c), CMP (d), GST film deposition (e), patterning of GST film (f), $Si_3N_4$ cap layer deposition (g), SEM images of an as fabricated (h) and amorphized (i) GST line cell and schematics of the experimental setup (j).

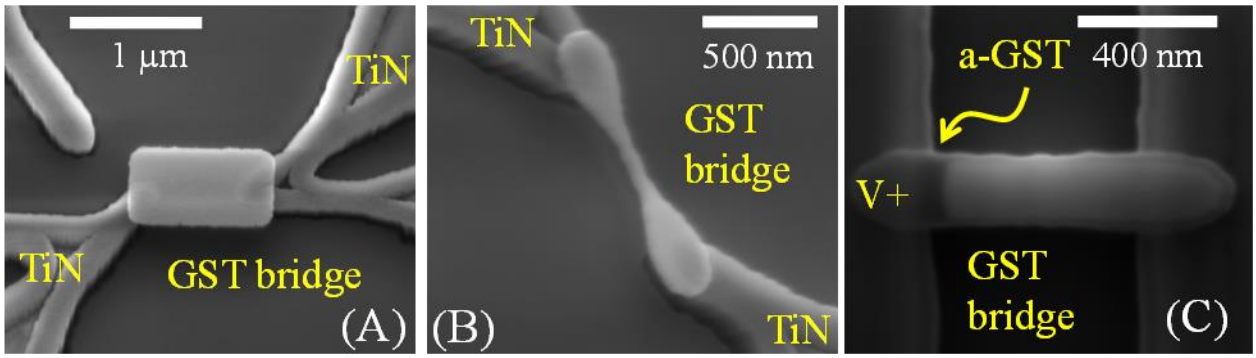


**Figure 22.** A, B: SEM images of example fabricated GST bridges with TiN contacts. C: We have observed highly asymmetric amorphization due to strong thermoelectric transport.

### High-speed electrical characterization

We developed a high-resolution electrical characterization scheme -built upon our pulse-based techniques for melting and crystallization experiments for Si micro-bridges- to extract the temperature dependent meta-stable electrical resistivity of the amorphous materials while monitoring the nucleation and crystallization dynamics in device scale. Long-duration crystallization process following amorphization is also electrically monitored as part of the same measurement. We have performed a set of detailed measurements on undoped Silicon and $Ge_2Sb_2Te_5$ in the 300 - 673 K range[13], [14] using the high-temperature cryogenic probe station (300 - 680 K, $10^{-5}$ torr) in our laboratory (Figure 21). Measurements on the Si structures show extremely rapid growth-from-melt and we have not yet observed amorphization and crystallization dynamics. As a contrast, GST solidifies as an amorphous material if the melt is allowed to rapidly cool (Figure 22). This allows observation of interesting materials behavior and characterization of its meta-stable amorphous phase.

The crystallization time scale of GST ranges from >10 years at room temperature to ~100 ns close to melting ($T_{melt\text{-}GST}$ ~ 900 K). However, during a typical set operation (rise times ~ 1-100 ns), the amorphous region (a-GST) experiences melting without having sufficient time for re-arrangement of the atoms in a crystalline structure. Hence a-GST retains its *metastable amorphous state* all the way up to melting. Similarly, the *metastable crystalline fcc phase* is retained above the *fcc-hcp* transition during reset operation. In slow measurements (typical maximum ramp rate ~ 1K/seconds), a-GST (and fcc-GST) gradually crystallizes as the temperature of a hot-chuck is ramped. Hence, slow measurements do not capture the meta-stable amorphous resistivity ($\rho_{a\text{-}GST}$) or the nucleation and crystallization dynamics which are critically important for device modeling. Significant changes in the resistivity are observed at 'transition temperatures', which corresponds to temperature points where crystallization is faster than the particular ramp-rate of the measurement.[15]

Slow and highly sensitive current voltage measurements using a semiconductor parameter analyzer can be used effectively to characterize highly resistive a-GST below the transition temperature, and a high-speed but less sensitive technique can be utilized at elevated temperatures immediately after amorphization. Typical oscilloscopes used for high-speed measurements provide a very high resolution in time (<1 ns) but does not provide as much resolution in voltage. Although DC current measurements can be performed by measuring the voltage at a 50 Ω termination, the DC offsets in oscilloscopes vary over time and is not possible to get well calibrated DC I-V measurements in the μV range. Additionally, the data depth of the oscilloscopes is limited (10 million points in our case). Hence, the high-resolution pulse cannot be monitored along with the whole recrystallization process using a single oscilloscope for $T_{chuck}$ = 300 ~ 700 K. (Note: Data transfer for 10 million data points over USB 2.0 takes several minutes.)

This technique utilizes a single-shot waveform containing sinusoid segments and a stepped melting pulse[16], [17] followed by a rapid cool-down (Figure 23). Sinusoids are used before and after the pulse to monitor the crystalline and the amorphous state resistivities at the ambient temperature and monitor the short-duration crystallization process. This waveform is applied in addition to a small DC offset that is continuously applied to the device. The long-duration DC offset enables electrical monitoring of the crystallization process and verifies the integrity of the device: recrystallization indicates successful amorphization, rather than a mechanical disconnect that is induced by the melting pulse.

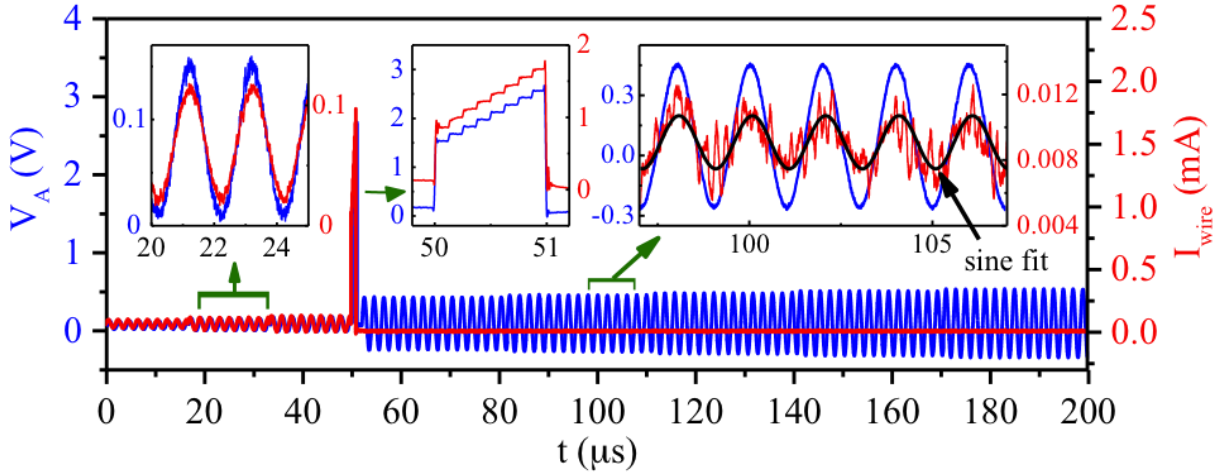


Figure 23. An example of applied and measured sequence of electrical signals showing voltage and current on a GST bridge and the sinusoidal fits in crystalline (before pulse) and amorphous (after pulse) states.

The raw data in each sinusoid segment is fit to a sinusoid with a fixed phase and frequency, minimizing the random errors due to noise (current levels are very low for the amorphous phase at low temperatures) and eliminate the problems associated with unknown offset voltages. The amplitudes from the sinusoid fits are used to construct current versus voltage graphs to extract the conductance from the slope. The amplitude of the sinusoid segments after the amorphization pulse are stepped up and down to form a hysteresis curve, monitoring the possible changes in the material during the 2 ms high-resolution measurement duration.

The melting pulse is stepped to make an I-V measurement in the molten state with voltage steps long enough to avoid the complications due to the RC transient response (Figure 24). These I-Vs are fitted to calculate the molten state resistivity, which also verifies successful melting of the bridge. A 1 µs cool-down period is used after the pulse with 0 V applied to the bridges to achieve rapid solidification prior to restoring to the baseline DC voltage level with the restart of the sinusoid signal. This eliminates the possibility of retaining a liquid filament after the melting pulse. The DC and AC signals used for the measurements are chosen to be large enough to observe measurable current levels (especially for amorphous phase after pulse) and small enough not to cause significant self-heating. Our experimental and modeling results show that the bridges return to the ambient temperature (controlled by the chuck) within the 1 µs cool-down period (time constant associated with cool-down is in ~1 ns scale). Linearity in the after pulse I-V characteristics as the voltage amplitude is stepped up and then down show that there is not a measurable change in the temperature of the structure or the phase of the material during the AC measurements (~ 2 ms). The long duration nucleation-crystallization dynamics is measured simultaneously using the DC signals via a DAQ card connected in parallel with 10 ms resolution, acquired directly into the memory of the computer controlling the measurements (DAQ card, the signal generator, oscilloscope and temperature controller), providing a practically unlimited record duration.

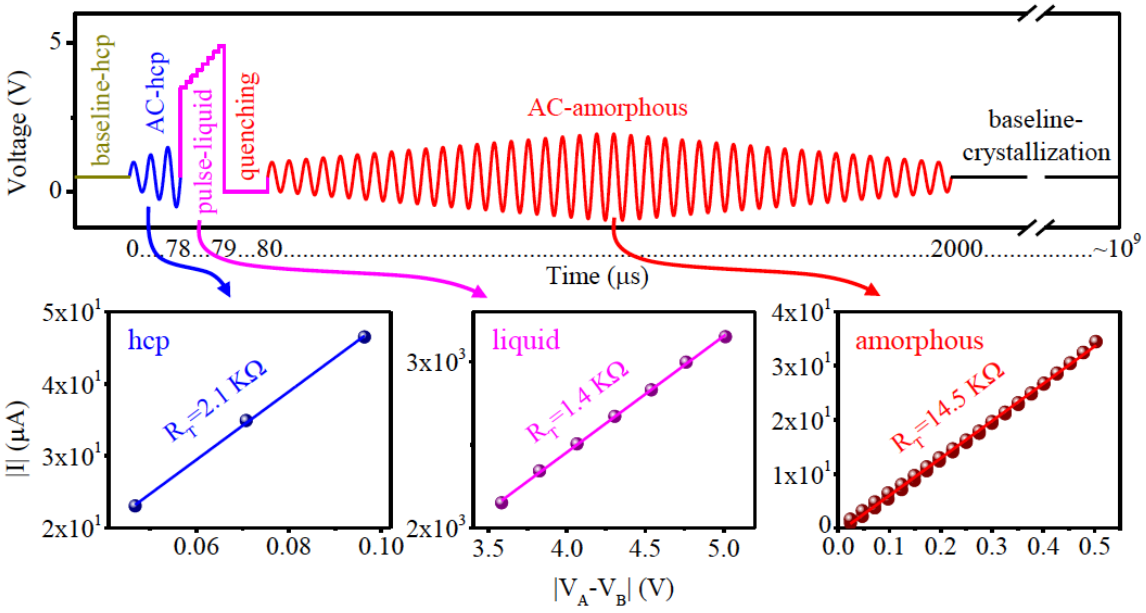


Figure 24. Schematic illustration of the high-resolution waveform, indicating the time scales of the different segments vary significantly (top). A set of I-V characteristics obtained from sinusoid fits before melting pulse (0-78 µs), stepped measurement during the melting pulse (78-80 µs), and sinusoid fits after the melting pulse (hysteresis measurement, 80-2000 µs) for $T_{chuck}$ = 550 K (bottom).

## Results

Using this technique, resistivity of the material in the crystalline state (before melting pulse), liquid state (during the melting pulse) and in meta-stable amorphous state (after the melting pulse) are directly measured and some indications of the nucleation-crystallization dynamics (both short-duration high-resolution, and long-duration, low-resolution) is obtained (Figure 25,Figure 26). $\rho_{a\text{-}GST}$ versus temperature characteristic are determined from measurements on >30 devices at each temperature point. Hysteresis loops seen in the 500 K and 550 K measurements and lack of any hysteresis at lower and higher temperatures indicate a peak in nucleation rate in an intermediate temperature range (~520 K), as was predicted by studies based on molecular dynamics simulations.

We believe that this is a powerful technique to detect nucleation at device scale but does not directly measure crystalline ratio, unlike laser reflectance measurements. The conductance data acquired from these measurements do not have a linear relationship with crystalline fraction since almost no current flows the structure -no detectable change in resistance- until percolation paths start to form (~15% in 3D and ~20-40% fill factor in quasi-2D structures). What is important for electrical devices is resistance not the fill factor, hence the results of these measurements are of more value compared to laser based techniques. Furthermore, it is not possible to make sensitive measurements at device scale using laser reflectance techniques.

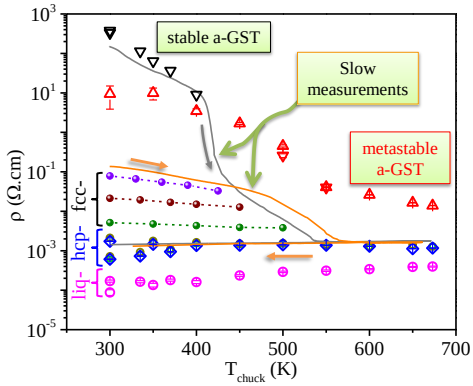


Figure 25. Measured GST resistivities as a function of chuck temperature. Solid lines show slow R-T measurements (with 3.5 K/min heating rate ) on two cells. Symbols show measurement results at a constant chuck temperature. Each data point is an average of data collected from 35 cells. AC measurements for amorphous GST (Δ) for T ≤400 K is not accurate enough with the waveform parameters used in these measurements since the capacitive coupling through the substrate is comparable to the current through the device at 1 MHz. There is a trade off between the resolution of the measurements during the melting pulse and the measurement duration, hence, the accuracy in the low temperature range. However, for T ≤400 K, high-resolution DC measurements performed minutes after the pulse yield accurate $\rho_{aGST}$ values since the crystallization times are very long. Small markers are for a separate set of measurements around 520 K.

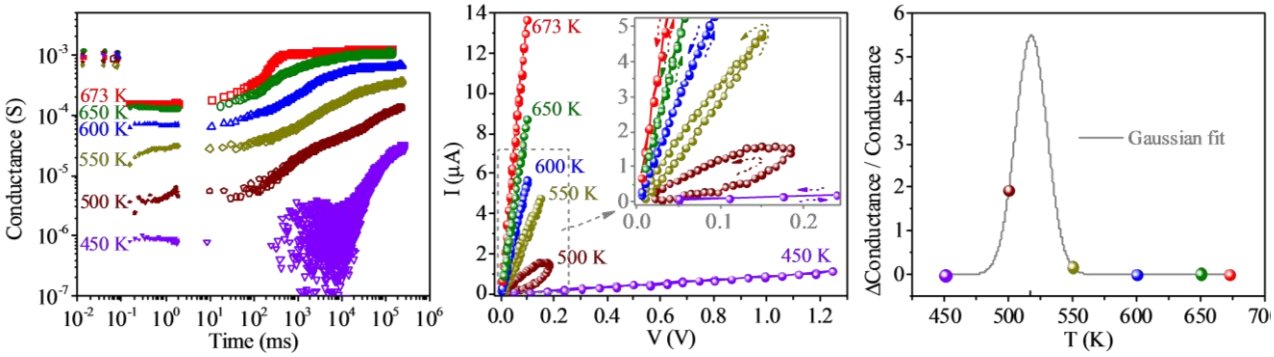


Figure 26. (Left) Conductance calculated from the sinusoid fits during the high-resolution measurements (solid symbols) and long duration DC measurements (open symbols) for a single device. (Middle) I-V characteristics based on the high-resolution measurements for a single device. Inset is a zoomed view highlighting the hysteresis loops seen for T = 500 K and 550 K measurements. (Right) Relative increase in conductance within the measurement time (~ 2ms) as function of chuck temperature and a Gaussian fit to the data.

The device level metastable resistivity data of GST collected by the fast (in the order of ~μs) electrical measurement system developed during the last award period has been further analyzed in this period. In contrast to the typical Arrhenius relationship where the natural log of resistivity is linearly proportional to the inverse of temperature, the natural log of metastable resistivity shows linear relationship with temperature (Figure 27a) suggesting a non-constant activation energy. Surprisingly enough the molten resistivity measured on GST thin film falls right on top of the linear extrapolation of the metastable data supporting the assumption of amorphous GST being a 'liquid state' with a temperature dependent viscosity.

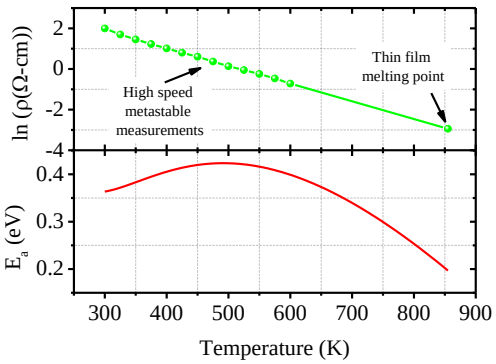


Figure 27. a) Natural log of measured (high speed device level) resistivity as a function of temperature[18]. The last data point is the thin film measurement at melting temperature. b) Extracted activation energy by fitting a third order polynomial to the ln(ρ) vs. $1/k_BT$ data.

Historically the conduction activation energy ($E_a$) in a mixed phase material is calculated as the slope of the Arrhenius plot. $E_A$ is extremely important to explain transport mechanisms in GST [19]–[22]. The temperature independent activation energy of GST is around 0.33 to 0.355 eV [19], [22], [23]. To figure out the metastable activation energy associated with device level operation we developed an algorithm that involves fitting the *ln(ρ)* vs. $1/k_BT$ data with polynomial function, where ρ is the resistivity, $k_B$ is the Boltzmann's constant and $T$ is the temperature. We can write the resistivity using Arrhenius formula,

$$\rho = \rho_0 \exp\left(\frac{E_a}{k_B T}\right) \tag{32}$$

where $E_a$ is temperature dependent, $E_a = E_a(T)$ and $\rho_0$ is the constant pre-factor.

Taking natural log of equation (32) we get,

$$\ln(\rho) = \ln(\rho_0) + \frac{E_a}{k_B T} \tag{33}$$

Differentiation of (33) with respect to $1/k_BT$ yields,

$$\frac{d\ln(\rho)}{d(1/k_B T)} = E_a + \frac{1}{k_B T}\frac{dE_a}{d(1/k_B T)} \tag{34}$$

Now, *ln(ρ)* vs. $1/k_BT$, not being linear for the metastable case, can be fitted with higher order polynomial. As an example, the third order fit gives,

$$\ln(\rho) = a(1/k_B T)^3 + b(1/k_B T)^2 + c(1/k_B T) + d \tag{35}$$

Differentiation of (35) with respect to $1/k_BT$ yields,

$$\frac{d\ln(\rho)}{d(1/k_B T)} = 3a(1/k_B T)^2 + 2b(1/k_B T) + c \tag{36}$$

From (34) and (36) we get,

$$E_a + \frac{1}{k_B T}\frac{dE_a}{d(1/k_B T)} = 3a(1/k_B T)^2 + 2b(1/k_B T) + c \quad (37)$$

The closed form analytical solution of (37) is,

$$E_a = a(1/k_B T)^2 + b(1/k_B T) + c + \frac{Const}{(1/k_B T)} \quad (38)$$

The value of 'Const' is calculated using the room temperature value of activation energy reported in literature [19], [23], [22].

The extracted $E_a$ plotted in Figure 27b is parabolic in nature instead of being constant which signifies different carrier activation processes at different temperature.

### Publications related to this work

#### Journal Articles

F. Dirisaglik, G. Bakan, Z. Jurado, S. Muneer, M. Akbulut, J. Rarey, L. Sullivan, M. Wennberg, A. King, L. Zhang, R. Nowak, C. Lam, H. Silva and A. Gokirmak, "High speed, high temperature electrical characterization of phase change materials: metastable phases, crystallization dynamics, and resistance drift," *Nanoscale, 2015,7, 16625-16630 (*2015).

F. Dirisaglik, G. Bakan, A. Faraclas, A. Gokirmak, and H. Silva, "Numerical modeling of thermoelectric Thomson effect in phase change memory bridge structures," *Int. J. High Speed Electron. Syst.*, vol. 23, no. 01n02, p. 1450004, Mar. 2014.

#### Conference Presentations

F. Dirisaglik, G. Bakan, S. Muneer, N. Williams, M. Akbulut, H, Silva, A. Gokirmak, "Electrical pump-probe characterization technique for phase change materials," 2016 74th Annual Device Research Conference (DRC), DOI: 10.1109/DRC.2016.7548508 (2016).

Faruk Dirisaglik, Gokhan Bakan, Zoila Jurado, Lindsay Sullivan, Sadid Muneer, Mustafa Akbulut, Kadir Cil, Yu Zhu, Chung Lam, Helena Silva, Ali Gokirmak, "High Speed, High Temperature Electrical Characterization of Meta-Stable Phases and Crystallization Dynamics of $Ge_2Sb_2Te_5$," HH5.06 *Mat. Res. Soc. Spring Meeting*, 2014.

## 5. Modeling of Phase Change Memory: Nucleation, Growth and Amorphization Dynamics during Set and Reset: Discrete Grains

We have updated our finite-element simulation framework using COMSOL to capture discrete nucleation and growth of individual grains while tracking crystal orientation and grain boundaries. Nucleation and growth rates are calibrated to match those found theoretically and experimentally in other works [24], but the underlying thermodynamic equations are not explicitly solved in this model. The crystallization approach used here is most similar to phase-field finite-element models based on classical nucleation and growth theory [24]–[28]. This model allows simulation of grain-boundary movement even after the material is fully crystallized via periodic re-amorphization of the grain boundaries. Transport through grain boundaries and crystalline grains is modeled using different resistivity functions in our electro-thermal models [29]–[32], capturing the stochastic nature of polycrystalline materials and percolation transport. We

Table 2: Analysis of Crystallization Results in Figure 28.

| Max. T (°C) | Source | Total Grains | % Area Crystallized | Average Grain Radius (nm) |
|---|---|---|---|---|
| 146 | [4] | 441 | 12.1 | 7.06 ± 4.5 |
| | This work | 275 | 23.4 | 13.4 ± 5.8 |
| 148 | [4] | 961 | 59.9 | 10.8 ± 6.2 |
| | This work | 826 | 61.6 | 11.8 ± 6.9 |
| 150 | [4] | 810 | 75.8 | 13.1 ± 8.2 |
| | This work | 754 | 76.8 | 14.2 ± 7.2 |

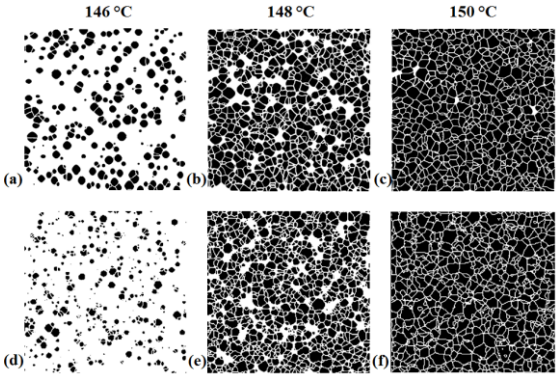


Figure 28. Comparison of simulation results from our nucleation and growth model (a-c) with the model from Burr et al. [24] (d-f), "Observation and modeling of polycrystalline grain formation in $Ge_2Sb_2Te_5$," Journal of Applied Physics, 2012, vol. 111, no. 10, p. 104308-5]) at various temperatures. Indicated temperatures signify the maximum temperature achieved during a 1.3 C/s ramp.

demonstrate our model in this manuscript with 2-D simulations, and the model can be extended to 3-D simulations as well.

Previously we have demonstrated a finite-element approach for simulating set and reset operation of PCM cells that captures thermoelectric effects [29], [33] and general crystallization and amorphization dynamics using an effective media approximation [34]. In earlier works, phase changes are modeled using a rate equation to solve for the crystal density (*CD*) of each mesh element in the geometry during device operation:

$$\frac{dCD}{dt} = Nuc(T, CD) + Grow(T, CD) + Amorph(T, CD) \tag{39}$$

In this effective-media approximation, each mesh element is assumed to represent a volume large enough such that (i) *CD* continuously varies between 0 (100% amorphous) and 1 (100% crystalline), (ii) the nucleation term produces a continuous field which increases *CD* over time according to published nucleation rates [24] and (iii) percolation transport within each mesh element is accounted for by drastically increased electrical conductivity for $CD > 0.3$. Material properties are defined as continuous functions of *CD* and temperature (*T*). This approach is useful for modeling the crystallization and amorphization of large volumes of GST.

However, nucleation probabilities are very small in mesh elements on the order of 1 nm. Hence, a model that can capture nucleation and growth of discrete grains and track grain boundaries is better suited for modeling PCM devices with ~10 nm critical dimensions. Such a model can capture the variability in PCM cells due to variations in crystal grain sizes and distributions.

Discrete nucleation is implemented by updating *Nucleation* in (39) with a periodic activation function. Unlike the method proposed in [25], where nucleation and growth solvers are explicitly separated, here we use a single differential equation (39) to model the changes in the material which is fully coupled with the electro-thermal model as described in Part I. The discrete nucleation model generates random numbers between 0 and 1 and stores them in an array, *rn(x,y,t)*, defined on a square x-y grid for each activation period ($t_{nuc}$). The *Nucleation* term is computed by comparing *rn(x,y,t)* with the nucleation probability ($p_{nuc}$) at each point using a dynamic step-function:

$$Nucleation = 0.8\ \mathrm{ns}^{-1}(1 - CD)(rn(x,y,t) < p_{nuc}) \quad (40)$$

$$p_{nuc} = (I_{ss}(T))(Vol_{nuc})(t_{nuc}) \quad (41)$$

where $I_{ss}$ (nuclei·m$^{-3}$·s$^{-1}$) is the published temperature dependent steady-state nucleation rate [24]. $Vol_{nuc}$ (nucleation site volume) is determined by the grid size used for *rn(x,y,t)* and an assumed depth. This technique approximates nucleation as a phenomenon that occurs at discrete time intervals with period $t_{nuc}$. If $rn(x,y,t) < p_{nuc}$ then nucleation of a crystal grain initiates at that site. This causes *Nucleation* in (39) to increase *CD* at a chosen rate of 0.8 ns$^{-1}$, fast enough to capture device switching dynamics while being computationally efficient (Figure 30a).

Once the nucleation of a crystal grain is initiated and *CD* reaches a significant value (~0.1), *Growth* in (39) rapidly brings *CD* to 1 at that mesh point, completing nucleation. The $\nabla\cdot(\nabla CD)$ term of *Growth*, as described in Part I, then becomes large at the edges of the nucleated grains, initiating templated growth (Figure 30b-e).

The value of *Growth* at the expanding grain edge is temperature dependent. In the example shown in Figure 30, *Growth* increases *CD* at a rate of 0.5 ns$^{-1}$, bringing *CD* to 1 in 2 ns at the grain interface, resulting in the expected growth velocity of 0.5 m/s at 600 K [24].

The activation period $t_{nuc}$ should be small enough that nucleation probability is negligible within the volume that will crystallize through growth of existing grains during $t_{nuc}$. We use $t_{nuc}$ = 5 ns for simulations of device operation, and we choose $t_{nuc}$ at time $t_k$ such that on average a single nucleus will appear within a certain volume (*Vol*) for simulations of long duration anneals:

$$\int_{t_k}^{t_k+t_{nuc}} \int_{Vol} p_{nuc}\, dVol\, dt \cong 1 \quad (42)$$

Since $p_{nuc}$ is temperature dependent, $t_{nuc}$ must be updated dynamically in simulations of ramped temperature anneals.

*Amorphization* in (39) is adapted from Part I to rapidly reach *CD* = 0 at locations where $T \geq T_{melt}$ (873 K).

We use nucleation and growth rates from [24], where Burr *et al.* use a more fundamental but computationally expensive cellular automata approach that calculates the surface energy density and bulk free energy difference between crystal grains and surrounding amorphous areas. Our model gives similar results (Figure 28, Table 2) and
is suitable for modeling crystallization dynamics coupled with electro-thermal physics in nanoscale devices.

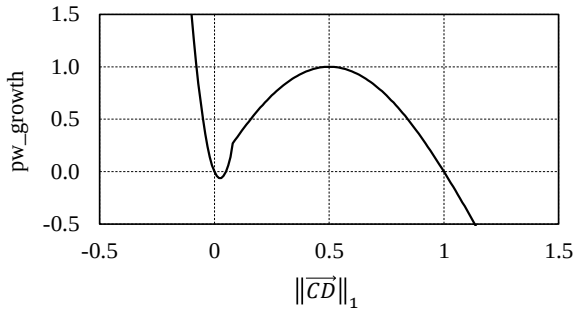


Figure 29. pw_growth($\|\overrightarrow{\boldsymbol{CD}}\|_1$) constrains each component $CD_i$ such that $\|\overrightarrow{\boldsymbol{CD}}\|_1$ is stable at 0 and 1.

Previously we have used a scalar variable *CD* to model crystalline density. Here, we define crystalline density as a vector $\overrightarrow{CD} = \{CD_1, CD_2, CD_3\}$ to model crystallinity and grain orientation simultaneously. The one-norm of $\overrightarrow{CD}$, $\left\|\overrightarrow{CD}\right\|_1$, is used to define local crystallinity:

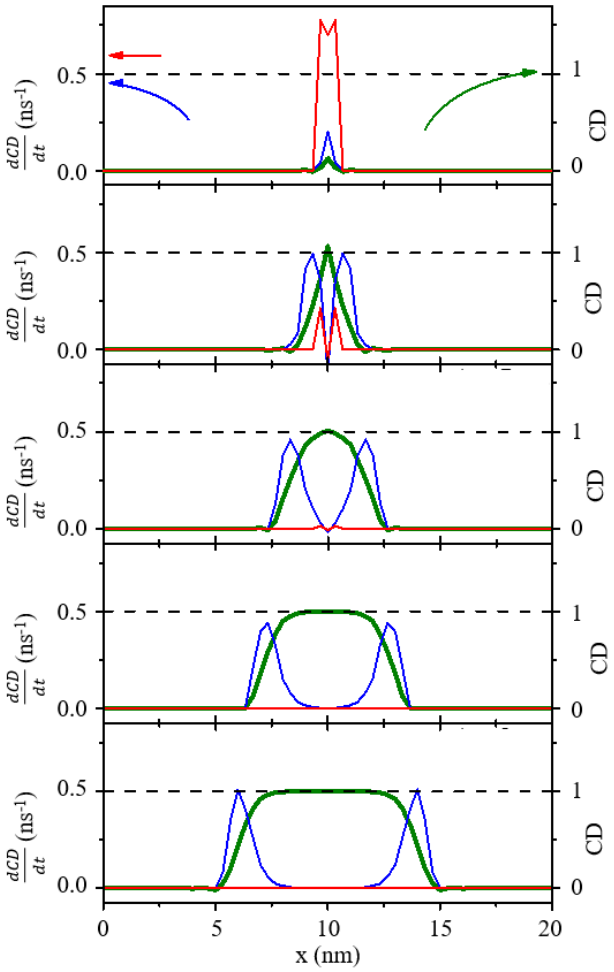


Figure 30. Visualization of time evolution of the nucleation and growth of a discrete grain showing the contributions of the *Nucleation* and *Growth* terms at 600 K.

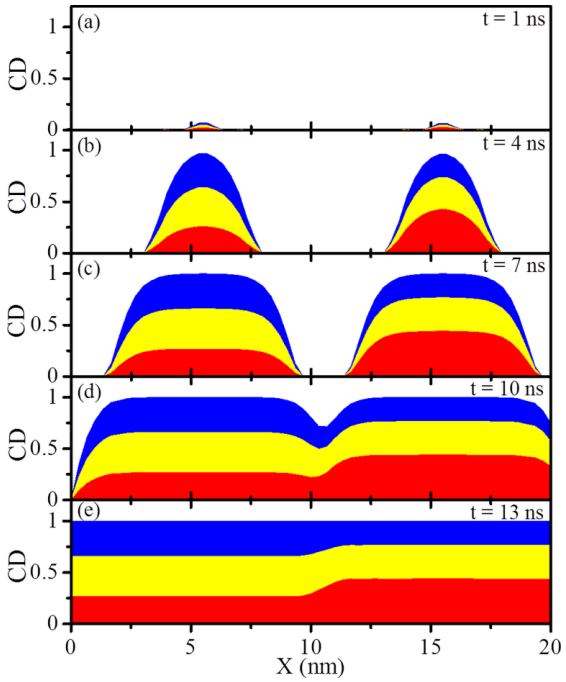


Figure 31. Time evolution of nucleation and growth of two expanding grains with unique, randomly generated $CD_i$ components (each shown as a different color) indicating individual grain orientations.

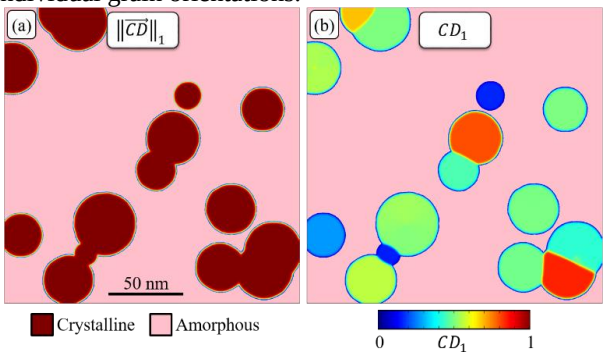


Figure 32. Simulated anneal of a 200 nm square of GST. (a) The one-norm of *CD* is used to identify crystalline (red) and amorphous (pink) material. (b) $CD_1$ has different values for individual crystalline grains, and can be used to distinguish grains with different orientations.

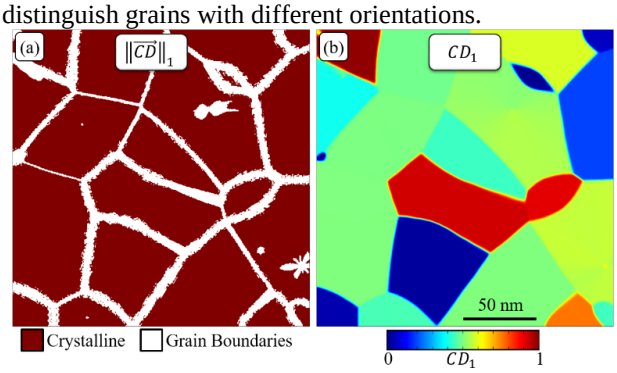


Figure 33. Fully annealed 200 nm square of GST. (a) One-norm of *CD* (red) with grain boundaries overlaid in white. (b) Grain orientation presented in the form of $CD_1$.

$$\left\|\overrightarrow{CD}\right\|_1 = CD_1 + CD_2 + CD_3 \qquad (43)$$

with $\left\|\overrightarrow{CD}\right\|_1 = 0$ and $\left\|\overrightarrow{CD}\right\|_1 = 1$ corresponding to fully amorphous and fully crystalline states respectively. The rate equation used to track crystallinity used previously is adapted to track each component $CD_i$:

$$\frac{dCD_i}{dt} = Nucleation_i\left(T, \left\|\overrightarrow{CD}\right\|_1, rn_i\right) + Growth_i\left(T, \left\|\overrightarrow{CD}\right\|_1, \nabla^2 CD_i\right) + Amorphization_i\left(T, \left\|\overrightarrow{CD}\right\|_1, CD_i\right) \qquad (44)$$

which solves for all 3 components simultaneously. *Growth*$_i$ is scaled by the control function *pw_growth* (Figure 29) to constrain $0 \le \left\|\overrightarrow{CD}\right\|_1 \le 1$. Upon nucleation with (2), a nucleus is assigned a random distribution of $\overrightarrow{CD}$ components ( Figure 31 a,b).

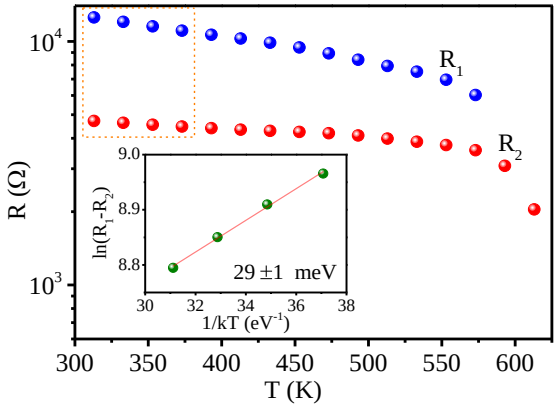


Figure 34. Experimental resistance-temperature (R-T) characteristics of a crystalline GST 50 nm thin film annealed at 553 K ($R_1$) and 593 K ($R_2$) obtained using a high-temperature Seebeck measurement setup [35]. We assume that subtracting the resistance of $R_2$ from $R_1$ eliminates the contribution of crystal grains; hence the grain boundary activation energy can be calculated using an Arrhenius relationship for ($R_1$-$R_2$) below glass transition temperature (~370 K [36]). A grain boundary activation energy of ~29 meV (inset) is obtained.

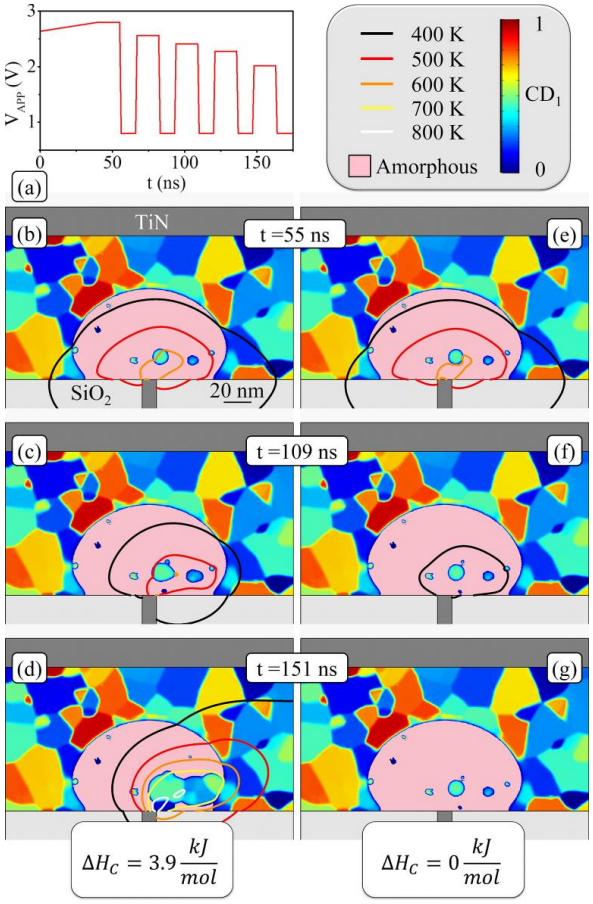


Figure 35. A series of set pulses (a) with a baseline is applied to a pre-nucleated amorphized mushroom cell with heat of crystallization on (b-d) and off (e-g). Heat of crystallization enhances thermal runaway, leading to higher temperatures and more crystallization. Contours show temperature in 100 K increments as indicated.

*Growth*$_i$ is scaled by $\frac{CD_i}{\|\overrightarrow{CD}\|_1}$ to preserve the correct component distribution as grains expand (Figure 31c,d) and terminated by *pw_growth* when $\|\overrightarrow{CD}\|_1 = 1$ to halt growth where crystalline grains meet. The result is a uniform field of $\|\overrightarrow{CD}\|_1 = 1$ (Figure 31e, Figure 32a) and discontinuous $CD_i$ values at grain boundaries (Figure 31e, Figure 32b). $|\nabla\overrightarrow{CD}|$ is typically <$10^{-3}$ nm$^{-1}$ within individual grains and ~0.5 nm$^{-1}$ at grain boundaries. We define grain boundaries where $\|\nabla\overrightarrow{CD}\|_1 \geq 5 \times 10^{-3}$ nm$^{-1}$, capturing the vast majority of boundaries. The identified grain boundaries have an average thickness of ~2 nm (Figure 33).

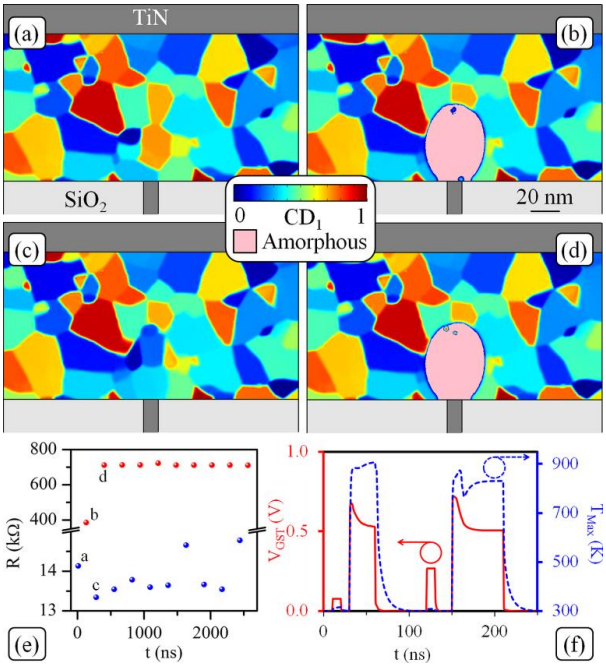


Figure 36. Grain maps for set (a,c) and reset (b,d) states in a 10 nm mushroom cell. Cycle-to-cycle resistance for set (blue) and reset (red) states over 10 cycles is shown in (e). The voltage difference between the top and bottom TiN contacts and the maximum temperature within the GST for the first cycle are shown in (f).

## Simulations

We demonstrate our crystallization model with grain boundary physics and heat of crystallization, in addition to the Joule heating and thermoelectric effects [29], [33], [37] described in Part I, on mushroom cells with 10 nm heaters. A temperature dependent activation energy term is included at grain boundaries to capture transport limited by thermionic emission [38]:

$$\sigma_{GB} = A\sigma_c e^{\frac{-E_a}{k_B T}} \tag{45}$$

where $k_B$ is the Boltzmann constant and $\sigma_c$ = 145 Ω$^{-1}$cm$^{-1}$ is used as the conductivity of crystalline GST. The activation energy $E_a$ is calculated as 29 meV from a series of R-T measurements (Figure 34) [39]. A scaling factor $A$ = 4 is used to account for the difference between the ~2 nm grain boundary thicknesses in our simulations and the expected thickness of ~0.5 nm [26], so that the total grain boundary resistance is captured correctly.

GST releases energy during crystallization as it relaxes into a lower energy state. An external heat source $Q_0$, dependent on the time derivative of $\overrightarrow{CD}$, is used to model this latent heat of crystallization ($\Delta H_c$):

$$Q_0 = \begin{cases} 0, & \frac{d\|\overrightarrow{CD}\|_1}{dt} \leq 0 \\ \alpha * \frac{d\|\overrightarrow{CD}\|_1}{dt}, & \frac{d\|\overrightarrow{CD}\|_1}{dt} > 0 \end{cases} \tag{46}$$

where α = 23.5 MW/m$^3$ to match $\Delta H_c$ = 3.9 kJ/mol [40]. The heat source is turned off upon amorphization as the latent heat of fusion during melting is already modeled by an increase in the heat capacity, as described in [28], [29], [40].

The temperature difference at growth fronts during steady state crystallization due to $\Delta H_c$ is relatively small (~1 K). However, $\Delta H_c$ can significantly impact the formation of percolation paths that experience high thermal gradients and thermal runaway [41] during rapid set operation in nanoscale

devices. We illustrate this by applying a series of steadily decreasing set pulses (Figure 35a) to a reset mushroom cell with (Figure 35 b-d) and without (Figure 35 e-g) modeling $\Delta H_c$.

Stochastic nucleation and growth dynamics cause variations in percolation paths and grain maps. Hence, the time and power necessary to cycle a device and the set and reset resistances can vary significantly. An example of the cycle-to-cycle variations in both set and reset states is presented in Figure 36. The relative standard deviation of all reset state resistances after the first cycle is ~0.5%. The first reset state (Figure 36b) resistance is ~46% below the others due to nucleation near the heater. Grain boundary resistances contribute proportionally more to the total resistance in the set state than in the reset state; hence the set state is more sensitive to grain map changes leading to a ~4% cycle-to-cycle deviation.

## Publications related to this work

### Journal articles

A. Faraclas, G. Bakan, H. Adnane, F. Dirisaglik, N. E. Williams, A. Gokirmak, H. Silva, L. Adnane, F. Dirisaglik, N. E. Williams, A. Gokirmak, and H. Silva, "Modeling of thermoelectric effects in phase change memory cells," *IEEE Trans. Electron Devices*, vol. 61, no. 2, pp. 372–378, Feb. 2014.

G. Bakan, A. Gokirmak, H. Silva, *Suppression of thermoelectric Thomson effect in silicon microwires under large electrical bias and implications for phase-change memory devices, Journal of Applied Physics* 116, 23, 234507 (2014)

F. Dirisaglik, G. Bakan, A. Faraclas, A. Gokirmak, and H. Silva, "Numerical modeling of thermoelectric thomson effect in phase change memory bridge structures," *Int. J. High Speed Electron. Syst*., vol. 23, no. 01n02, p. 1450004, Mar. 2014.

Z. Woods and A. Gokirmak, "Modeling of Phase Change Memory: Nucleation, Growth and Amorphization Dynamics during Set and Reset: Part I - Effective Media Approximation" *IEEE Trans. Electron Devices*, 2017 (Accepted).

Z. Woods, J. Scoggin, A. Cywar, L. Adnane, and A. Gokirmak, "Modeling of Phase Change Memory: Nucleation, Growth and Amorphization Dynamics during Set and Reset: Part II – Discrete Grains," *IEEE Trans. Electron Devices*, 2017 (Accepted).

### Conference presentations

Z. Woods, A. Gokirmak, "Modeling of Phase Change Memory Devices Using a Dynamic Crystal Density Approach," HH2.08 *Mat. Res. Soc. Spring Meeting*, 2014.

A. Cywar, S. Fischer, A. Gokirmak, "Dynamic Crystallization Model for Ge2Sb2Te5 Nanostructures," HH6.04 *Mat. Res. Soc. Spring Meeting*, 2014.

# 6. High-temperature characterization of relevant materials

## Development of high temperature material characterization tools

### *Seebeck measurement setup*

The high temperature Seebeck coefficient and resistivity measurement setup was constructed using materials available in our laboratory (stepper motors, metal parts, etc.) and common inexpensive items (e.g. I/O cards, thermocouples, Pyrex cookware, copper tubing, cartridge heaters and an inductive cooktop (Figure 37). The measurement setup was the topic of a journal paper [42] and was discussed in few conference presentations. Measurement technique is based on the linear approximation of the proportionality constant $S$ between the open circuit voltage $V_0$ and the temperature difference $\Delta T$ across a sample [43]. The sample holder in the setup is a brass chuck (non-magnetic disc) of 87 mm diameter and 10 mm height, put on top of two steel plates and supported by a high temperature glass-ceramic base. The L shape probe arms are screwed to a ceramic glass plate for electric isolation (not shown in the figure) then attached to the chuck to minimize the effect of vibrations on the electrical contacts. Tapered tungsten probes of 2.4 μm tip radius and 45 degree angle are attached to the probe arms and gently pressed against the surface of the sample to form electrical contacts (Figure 37). Two Omega K-type thermocouples of 0.5 mm diameter tip are clamped laterally to each side of the sample. The electrical probes are then carefully aligned to be centered with the thermocouple probed spots (Figure 37). For some samples, lithographically patterned metal contacts were also used to set the distance between the probes. A distance of 20 mm between the two sides of the sample is sufficient to achieve a temperature difference ΔT ~10 °C. Signal and ground lines of coaxial cables are connected directly to the corners of the probe arms.

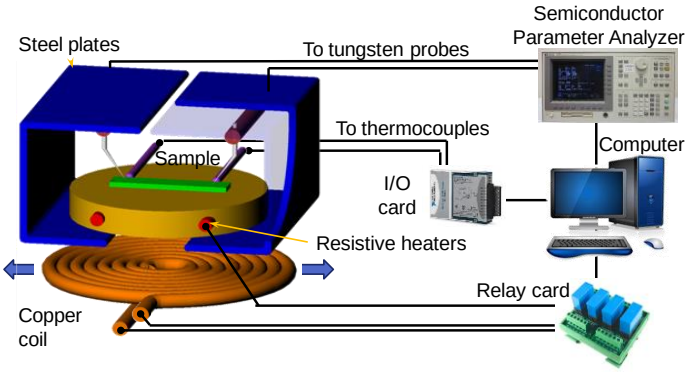


Figure 37. Schematics of the high-temperature Seebeck coefficient and resistivity measurement setup. Two C-shaped surrounding steel plates form an enclosure for heat confinement and probe arms heating (with either resistive or inductive heating). The probe tips on the surface of the sample are centered with the thermocouples probed spots. The actual setup has 4 probe arms and 4 thermocouples so that two samples can be measured at the same time. Resistive or inductive heating can be used. With inductive heating, the non-magnetic chuck (brass alloy) is heated by contact to the steel plate which in turn is heated by the AC magnetic field generated by the water cooled copper pipe coil underneath. The measurement area is enclosed in low vacuum chamber surrounded with a glass shield filled with nitrogen (not shown in the schematic).

For resistive heating two cartridge heaters of 300 Watt each are inserted in either side of the chuck and controlled individually using a relay card to heat and establish a temperature gradient in the sample. The distance of ~ 70 mm between the two heaters allows us to generate a temperature difference of ~ +/- 20 °C going from one side to the other. By adjusting the On/Off time periods for each heater the temperature difference is controlled and stabilized along with the heating rate and the average temperature. The temperature profile on the chuck is simulated and examined with COMSOL Multi Physics. Finite element simulation of heat transfer in a brass chuck (same dimensions as the one used in the setup) is solved with time dependent heat transfer model. Temperature profile is represented in the inset of Figure 38. The thermal inertia and the temperature diffusion inside the chuck keep the temperature almost linear

on the surface between the heaters while tuning the temperature gradient. For a temperature difference of 10 ºC between the heaters at an average temperature of 95 ºC, the temperature versus distance on the surface of the chuck is given in Figure 38. This profile justifies taking the average temperature between the two sides of the sample as the average temperature of the chuck.

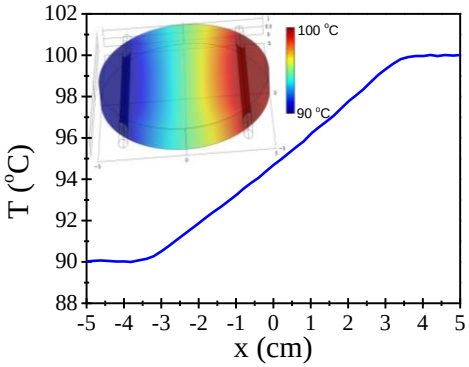


Figure 38. Temperature on the surface of the chuck along the diameter perpendicular to the heaters simulated after 60 s by setting the temperature of the resistive heaters to 100 °C in one side and 90 °C in the other. The inset represents the temperature profile of the chuck.

For inductive heating, a water cooled copper planar coil positioned underneath the chuck and supported by a motorized stage is used to generate a high frequency (160 KHz) magnetic field that heats the steel C-shaped plates surrounding the test area which in turn heat the non-magnetic chuck by direct contact (Figure 37). The water cooled planar coil was made using spiral copper tube isolated with Kapton tape and can withstand chuck temperatures ~ 800 °C. To control the sample temperature, the switching of the heater is controlled through the relay card while the temperature gradient along the sample is adjusted by the position of the coil underneath the chuck. The temperature gradient was found to be in direct relation with the number of steps completed by the stepper motor within a certain range (~ 3cm right or left from the center). The inductive heater is turned off (through the relay card) during each measurement to avoid possible interferences and magnetic field effects on the sample or probes materials (e.g. bismuth–antimony alloys in thermocouples)[44].

The setup is fully automated using a LabVIEW interface. The regulation of temperature starts when it reaches 80% of the target. The maximum temperature reached with the setup is ~ 750 °C. When the temperature is stabilized around the target and the temperature gradient is set across a semiconductor sample, the I-V characteristics measured with a semiconductor parameter analyzer (PA) provide us simultaneously with the Seebeck voltage, which is the x-axis intercept of the linear fit of the data, and with the resistance between the two contacts which is the slope of the linear fit. The advantage of using the PA is that the x-intercept of the I-V curve is not modified by the contact resistance. Two samples can be measured simultaneously using the 4 Source Monitor Units (SMUs) of the PA. The temperature on the surface of the sample is examined with COMSOL (heat transfer simulation) and it is found to be very close to the temperature of the chuck.

### *Hall measurement setup*

The measurement of the Hall coefficient enables determination of carrier type and carrier concentration along with the carrier mobility in a material. Like the previously described Seebeck coefficient measurement setup, the developed high temperature hall coefficient measurement setup was the topic of a journal paper [45] and was discussed in few conference presentations. Multiple measurements on single crystal low doped silicon sample show good agreement with published data. Based on the van der Pauw technique [46], the electrical resistivity and Hall coefficient are simultaneously extracted from multiple current-voltage measurements performed by a PA. The fully automated setup uses rare earth permanent magnets for constant magnetic field generation and can reach up to ~500 ºC sample temperature, limited by the power of the heaters, heat conduction along the chuck, and oxidation of the electrical contacts. The setup consists of three main parts: The sample holder with heating elements, the movable stage with the magnetic frame, and the electronic control and data acquisition components.

The sample holder is a brass chuck of 6 cm × 1 cm × 22 cm laying on a glass-ceramic base of 10 cm × 0.4 cm × 28cm and enclosed in a measurement chamber (Figure 39). Two cartridge heaters of 300 Watts each are insert in one end of the chuck while the other end is designed to support samples. 4 electrical probes are attached to the top surface of the ceramic base and connected to coaxial cables from the bottom of the base. The contacts are articulated in the middle so they can be positioned to measure square samples between 1 mm and 25 mm side-length. Two thermocouples are clamped to the chuck surface, one between the heaters for temperature regulation and the other close to the sample (1~2 mm) to record the sample temperature. When the temperature near the heaters is stable around the target, the system waits for 10 minutes during which the temperature of the sample asymptotically and without rippling approaches a stable value. This is important for characterization of materials that undergo irreversible changes with temperature, such as phase-change compounds. When the measurement at a given temperature is complete the target temperature is increased to the next step. The system repeats the stabilization tasks with measurements until the final temperature cycle. The chuck is enclosed by an aluminum cover, sealed on top of the ceramic base, to prevent light straying and to form a chamber that is filled with nitrogen to reduce oxidation of the samples and setup components at high temperatures. An opening along the center of the chuck drives nitrogen from the heaters side to the sample side inside the chamber.

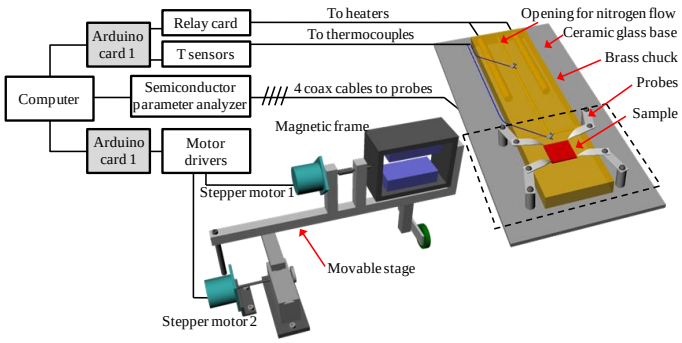


Figure 39. Schematic of the Hall measurement setup. On the right is the chuck sitting on a ceramic glass support. The dashed line determines the region that is insert between the magnets of the movable stage to apply a magnetic field to the sample. The 4 coax cables are connected to the probes from underneath the glass support.

The movable magnetic frame is controlled with two stepper motors to apply an 'up', 'down' or 'no' field to the samples (Figure 39). Two N42 grade neodymium magnets, 4 inch × 2 inch × 1 inch thick rare earth NdFeB blocks that can provide a maximum field of 1.32 Tesla each, with an operating temperature up to 80 °C, are fixed on the horizontal walls of an iron rectangular frame that measures 9 cm by 15 cm inside, 10.5 cm by 16.5 cm outside, and 6.3 cm in depth (Figure 40). The gap between the two magnets is about 3 cm so the magnetic frame can be freely moved to surround the sample holder. The magnetic frame is fixed on an aluminum movable stage from the 2 vertical sides through an axis in two bearings connected to a stepper motor to flip the magnetic field direction between 'up' and 'down', normal to the surface of the sample.

For the electronic control of the system, the setup uses two Arduino Mega 2560 cards[47] connected through USB to a computer. One card is used to measure temperature from the two thermocouples as described before, and to generate switching pulses for the relay card for temperature control and stabilization. The second card is used to drive the stepper motors to apply or remove the magnetic field. The two cards, as well as an HP 4145B semiconductor PA are simultaneously controlled with the measurement computer through a LabVIEW interface. Once the temperature is stabilized within a given range, the stepper motors move the magnetic frame to the sample and the

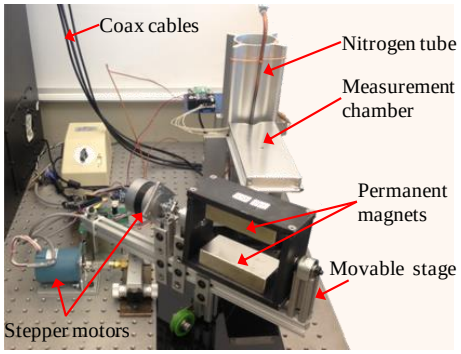


Figure 40. Optical image of the measurement setup. The white mark on the magnetic frame indicates that the magnetic field is directed up between the magnets.

PA performs an I-V and transfers the data to the computer. Articulated electrical contacts allow measurements on different size samples, from ~ 2 mm to 25 mm side length

To avoid the influence of minority-carrier injection on the measurements, the current passing through the sample is maintained low enough to get linear I-Vs as discussed in ref [48]. Bipolar thermomagnetic effect, or Ettingshausen effect [43], [49] may also introduce an error in Hall coefficient measurements for the case of intrinsic semiconductors or semimetals. This effect refers to the potential that is created in addition to the Hall potential if there is a temperature difference between the voltage measurement points ($\Delta V = - S.\Delta T$, where $S$ is the Seebeck coefficient). It is usually very small and considered a minor effect [49], [50] especially in cases of expected uniform thermal profile as in our case where the sample sits on a large metal chuck. The flow of nitrogen through the chuck into the sample chamber helps create a uniform temperature environment. Additional thermocouples may be installed around the sample to account for this contribution in materials or setups where this Seebeck voltage may be significant.

The temperature between the heaters follows the target closely (with rippling of ± 4°C at 700 °C) while the temperature close to the sample is significantly lower ( ~ 315 °C and 510 °C at chuck temperatures of 400 °C and 700 °C). The temperature difference between the surface of the sample and the surface of the chuck is expected to be insignificant based on finite element simulations. The increase in sample temperature during the time it takes to complete the measurement is ~1 ºC at 400 ºC and less than 2 at 500°C which is acceptable since it is in the order of the tolerance of the thermocouples used.

### Simultaneous R-T and S-T measurement on GST

Continuously increasing temperature measurements of R(T) were performed on 50 nm, 100 nm, and 200 nm GST thin films up to the melting temperature and scaled to resistivity ρ(T), represented in Figure 41, using the room-temperature resistivity value after anneal at 200 °C. During these measurements the temperature was increased with a constant rate of 5 °C/min. The two transitions, from amorphous to fcc and from fcc to hcp correspond to the turning points in the curves, and occur at ~155°C and ~365°C respectively. The as-deposited amorphous films have room-temperature resistivity ~ $8.7 \times 10^2$ Ω.cm, in agreement with reported literature values of $8 \times 10^2$~ $9 \times 10^2$ Ω.cm [14]. The films typically become discontinuous after the melting temperature at 600 °C. The drop in the resistivity curve after 585 °C (Figure 41 inset) indicates that the film is molten and the liquid resistivity at this point is 1.14 mΩ·cm, also in agreement with previously reported values for liquid GST resistivity [17], [51]. Film thickness reduction from density change at the first transition was reported ~ 5% [52] but not taken into account in our calculations.

The R(T) curves of the GST films show a drop in resistance of more than five orders of magnitude as the material transitions from amorphous to fcc and hcp crystalline phases whereas this ratio is only approximately four orders of magnitude in GST devices[17]. This difference is attributed to the melt-quench amorphization process in small-scale devices through electrical pulses, which leads to lower atomic disorder,

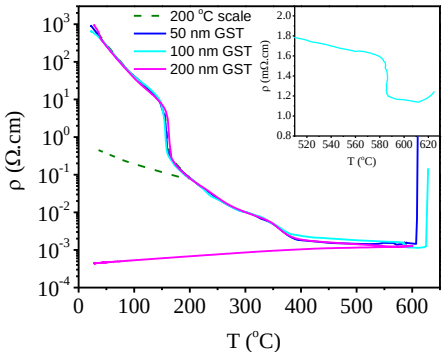


Figure 41. GST resistivity variation with temperature. For the green curve, the 100 nm thin film sample heated up to 200 °C and cooled down; the curve is scaled to the resistivity value at room temperature after cooling. For the red curve, the same procedure for the same sample up to 300 °C. Other curves are the 4 point resistance measurement obtained with heating rate of ~5°C/min, scaled to resistivity.

hence lower amorphous resistivity to start with, compared to as-deposited amorphous films.

In order to characterize the temperature-dependent resistance R(T) and Seebeck coefficient S(T) of the material at each crystalline state as the material progressively changes from amorphous to crystalline, measurements during multiple heating and cooling cycles with increasingly maximum temperature were performed (Figure 42a and b). The R(T) and S(T) characteristics were obtained simultaneously from 2-point I-V measurements performed on 2 samples using a PA. Due to the required thermal gradient, and for practical experiment times, the measurements are performed from 40 °C in 10 °C increments up to 300 °C and in 20 °C increments above 300 °C. The final temperature was set to 180 °C for the first cycle and was increased by 20 °C for each subsequent cycle.

The R(T) characteristics show the expected exponential decrease in resistance with increasing temperature, within each crystalline state, as the material progressively crystallizes from amorphous to fcc and from fcc to hcp [53], [54]. Given the large carrier concentration in GST [55], [56], the overall decrease in resistance from one annealing cycle to another is expected to be mostly due to the increase in mobility with crystallization. After the fcc to hcp transition (last four R-T curves) the material shows a metallic behavior with the resistance increasing with temperature due to mobility degradation with increasing phonon scattering. These results are in agreement with reports in the literature of metallic behavior of hcp-GST, observed as a positive temperature coefficient of resistivity [13],[18],[19]. Assuming an Arrhenius dependence of conductivity on temperature below the glass transition temperature (reported ~100 °C [36]), the conductivity of the material in the exponential regions can be expressed by:

$$\sigma = \sigma_0 e^{-E/kT} \tag{47}$$

where $E$ is the conduction activation energy, $k$ is the Boltzmann constant, $T$ is the absolute temperature, and $\sigma_0$ is defined as the minimum metallic conductivity [59]. In the amorphous phase, the activation energy $E$ is thought to include the activation energy for hopping mechanisms which do not occur in *fcc* and *hcp*-GST based on UV/visible/NIR band gap measurements [60]. The activation energy for conduction obtained for the amorphous phase from the first cycle, $E$=0.417 eV, is in agreement with reported values [61] and it

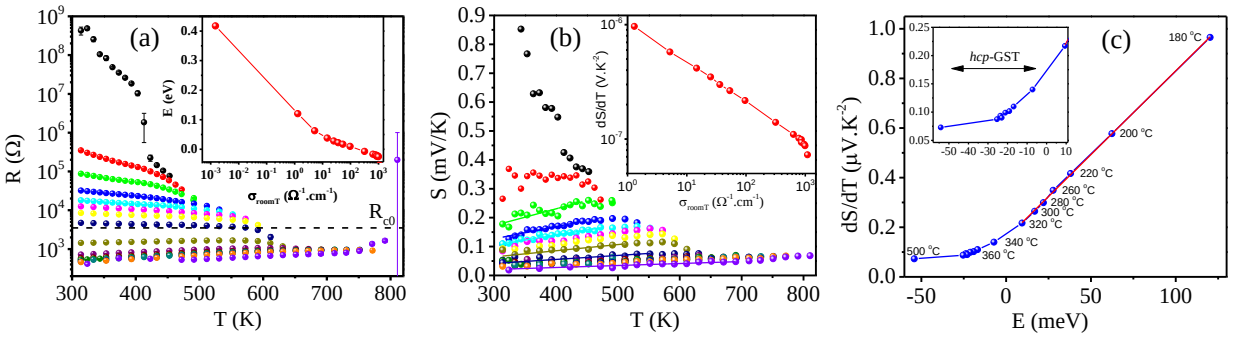


Figure 42. a) 50 nm GST sample resistance measured multiple times to increasingly maximum temperature. The measurements were performed in steps of 10 °C for the first measurements up to 200 °C, 20 °C step up to 520 $^0$C, and 50$^0$C step initially for the last measurement up to 540 °C. The temperature is stabilized at each step for ~20 min while/before measuring the Seebeck coefficient. The dashed line represents the resistance value of the sample at the second transition temperature ($R_{c0}$). The inset in the graph shows the conduction activation energy, obtained from the slopes of the linear fit of ln(R) vs. 1/kT, as a function of the conductivity of the sample at room temperature, b) 50 nm GST Seebeck coefficient variation with temperature measured simultaneously with the resistance of the sample given in a. The inset represents the slopes dS/dT plotted as function of the conductivity of the sample at room temperature, and c) Evolution of the slopes of Seebeck curves with the activation energy E for 50 nm GST thin film. The inset represents a zoom in plot on the negative values of E where the GST switched into the hcp phase. Notice for positive values of E (fcc-GST) the relation dS/dT-E is linear with an intercept of 0.155 μV/K$^2$.

decreases as the material crystallizes in the following cycles of increasingly maximum temperatures (inset in Figure 42a).

Figure 42b shows the S(T) measurement results obtained simultaneously with the R(T) results. Once the material starts crystallizing (from the first heating-cooling cycle onward), and for each state (corresponding to the material annealed at the previous cycle maximum temperature) the Seebeck coefficient increases approximately linearly with temperature, before a higher temperature is reached and further material changes occur due to continuing crystallization. Linear fits of these linear region in the S-T curves with fixed zero intercept (0 mV/K @ 0 K) present very small relative standard deviation errors on the slopes (0.6~3.7%). The observed linear dependence of the Seebeck coefficient with temperature is in agreement with that obtained within the Boltzmann approximation transport model for degenerate semiconductors[62]–[64]:

$$S = \frac{8\pi^2 k_B^2}{3qh^2} m^* T \left(\frac{\pi}{3n}\right)^{2/3} \quad (48)$$

where $k_B$ is the Boltzmann constant, $h$ is the Plank constant, $q$ is the elementary charge, $n$ is the carrier concentration, $m^*$ is the carrier effective mass, and $T$ is the absolute temperature.

The derivative dS/dT, in turn, shows a strikingly linear dependence on the conductivity activation energy (Figure 42c) which suggests a linear relation between the effective mass and this activation energy (in the crystalline state region where this energy is positive and may be a meaningful conduction parameter). This observation can be used to empirically determine the temperature dependence of conductivity or Seebeck coefficient of a given mixed-phase state GST based on a single room-temperature measurement of the Seebeck coefficient or conductivity measurements at a few low temperature points (to obtain E).

The positive Seebeck coefficient obtained for the GST films confirms the p-type conduction of the material up to the maximum measured temperature of ~ 800 K. The S(T) decrease with temperature for the amorphous phase, as well as the increase with temperature for the stable *hcp* phase, are in agreement with previously reports [51], [57]. For the *fcc* phase however, these multiple stepped measurements show that the Seebeck coefficient also increases with temperature for a given crystalline state, up to the maximum temperature reached in the previous cycle. The decrease of S(T) with temperature observed in continuous measurements (such as those shown in Figure 42b, and also previously reported for different anneal temperatures [65], [66]) is therefore due to crystallization-related material changes, rather than bipolar conduction which explains the turn-around in stable semiconductors as they approach the intrinsic regime. The positive S(T) slope we observe for the crystalline material (both *fcc* and *hcp*) is consistent with observations of asymmetric amorphization of PCM line cells toward the higher potential terminal [33], [67], [68]

### Percolation model and correlation to the grain size

Since the increase of average grain size in *fcc*-GST is only from ~18 to ~30 nm [69], the drastic change in conductivity observed at the amorphous to *fcc* transition is likely due to percolation paths that form in the material as both the number of grains and the grain size increase. Conductivity of an inhomogeneous material formed by two different materials with different properties was described in late 1800's by Rayleigh [70] and Wiener [71] and then formulated into the effective-medium theory by Bruggeman [72] for various shapes and by Landauer [73] for spheres of conductivity $\sigma_c$ embedded in a material of conductivity $\sigma_a$. The model was adopted recently for mixed phase amorphous-crystalline chalcogenides like GST[74]. In this work, we model mixed phase amorphous-fcc GST as spheres of fully crystalline *fcc*-GST

embedded in amorphous GST and use the average grain sizes obtained from XRD measurements as the diameter of the spheres. The conductivity of the mixed material in this case is given by [72]–[75].

$$\sigma = \frac{1}{4}\left[2\sigma_p - \sigma_q + \sqrt{\left(2\sigma_p - \sigma_q\right)^2 + 8\sigma_a\sigma_c}\right] \tag{49}$$

with

$$\sigma_p = (1-f)\sigma_a + f\sigma_c$$
$$\sigma_q = (1-f)\sigma_c + f\sigma_a$$

where $\sigma_c$ is the conductivity of the crystalline spheres, $\sigma_a$ is the conductivity of the amorphous GST, and $f$ is the crystallinity fraction of the material (fraction of the crystalline volume to the total volume of the sample).

Solving equation (6) for $f$ yields:

$$f = \frac{(\sigma - \sigma_a)(2\sigma + \sigma_c)}{3\sigma(\sigma_c - \sigma_a)} \tag{50}$$

which can be written in terms of the resistances assuming a constant geometry factor $C$, $\sigma = C/R$ as:

$$f = \frac{(R_a - R)(R + 2R_c)}{3R(R_a - R_c)} \tag{51}$$

where $R$, $R_a$, and $R_c$ are the resistances of the mixed phase, the amorphous, and the fully crystalline fcc GST respectively.

The resistance of the mixed phase material at each crystallinity fraction $f$ follows an Arrhenius dependence:

$$R = R_0 \exp(E/k_B T) \tag{52}$$

with $R_0$ and $E$ are the pre-factor and conduction activation energy of the mixed material. The parameters for amorphous GST $R_{a0}$ and $E_a$ are obtained from the first R-T measurement on the amorphous film:

$$R_a = R_{a0} \exp(E_a/k_B T) \tag{53}$$

The resistance of fully crystalline *fcc*-GST is assumed to be constant with temperature (E = 0 eV) since the activation energy is observed to change from positive values for mixed amorphous-fcc phase to negative values for mixed fcc-hcp phase (see dashed lines in Figure 42a). The constant resistance value for fully crystalline *fcc*-GST is taken as the resistance at the second transition temperature obtained from the zero of the second derivative of the 'envelope' of the R-Ts (formed by the last data point from each cycle).

$$R_c = R_{c0} \tag{54}$$

The different parameters, $R_{a0}$, $E_a$, and $R_{c0}$ are given in Table 1 for the 50nm and 200 nm thick films and are used to calculate the crystallinity fraction $f$ of the sample as a function of temperature from equation (54).

Table 3: Extracted parameters from the measurements.

| | 50 nm thin film | 200 nm thin film |
|---|---|---|
| $R_{a0}$ (Ω) | 77.05 | 56.99 |
| $E_a$ (meV) | 419.8 | 376.7 |
| $R_c$ (Ω) | 3558 | 1104 |

Figure 43 shows experimental S-T slopes of the mixed-phase material as a function of the calculated crystallinity *f* for the 50 nm and 200 nm thick films. The crystallinity fraction of the 200 nm thin film is higher than that of the 50 nm film. It was also observed in crystal volume fraction change with annealing time at 160 °C for different thicknesses [76]. We believe the difference came from the average grain size dependence on film thickness.

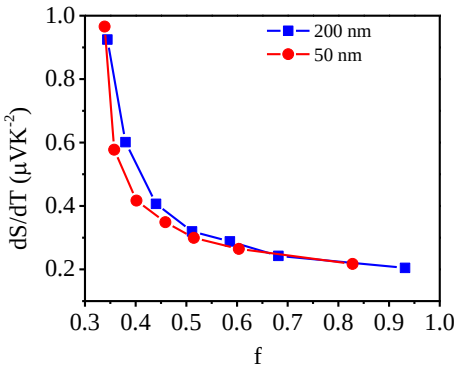


Figure 43. dS/dT vs. f in 200 nm GST thin films.

As mentioned before, dS/dT in degenerate conductors is related to the effective mass (~ $m^*/n^{2/3}$) and the sharp decrease in dS/dT observed here as a function of crystalline fraction indicates a corresponding variation in this ratio, $m^*/n^{2/3}$. A sharp decrease in hole effective mass is mentioned in the modeling work by Bogoslovskij and Tsendin as a possible mechanism of threshold switching with self-heating in chalcogenide glasses[77].

XRD measurements were also performed to correlate the transport parameters to the grain size in the mixed-phase material using the percolation model[72]–[75]. Both room temperature measurements on pre-annealed samples and in-situ measurements (at stabilized temperatures during anneal)[78] were performed. Figure 44 shows the evolution of XRD patterns with temperature for an as-fabricated amorphous 100 nm GST film as the chuck temperature was increased from room temperature to 585 °C in 100 °C steps and decreased back to room temperature. The peaks in the pattern of the amorphous sample are repeated in all patterns suggesting these originate from the silicon substrate and sample holder (Aluminum). The *fcc* phase of the sample at 200 °C and 300 °C is identified by the peaks at 25.5°, 29.4°, 42.4° and at 52.6° while the *hcp* phase exhibits different peaks at the angles 21.4°, 25.7°, 28.9°, 40.1°, 42.8°, 48.5°, and 52.9° corresponding to different planes, similar to what has been previously observed [79]–[83]. After cooling down the sample to room temperature, a new pattern is acquired and it shows a small shift to the right in all *hcp* peaks, which is due to the thermal expansion of the material at high temperatures [84]. From these results, the highest increase in the *hcp* planes spacing is 1.45% at 400 °C for the (004) direction. The average grain size at different temperatures was obtained from the XRD patterns using the Scherrer equation [85], [86] which relates the full-width-half-max (FWHM) $\beta$ from the peak intensity with the grain size (*gs)* [87]:

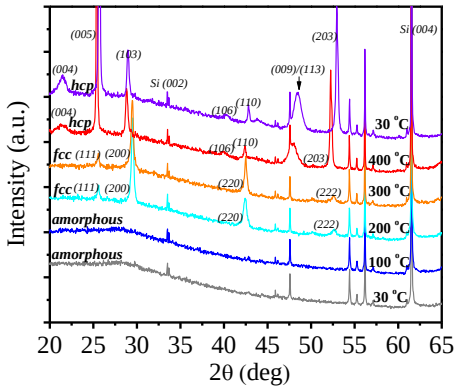


Figure 44. XRD patterns of 100 nm GST film annealed at different temperatures, then cooled down from 400 °C to get the pattern for *hcp*-GST at 30 °C.

$$gs = \frac{0.9\lambda}{\beta \cos\theta} \tag{55}$$

where $\lambda$ is the X-ray wavelength and $\theta$ is the diffraction angle. XRD measurements have been previously reported for *hcp*-GST annealed up to 330 °C and the average grain size was found to be 40.3 nm [88].

In order to correlate the XRD grain size results with those from our anneal temperature steps for the R(T) and S(T) measurements, the data for average grain size versus temperature were interpolated with a third order polynomial fit (Figure 45). Grain sizes calculated from impedance spectroscopy (IS) measurements by Huang *et al.*, assuming a brick model, [89] fall in the same range but show a significantly different trend with the anneal temperature (downward curvature).

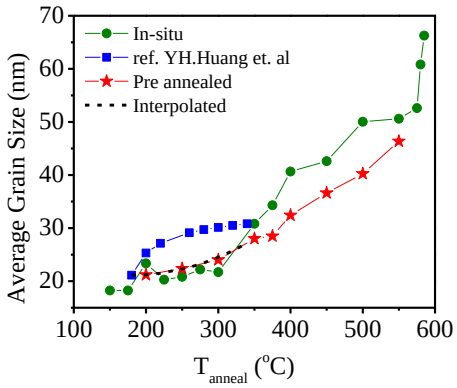


Figure 45. Average grain size calculated from XRD measurements on 200 nm thin GST film.

Since the model we have used for conductivity (equation 6) assumes spherical-like crystals in amorphous media, $f$ is proportional to $gs^3$ times the number of the grains in the sample, and it is interesting to look at the relation between $f$ and $gs^3$ obtained from XRD (Figure 46). There appear to be 3 different regions in the plot:

- In the first region (in yellow color), the crystallinity of the sample is increasing rapidly while the grains are not growing faster ($\Delta f/\Delta gs = 0.172$ nm$^{-1}$), it can be explained that nucleation of the material is still high and the number of grains is increasing.

- In the second region (light blue color), the $f$ is changing linearly with gs$^3$ with lower rate compare to previous region ($\Delta f/\Delta gs=0.0507$ nm$^{-1}$). Here the number of the crystals is constant and the change in the crystallinity is mainly related to the growth of the crystals.

- In the third region (magenta color), the critical size of the crystals is reached and the crystallinity is increasing rapidly with a small increase in the grain size. As a result, the main change in the volume of the crystal is the crystallization of the remaining gaps between the crystals.

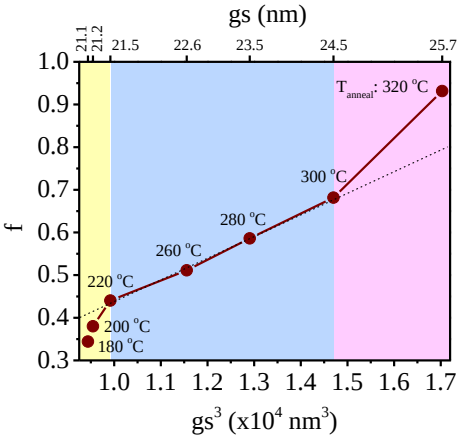


Figure 46. Crystallinity of the 200 nm GST thin film as a function of the cubic grain size gs$^3$.

## Thermal conductivity calculation

Seebeck coefficient is related to the thermal conductivity (k) through the PSM for composites[90]:

$$(1-f)\frac{\frac{k_a}{S_a}-\frac{k}{S}}{\frac{k_a}{S_a}+2\frac{k}{S}}+f\frac{\frac{k_c}{S_c}-\frac{k}{S}}{\frac{k_c}{S_c}+2\frac{k}{S}}=0 \qquad (56)$$

where $k_a$ and $k_c$ are the amorphous and *fcc* thermal conductivities and $S_a$ and $S_c$ are the amorphous and *fcc* Seebeck coefficients respectively, and $f$ is the crystalline fraction previously calculated using the percolation conductivity model. Solving the equation 4 with the condition $k_a \leq k \leq k_c$ leads to:

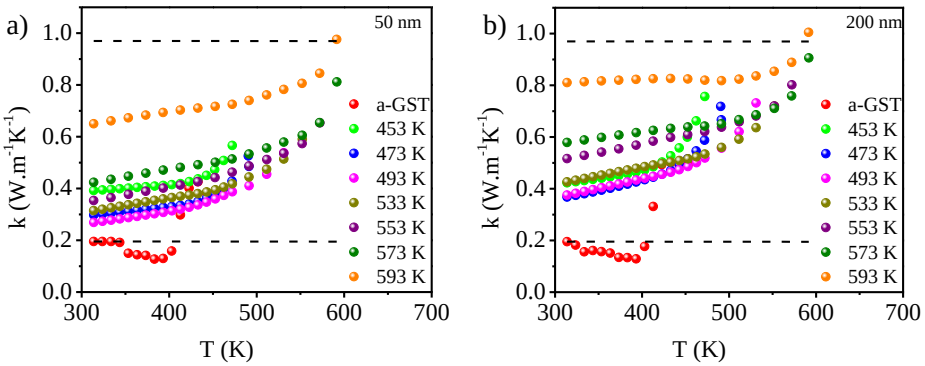


Figure 47. Calculated thermal conductivity for a) 50 nm and b) 200 nm films.

$$k = \frac{1}{4}S\left(\frac{ka}{Sa}(2-3f) - \frac{kc}{Sc}(1-3f) + \sqrt{\left(\frac{ka}{Sa}(2-3f) - \frac{kc}{Sc}(1-3f)\right)^2 + 8\frac{ka}{Sa}\frac{kc}{Sc}}\right) \quad (57)$$

One can note that for f=0, S=$S_a$, therefore k=$k_a$, and for f=1,S=$S_c$, and k=$k_c$.
Using the crystallinity *f* calculated before, and $k_a$ and $k_c$ reported in reference[91], calculated k-T characteristics for each crystallinity phase of 50 nm and 200 nm thin films is represented in Figure 47.

$k_a$-T characteristic (dash lines in Figure 47) used in the calculations is taken as the linear extrapolation of the first data points measured in the amorphous state of the material and $k_c$-T characteristic is a linear function of temperature that includes the thermal conductivity of the material at the second transition temperature calculated from the cooling cycle of the film in hcp phase. This approximation is justified by similar negative slope of *k*-T with the cooling of the material from 180 °C reported in the same reference.[91]

## Publications related to this work

### Journal Articles

L. Adnane, N. Williams, H. Silva, and A. Gokirmak. "High temperature setup for measurements of Seebeck coefficient and electrical resistivity of thin films using inductive heating." Review of Scientific Instruments 86, no. 10 (2015): 105119.

L. Adnane, H. Silva, and A. Gokirmak. "High temperature Hall measurement setup for thin film characterization" Review of Scientific Instruments 87, no. 7 (2016): 075117.

L. Adnane, F. Dirisaglik, A. Cywar, K, Cil, Y. Zhu, C. Lam, A. F. M. Anwar, A. Gokirmak, H. Silva. "High Temperature Electrical Resistivity and Seebeck Coefficient of Ge2Sb2Te5 Thin Films" Journal of Applied Physics 2017 (*Accepted*)

### Conference Presentations

Lhacene Adnane, Faruk Dirisaglik, Adam Cywar, Kadir Cil, Chung Lam, Helena Silva, Ali Gokirmak. "Seebeck Coefficient, Electrical Resistivity and Derived Thermal Conductivity of Ge2Sb2Te5 Thin Films" MRS Spring Meeting 2017, ED11.4.01

Lhacene Adnane, Ali Gokirmak, Helena Silva. "Simultaneous Seebeck Coefficient and Electrical Resistivity Characterization of Ge2Sb2Te5 Thin Films" CMOC UConn 2017

Lhacene Adnane, Faruk Dirisaglik, Kadir Cil, Adam Cywar, Yu Zhu, Chung Lam, Ali Gokirmak, Helena Silva. "Characterization of Seebeck Coefficient and Electrical Resistivity of Ge2Sb2Te5 Thin Films" ISDRS 2016. FP1-04

L. Adnane, F. Dirisaglik , K. Cil, Ali Gokirmak, H. Silva "Van der Pauw Hall Mobility Measurement Setup for Thin Film Characterization at High Temperatures " CMOC UConn 2015

L. Adnane, A. Gokirmak, H. Silva “Simultaneous Seebeck Coefficient and Electrical Resistivity Characterization of Ge2Sb2Te5 Thin Films" MRS Spring Meeting 2014, HH6.01

L. Adnane, F. Dirisaglik , A. Gokirmak, H. Silva " High Temperature Van Der Pauw Hall Measurements" MRS fall meeting 2013, BB11.05

L. Adnane, Y. Zhu, C. Lam, A. Gokirmak, H. Silva "Electrical Resistivity and Seebeck coefficient of Thin Film Ge2Sb2Te5 Up to 600 °C" MRS fall meeting 2012, B6.11

L. Adnane, A. Gokirmak, H. Silva "Seebeck Coefficient and Electrical Resistivity Measurement on Semiconducting Thin Films at High Temperature" CMOC UConn 2012

L. Adnane, F. Dirisaglik , M. Akbulut, Y. Zhu , C. Lam , A. Gokirmak , H. Silva "High Temperature Seebeck Coefficient and Electrical Resistivity of Ge2Sb2Te5 Thin Films" APS March Meeting 2011, Q28.00006

L. Adnane, N. Williams, A. Gokirmak, H. Silva "High temperature Seebeck coefficient and resistivity measurement setup" MRS fall meeting 2011, O8.12

## 7. Microplasma formation in ZnO nanoforest

### Motivation

The interest in environmentally friendly semiconductors, biocompatible, functional nanostructures, nanoscale electronic devices and large area electronics has led to significant research efforts in metal-oxide semiconductors such as ZnO. ZnO is a common, low-cost, antibacterial material that forms various nanostructures depending on the process conditions[92], [93]. It is an intrinsically n-type material with a large direct bandgap of ~3.4 eV. ZnO nanostructures can be grown using simple and inexpensive solution based synthesis techniques with various morphologies only by changing the process conditions. ZnO sublimates (i.e. evaporates directly from its solid form without experiencing a molten state) congruently at atmospheric pressure. The sublimation temperature of ZnO is ~380 °C for the Zn surface and ~600 °C for O surface. ZnO decomposes into zinc vapor and oxygen at ~1975 °C[92]–[96]

$$ZnO(s) \rightarrow Zn(g) + \frac{1}{2}O_2(g) \tag{58}$$

Techniques to produce ZnO microplasmas can lead to various applications in the synthesis and nanomaterials processing field. Due to the small probe separation, microplasmas can be produced at atmospheric pressure with small breakdown voltages and can also maintain the non-equilibrium state with low gas temperatures (in transient cold plasmas) when short duration pulse voltages are applied[97]. Such atmospheric pressure cold plasmas have a wide range of biomedical applications[98]. Cold ZnO atmospheric pressure microplasmas can be used for sterilization[99], medical[100], and dental[101] procedures. On the other hand, hot ZnO microplasmas can be used for materials processing, lighting and

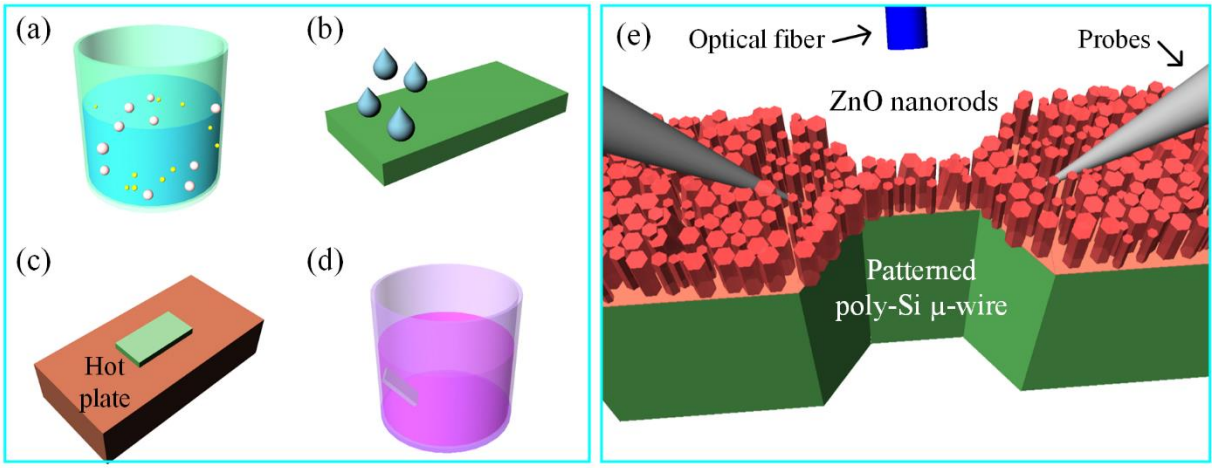


Figure 48. Schematics of (a-d) the growth process for the ZnO nanoforests and (e) the electrical probe and optical fiber arrangement[92], [93].

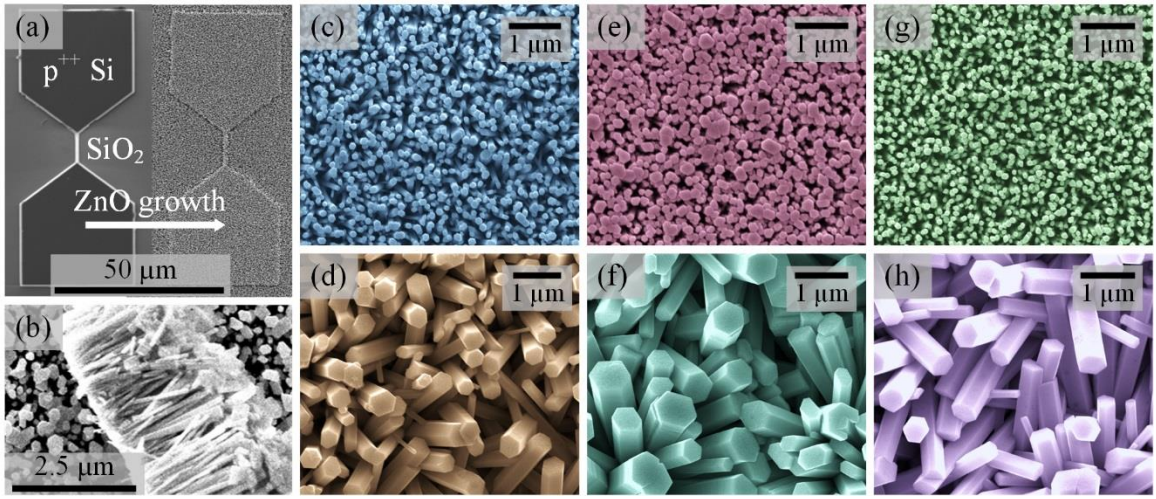


Figure 49. Scanning electron microscope (SEM) images of the ZnO NRs grown on (a) ~100 nm thick, highly doped, patterned, $p^{++}$-type, silicon microstructures (before and after ZnO nanorod growth) and (b) cross-section SEM image of the ZnO NRs. False colored SEM images of (c) ~100 nm and (d) ~400 nm ZnO NRs on FTO glass, (e) ~150 nm and (f) ~600 nm ZnO NRs on $p^{++}$-poly-Si, (g) ~100 nm and (h) ~500 nm ZnO NRs on $p^{--}$-sc-Si[92], [93].

display device technologies [102]. Generation of ZnO plasmas has typically been done using pulsed laser ablation[103]–[105] to obtain high quality ZnO thin films and nanomaterials[92].

We have grown ZnO nanoforest formed of nanorods (NRs) of various sizes and on different substrates. Applying high electric fields (~3–7 V/μm) to the NRs using tungsten probes have resulted in a bright blue and white light emission. We have performed electrical characterization at different ambient pressures and analyzed the resulting optical emission spectra and videos to determine the mechanisms giving rise to light emission.[92], [93], [106]–[109].

### ZnO nanoforest synthesis

We have used Chemical bath deposition (CBD)[110], a low-cost solution-based technique to grow the ZnO NRs on the following substrates:

1. Previously fabricated highly doped p-type poly-crystalline silicon microstructures (μ-wire) (Figure 48a and 16b).
2. Commercial fluorine doped tin oxide (FTO) glass (Figure 48c and 16d).

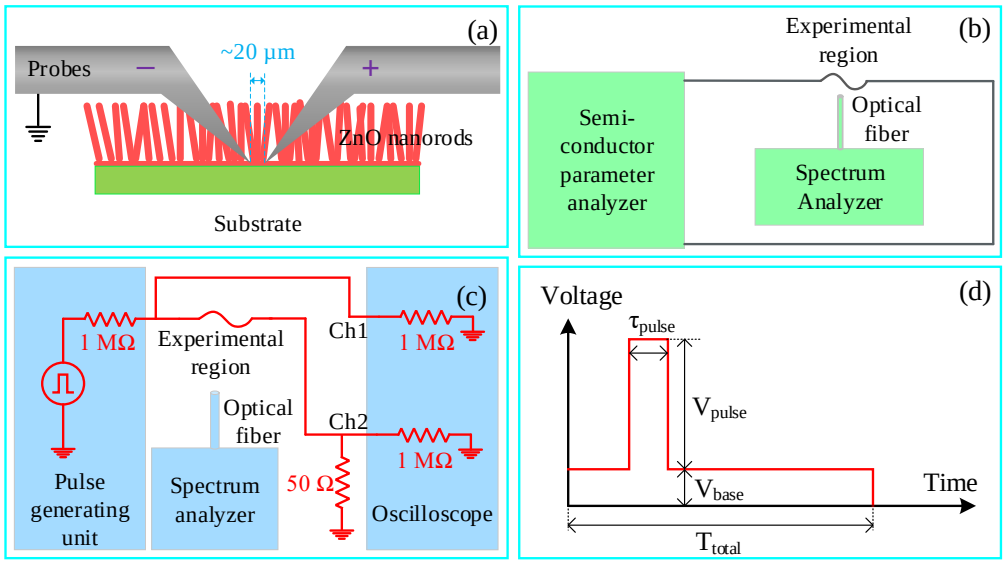


Figure 50. (a) Schematics of the probe arrangement, (b,c) electrical measurement setup for DC and pulse analysis, (d) Schematic of applied single pulse: pulse voltage ($V_{pulse}$) with duration $\tau_{pulse}$ and baseline voltage ($V_{base}$) with total duration $T_{total}$[92], [93].

3. Highly doped p-type poly-crystalline silicon ($p^{++}$-poly-Si) (Figure 48e and 16f).
4. Lightly doped p-type single crystal silicon ($p^{--}$-sc-Si) (Figure 48g and 16h).

The samples were first precleaned with deionized water, soap solution, and sonication in ethanol and then dried with nitrogen. Next, the clean and dried samples were spin-coated (sample 1) or drop-coated (samples 2-4) with a seed solution prepared by dissolving 0.0457 mg of zinc acetate dihydrate in 50 mL of ethanol (Figure 49a and 17b). The samples with seed layer were then baked at 350 °C for 30 min (Figure 49c). Meanwhile, a water-based precursor solution was made with 25 emmM of zinc nitrate hexahydrate, 25 mM of hexamethylenetetramine, and 6 mM of poly(ethyleneimine). In the final step, the baked samples were submersed in the precursor solution and kept at 90 °C for 24 h (Figure 49d). The process yields 2–2.5 µm long ZnO NRs homogeneously grown along the c-direction of the wurtzite structure with ~150 nm diameter on top of a very thin layer of ZnO film (~2–3 nm). Using a different water ratio for the seed solution, larger NRs with average diameter of ~500 nm was also obtained with the samples 2-4[92], [93].

### Electrical and optical experimental set-up

The grown samples were electrically characterized in open air in an Alessi probe station at atmospheric pressure and in vacuum inside a Janis cryogenic probe station at 2.5 mTorr (medium vacuum). The probe stations were equipped with high-magnification optics (5X-100X) and high-resolution micromanipulators. The electrical excitations were applied with tungsten probe tips of 2.4 µm tip radius and 45° angle (Cascade Microtech, PTT-24/4-25) with an average probe separation of ~10-20 µm achieved with micromanipulators. The probes were forced to slightly slide through the ZnO nanoforest to ensure good electrical contact (Figure 49e and Figure 50a) [92], [93]. We carried out three types of electrical characterization:

1. DC voltage sweeps between 0–80 V using HP 4145B semiconductor parameter analyzer (Figure 50b)[93],

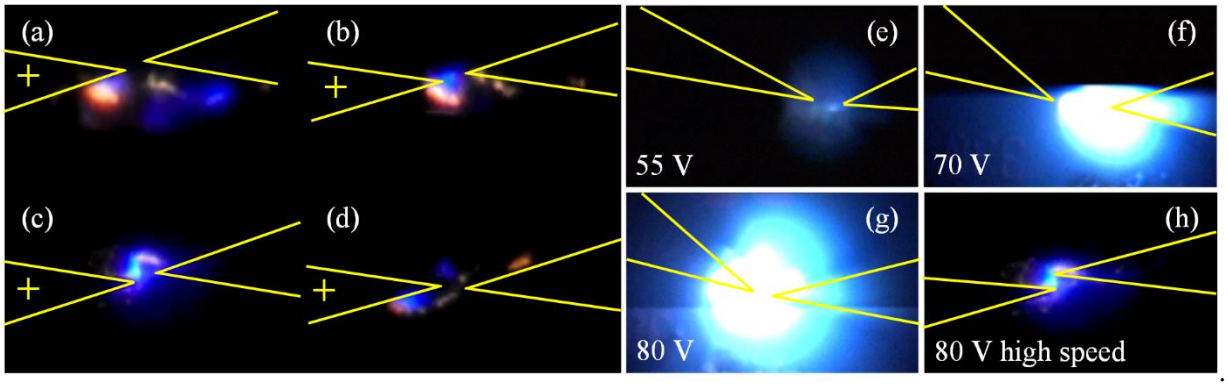


Figure 51. Frames extracted from high-speed and high-resolution videos showing light emission from the ZnO nanorods contacted by tungsten probes with approximate separation of 10–15 μm (a-d) during DC tests and (e-h) during AC excitation of 10–10000 Hz with the indicated peak-to-peak voltage levels. The probe locations and applied voltage polarity are as indicated in yellow[93].

2. AC sinusoidal voltages with peak-to-peak amplitudes up to 80 V and 1–10 kHz frequency with Tektronix AFG 3102 arbitrary/ function generator[93], and
3. microsecond single pulses with amplitudes up to 50 V using Agilent 8114A pulse generator (Figure 50c and d)[92].

For imaging of the test area and video recording of the light emission, either a high-sensitivity 1080p HD camcorder with a frame rate of 60 fps (Sony, HDR-CX160) or a high-speed camera with a maximum of 1200 fps (Casio, EX-F1) was connected to the microscope head. A wideband (200–1100 nm) optical spectrometer with 1 nm resolution (Ocean Optics, HR2000+) was incorporated with the system to understand the physical mechanism responsible for the light emission through spectral analysis. An optical fiber was coupled to the spectrum analyzer and the other end of the fiber was attached to a probe arm which was aligned to the test area using a micromanipulator.

Another micromanipulator was attached to a high-speed PIN diode with built-in amplifier which was positioned to face the test area to detect the emitted light intensity with better time resolution. The distance from the PIN diode to the sample was adjusted to achieve adequate signal-to-noise ratio without saturating the diode during the experiments. The voltage output of the built-in amplifier was significantly larger than any noise or perturbations coupled into the signal lines caused by the fast pulses. Hence, this approach was preferred over a simple PIN diode for detection. The applied voltage, PIN diode output voltage, and resulting current were measured simultaneously using two synchronized two-channel oscilloscopes (Tektronix, TDS 2002B). The electrical resistivities of the bare polysilicon substrate and the sample with ZnO NRs on polysilicon were measured using a four-point probe method[92], [93].

The coaxial cable lengths were matched to minimize the difference in phase delay. The signal generator output and the oscilloscopes inputs were terminated to 50 Ω resistors to eliminate reflections and oscillations. To exclude the ambient light, the entire probe station was covered with a black enclosure, light sources inside the probe setup and the ones at the room were turned off during measurements. The remainder leakage light was stored as the reference dark spectrum and was deducted with the spectrometer tool. The electrical measurements, instrument control, and data acquisition were performed with LabVIEW codes and the optical spectrum recordings were all controlled through computer[92], [93].

### Results from electrical and optical experiments

The electrical excitation resulted in bright blue and white light in all measurements and orange–pink regions in some cases. Higher current levels and stronger emissions were observed as the voltage

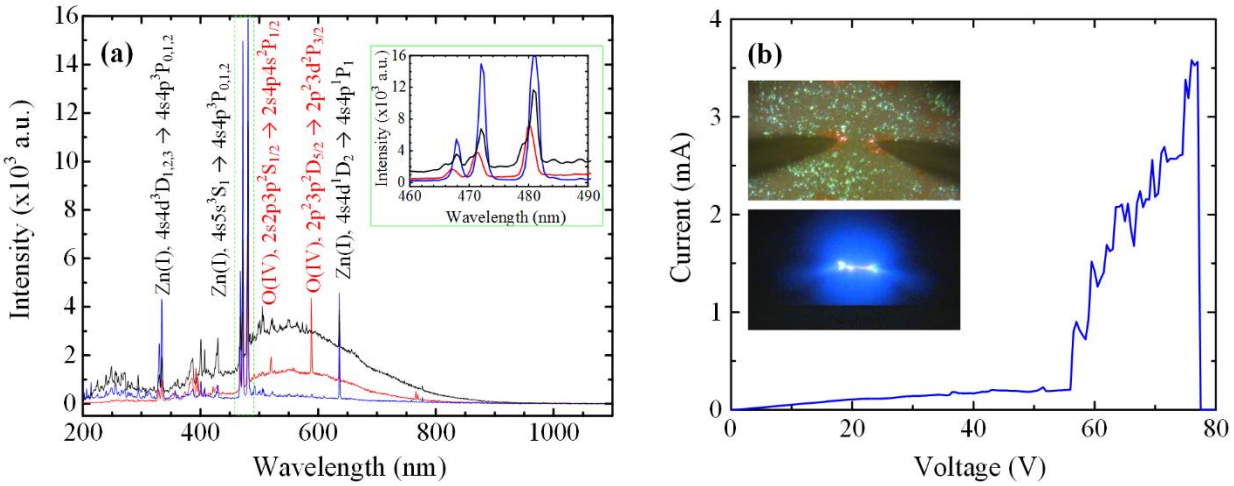


Figure 52. (a) Optical emission spectra obtained from DC voltage sweeping of 0–80 V (blue), AC excitation with an amplitude of 40 V at 1 kHz (red), and single pulse voltage with an amplitude of 35 V and a duration of 10 µs (black). The corresponding atomic electron transitions in the excited species are indicated adjacent to the spectral lines. The inset shows the characteristic peaks (triplet) for neutral Zn atoms. (b) Example of a DC, I–V characteristic from 0–80 V in steps of 1 V through the ZnO nanorods. The entire DC sweep was carried out in ≈10–15 s. The insets show the optical image of the probe arrangement before the test (top) and a frame from the high-resolution video of the light emission (bottom)[93].

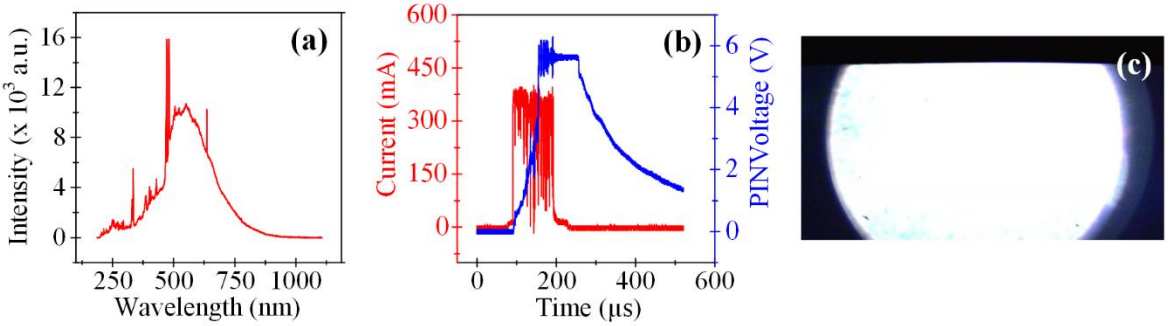


Figure 53. (a) Spectrum of the light emission resulting from application of a single pulse with amplitude of 45 V and duration of 100 µs. The spectral line around 480 nm was clipped due to the saturation of the spectrum analyzer. The white light (broad spectrum) content was very strong for this pulse. (b) Current and PIN output voltage versus time measured by an oscilloscope. The photodiode used for this trial was very sensitive but not fast enough to capture the details, showing slow rise and fall times and saturation. The delay was primarily due to the response time of the built-in amplifier in the PIN diode package. The fluctuations in the current indicate the recurrent formation and termination of conductive paths between the contacts. (c) A frame extracted from the corresponding light emission video[93].

levels were increased. Multiple flashes with changing percolation paths were monitored during longer excitations as the materials experience changes in thermal and electrical properties over time due to the high electrical stress (Figure 51). The measured spectra (with DC, AC and pulse analyses) consistently showed three, high intensity, fine spectral lines at approximately 481, 472 and 467 nm. This triplet (in blue wavelength range in inset of Figure 52a corresponds to atomic electron transitions (AETs) in neutral zinc (Zn I) atoms. The localized orange–pink glow observed in some cases (at ~635 nm) can also be ascribed to another AET of neutral zinc (Figure 52a). Hence, the existence of these fine lines indicates generation of a plasma by the dielectric breakdown of air between the ZnO nanorods and of the breakdown of the ZnO structures themselves, leading to sublimation and plasma formation in the ZnO nanoforest[93].

The application of higher amplitude and longer duration voltage pulses resulted in a greater overall intensity of the emitted light (Figure 52 and Figure 53). The broad spectrum (white light) emission (Figure 52 and Figure 53) can be ascribed to the free–free electron transitions in the plasma, the electronic excitations within solid ZnO and/or energy loss through multiple transitions with a very broad spectrum of trap levels [111]. Blackbody radiation may also contribute to the broad spectrum, white light emission but the spectral distribution is distinctly different than what is expected from blackbody radiation alone. The lack of broad spectrum emission in some of the DC experiments indicates a distinct difference in plasma conditions (Figure 52). The intensity of the emitted light was often strong enough to saturate the spectrum analyzer, PIN diode and the camera, even for a single μs-duration pulse (Figure 53a). The pulse measurements showed a non-steady and high current level (Figure 53b) [93].

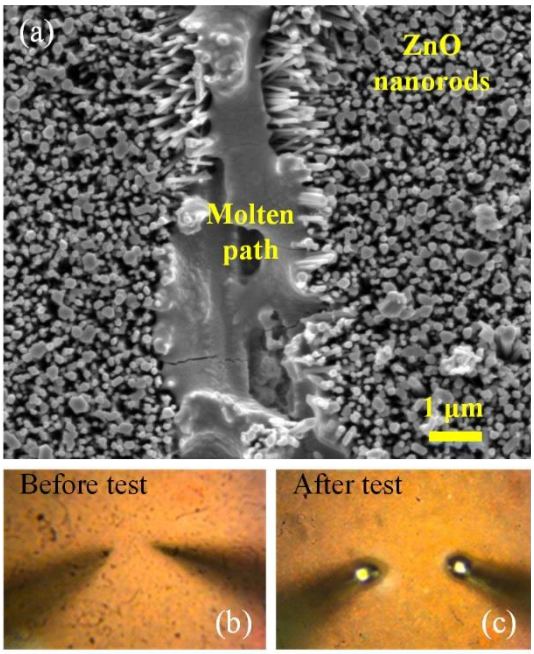


Figure 54. (a) Scanning electron microscope image of the molten path due to the current flow between the contacts after a DC test showing evidence of melting and recrystallization of the material under electrical stress. (b,c) Optical microscope images showing two tungsten probes placed on a continuous ZnO nanoforest before (left) and after (right) a DC measurement test. The melting of the micrometer-sized probe tips during the electrical test suggests local temperatures above the melting point of tungsten (3422 °C) [93].

*Physical origin of plasma formation*

Since the ZnO nanoforest material has relatively weak mechanical properties and adhesion to the substrate, probing with tungsten tips causes some shifting of this material and hence the probes are likely to touch both ZnO and the polysilicon substrate. The room-temperature electrical resistivity of ZnO nanoforest on highly doped polysilicon is ~6.8 Ω·cm and that of highly doped polysilicon substrate itself is ~0.02 Ω·cm. Therefore, the current is expected to mostly flow through the polysilicon substrate, at least in the beginning when the temperature is low. As the temperature increases, due to Joule heating, the current paths will change depending on the temperature dependence of the resistivity of these two materials[93].

Due to the large difference in resistivity, however, it is likely that the current flows mostly through the polysilicon substrate until the electrical breakdown of air or the ZnO nanorods occurs under the high fields and lower resistivity paths open through the ZnO nanoforest[93].

Because of the geometrical nonuniformity of the ZnO nanoforest, the electrical resistance and electric field distribution between two probes are also nonuniform. Therefore, some segments along the current flow path are likely to undergo dielectric breakdown and joule heating earlier than others. The joule heating in turn results in sublimation of ZnO into Zn vapor and $O_2$ gas and melting of the polysilicon substrate. Thus, different regions between the two probes are expected to experience these thermal changes in a sequential fashion[93].

The SEM images taken in our experiments after DC electrical analysis (Figure 54a) indicate melting of the materials between the contacts, and an optical image of the tungsten probes after some of the measurements (Figure 54 b and c) indicates melting of the probe tips. Hence, in some cases, the local temperature exceeds the melting point of tungsten (3422 °C), which is significantly above the sublimation

temperature of ZnO[93] (~380 °C for the Zn surface, ~600 °C for the O surface, and ~1975 °C for the decomposition into zinc vapor and oxygen) [94], [95].

Figure 55a shows DC voltage sweep measurements performed in vacuum and at atmospheric pressure with a probe separation of ~10 μm on the ZnO nanorods grown on two adjacent polysilicon microstructures of very similar dimensions (length of 2.5 μm and width of 2.1 and 2.15 μm). The resulting I–V characteristics showed breakdown voltages at around 35 and 49 V at vacuum and atmospheric pressure, respectively. At lower pressure, lower temperature and hence, smaller applied electrical energy lead to sufficient vapor pressure to initiate the sublimation process[93], [112].

The resulting light emission consisted of multiple flashes for the DC measurements both in vacuum and at atmospheric pressure. However, the light flashes in the atmospheric pressure measurements were more intense, whiter, and occurred over a broader area as compared to those in vacuum (Figure 55 b–g). The observation of light emission in vacuum implies that breakdown in ZnO, sublimation, and subsequent impact ionization are sufficient for the plasma formation process in the ZnO nanoforest, and hence, air breakdown is not a key requirement for initiation of the plasma formation process[93].

Typically, 3.4 eV emission (UV light) is expected from ZnO if conduction band to valance band recombination is the dominant mechanism. White light can also be emitted from the ZnO structures as the excited carriers trickle down from the conduction band to valance band through multiple defect levels or because of the optical excitation of materials by the ultraviolet source[113]. Blue light has been previously observed from ZnO-based homojunction LEDs, where it is attributed to donor–acceptor pair recombination in the p-type ZnO layer[114] and also from n-ZnO/p-GaN heterojunction LEDs[115]. The superposition of electroluminescence and Fabry–Pérot oscillations has also been suggested as the possible mechanism for blue–white emission from ZnO-based homojunction LEDs[93], [116].

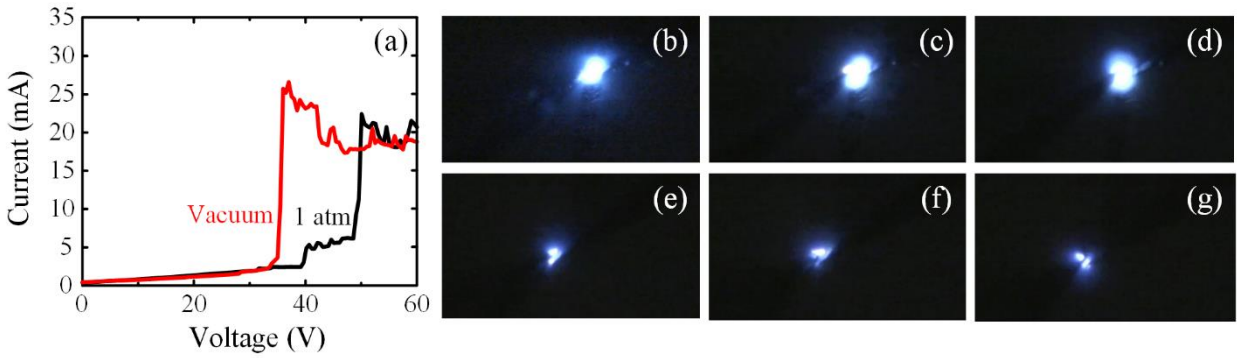


Figure 55. (a) I–V characteristics for two DC voltage sweep measurements from 0–60 V performed in vacuum (red) and at atmospheric pressure (black). These measurements were performed on ZnO nanorods grown on two different polysilicon microstructures of very similar dimensions. (b–g) Video frames extracted from a high-resolution camera recording for the corresponding light emission for the DC measurements at atmospheric pressure (b–d) and in vacuum (e–g)[93].

### *Hot and cold microplasmas*

Gradual increase of pulse amplitude ($V_{pulse}$) at a constant pulse duration ($\tau_{pulse}$) gave rise to increased light intensity. With a $\tau_{pulse}$ of 100 µs, the $V_{pulse}$ was varied from 10 V to 40 V in 10 V steps keeping a base voltage ($V_{base}$) of 10 V with the total duration ($T_{total}$) of 1 ms for the ZnO NRs with average diameter of ~100 nm on FTO substrate (Figure 56). The smaller amplitudes (10 and 20 V) resulted in blue light with low intensity (Figure 56a and 24b) while the higher ones (30 and 40 V) caused white light with blue glows with an overall increase in intensity (Figure 56c and 24d). All the resultant spectra showed sharp spectral lines at 480, 472 and 467 nm (for the blue light) corresponding to the AET in neutral Zn atoms[117]. The increase in $V_{pulse}$ resulted in additional spectral lines associated with the AETs in several Zn and O ionic species indicating the increase in the degree of ionization of the plasma. The higher values of $V_{pulse}$ also initiated a broad continuum in the emission spectrum between ~200 and 900 nm corresponding to the white light observed near the positive probe (Figure 56c and 24d). This broad continuum can be a result of several processes, such as thermal bremsstrahlung emission (due to free-free electron transitions), recombination from different trap sites[111], and black body radiation[118]. Melting of the positive probe was also noticed

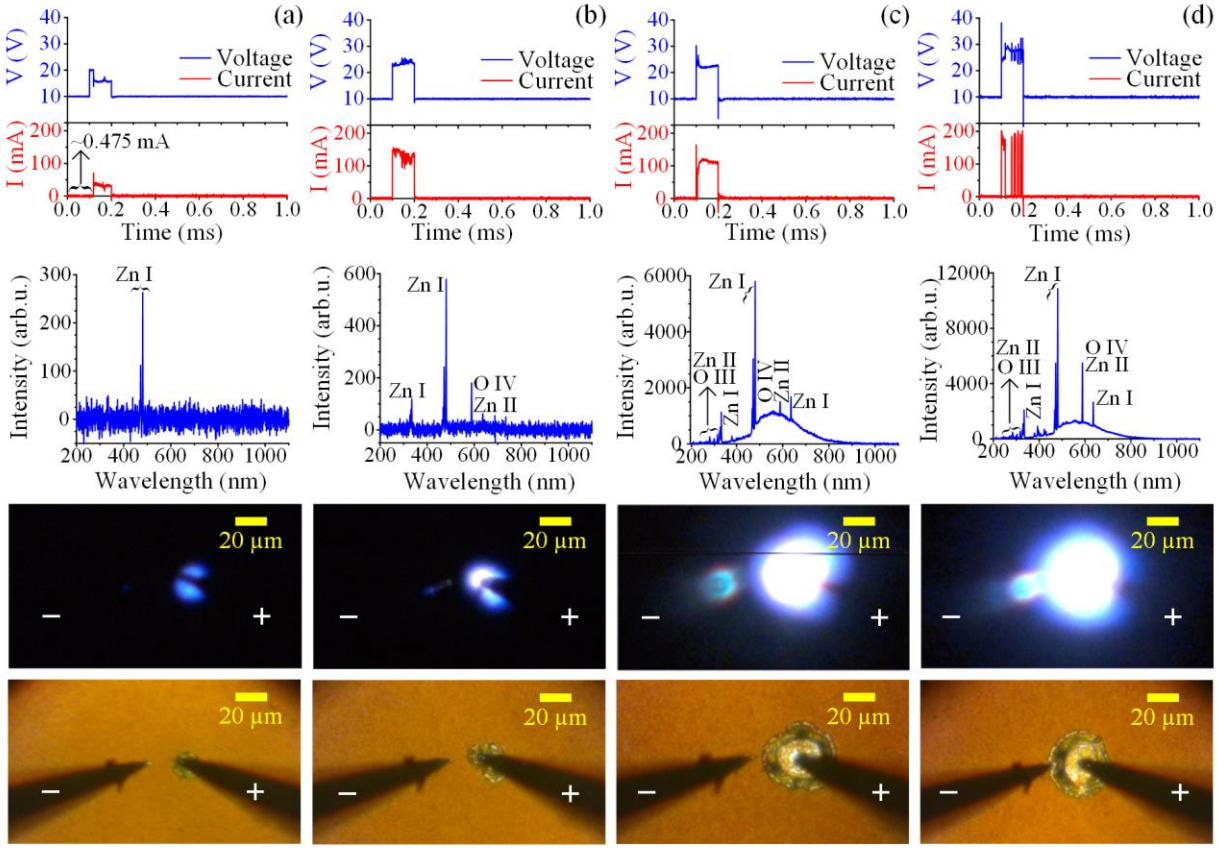


Figure 56. Pulse experiments through ZnO NRs (average diameter of ~100 nm) on FTO glass substrate with $\tau_{pulse}$ = 100 µs, $T_{total}$ = 1 ms, $V_{base}$ = 10 V. Vpulse was increased from 10 V to 40 V in 10 V steps (10 V in a, 20 V in b, 30 V in c, 40 V in d). The probe separation was kept ~20 µm and the spectrometer integration time was maintained at 100 ms for all measurements. Applied voltages and resulting currents versus time (1st row). Optical emission spectra (2nd row). Video frames of the light emission (3rd row). Optical micrographs of the test areas after the electrical stress (4th row) [92].

in the high amplitude cases (Figure 56c and 24d), which indicates a very high gas temperature (greater than the melting point of tungsten at 3422 °C)[92].

The overall high light intensity, high degree of ionization, introduction of broad spectrum and probe melting in the high amplitude cases (Figure 56 c and d) indicate these are hot plasmas (with high gas temperature). On the other hand, the low degree of ionization, absence of the white broad continuum and negligible probe melting in the low amplitude cases (Figure 56a and 24b) suggest cold plasmas. For the cold ZnO plasmas, the gas temperature may be as low as the sublimation temperature of ZnO. Further experiments are required to probe the gas temperatures of these hot and cold plasmas[92].

The pulse duration also affected the characteristics of the generated plasmas. Single pulses of three different durations ($\tau_{pulse}$ = 1, 10 and 100 μs) were applied on the same sample of ZnO nano-forests on FTO glass substrate (Figure 57). For each case, the minimum voltage required to initiate the plasma ($V_{BDmin}$) was monitored. It was observed that shorter pulses required higher pulse amplitudes for plasma generation. For instance, while a 100 μs, 10 V pulse led to plasma generation (Figure 57a), a 10 μs pulse required an amplitude of 24 V (Figure 57b) and a 1 μs pulse required 45 V (Figure 57c). For each case, $V_{BDmin}$ resulted in low intensity blue light (or cold ZnO plasma) and any applied voltage below $V_{BDmin}$ did not lead to any observable light emission[92].

Cold ZnO plasmas or blue emissions were therefore generated with $\tau_{pulse}$ of 1-100 μs and $V_{pulse}$ of 10-45 V for the NRs with diameter of ~100 nm on FTO glass substrate. Longer pulse durations did not lead to blue emissions – the smallest voltage of $V_{pulse}$ = 0 V (with $V_{base}$ = 10 V) resulted directly in the high intensity white light with the broad spectrum and probe melting – whereas shorter pulse durations did not lead to plasma generation until the minimum required amplitudes ($V_{BDmin}$) applied (Table 4)[92].

### *Substrate effect on plasma generation*

The pulse measurements were also conducted with the samples grown on $p^{++}$-poly-Si and $p^{--}$-sc-Si substrates. For ZnO NRs on silicon, plasma generation required pulses of at least 100 ms duration

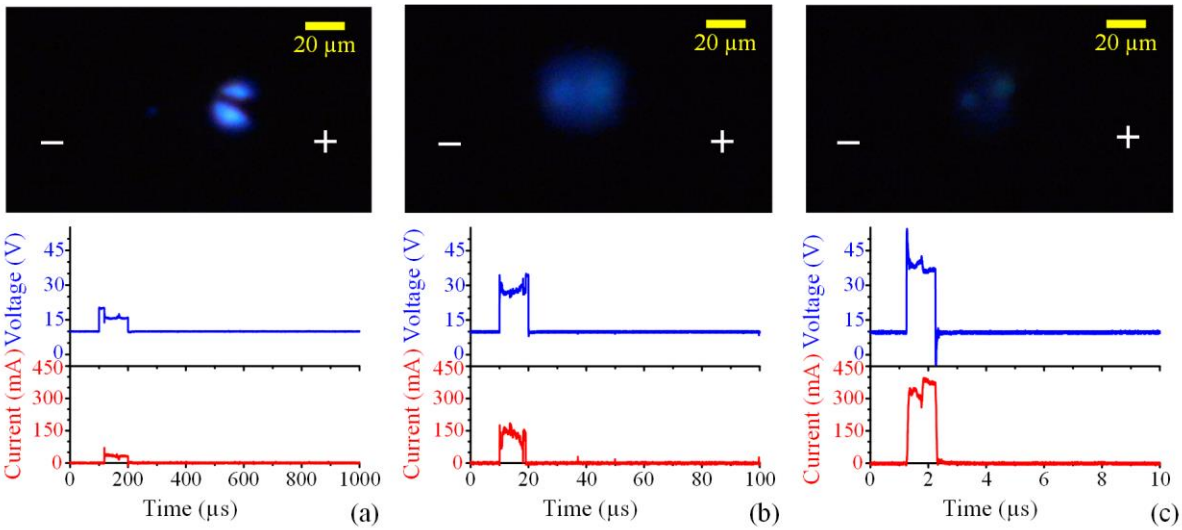


Figure 57. Cold ZnO plasmas with characteristic blue light emission. The pulse measurements were carried out through ZnO NRs (with average diameter of ~100 nm) on FTO glass substrate with $V_{base}$ = 10 V and (a) $V_{pulse}$ = 10 V, $\tau_{pulse}$ = 100 μs, $T_{total}$ = 1 ms; (b) $V_{pulse}$ = 24 V, $\tau_{pulse}$ = 10 μs, $T_{total}$ = 100 μs; (c) $V_{pulse}$ = 45 V, $\tau_{pulse}$ = 1 μs, $T_{total}$ = 10 μs. The spectral peaks were found at 480 and 472 nm (in (a)) and 480 nm only with lower intensity (in (b) and (c)). For lower pulse durations, higher voltage amplitudes were required to accomplish plasma breakdown. Images of the emitted light extracted from the videos recorded with 60 fps frame rate (1st row). Current and voltage versus time graphs (2nd row) [92].

Table 4. Comparison of the minimum applied voltages required for triggering plasma generation ($V_{BDmin}$) for different $\tau_{pulse}$ on different substrates (with corresponding resistivity values of the bare substrates). ZnO NRs of larger size (~500 nm average diameter) were used for this analysis.

| Pulse duration ($\tau_{pulse}$) | Required $V_{BDmin} = V_{pulse} + V_{base}$ | | |
|---|---|---|---|
| | On FTO ($2.4X10^{-4}$ Ωcm) | On $p^{++}$-poly-Si ($2.3X10^{-2}$ Ωcm) | On $p^{-}$-sc-Si (20 Ωcm) |
| 100 ms | N/A‡ | 25 V + 10 V | 50 V + 10 V |
| 100 µs | 9 V + 10 V | N/A* | N/A* |
| 10 µs | 19 V + 10 V | N/A* | N/A* |

‡The sample on FTO substrate did not lead to blue emission for any $\tau_{pulse}$ > 100 µs even with a smallest applied voltage of $V_{pulse}$ = 0 V and $V_{base}$ = 10 V.
*The samples on silicon substrates did not lead to plasma generation for $\tau_{pulse}$ < 100 ms[92].

whereas for those on FTO glass pulses as short as 1 µs were sufficient (Table 4). A comparison of the required $V_{BDmin}$ for the samples on these three substrates was carried out with the ZnO NRs of larger diameters (~500 nm) (Table 4). Such comparison could not be made with the smaller size NRs (of ~100 nm) as the samples of smaller NRs on silicon substrates could barely emit light (with up to 100 ms, 50 V pulses) and appear to require even higher energies for plasma generation. The electrical conductivity of the substrates, which determines the conduction paths through the nanoforests, appears to play a critical role on the plasma generation. The highest conductivity substrate, FTO, results in the easiest plasma formation (Table 4). This was also observed under DC sweeps from 0 to 80 V which show overall smallest resistance and breakdown voltage for the ZnO nanoforests on FTO glass (figure 7 in Ref [92]). In addition to the electrical conductivity, the chemical composition and the surface properties of different substrates may also play a role in the differences observed in the microplasma formation.

### *Nano-material synthesis*

The generation of ZnO plasma by high electrical stress through the ZnO nanoforests resulted in sputtering of nanomaterials with large surface area on the neighboring regions (Figure 58). Different pulse amplitudes, durations, and different substrates gave rise to sputtering of different shape and size nanostructures over the ZnO NRs. These resemble 'nano-sprinkles' on ZnO NRs on $p^{++}$-poly-Si (Figure 58a), 'nano-flowers' on ZnO NRs on FTO glass (Figure 58b), and 'nano-flowers' and 'nano-cauliflowers' on ZnO NRs on $p^{-}$-sc-Si (Figure 58 c-f). A single pulse of $\tau_{pulse}$ = 100 ms and $V_{pulse}$ = 50V through the ZnO NRs on $p^{++}$-poly-Si resulted in the 'nano-sprinkles' shown in Figure 58a. The 'nano-flowers' on ZnO NRs on FTO glass (Figure 58b) were produced by applying a single pulse of $\tau_{pulse}$ = 100 µs, $V_{pulse}$ = 40V, $V_{base}$ = 10 V, $T_{total}$ = 1 ms. The larger surface-area nanostructures shown in Figure 58 c-f were formed after the repeated application of multiple single pulses of $\tau_{pulse}$ = 100 ms, $V_{pulse}$ = 50V, $V_{base}$ = 10 V, $T_{total}$ = 1 s through the ZnO NRs on $p^{-}$-sc-Si. Energy dispersive x-ray spectroscopy (EDX) was carried out on the sputtered area to obtain the elemental composition of the sputtered material. The results showed ~80-90% (percentage of weight) of ZnO in the sputtered material[92].

## Summary

The electrical experiments performed on ZnO nanorods grown on silicon and FTO glass substrates lead to high intensity, blue and white light emission. The abrupt increase in current at higher fields, sharp spectral peaks and very high local temperatures (observed as significant probe melting) indicate ZnO dielectric breakdown, sublimation, and plasma generation. The sharp spectral lines correspond to atomic electron transitions of excited Zn and O species in plasma. The comparison between the results obtained from vacuum and atmospheric pressure measurements also indicate a plasma process as the dominant mechanism for light emission. The intensity and characteristics of the microplasmas and emitted light were adjusted to a certain degree by the amplitude and duration of the applied voltage pulses. Both hot and cold microplasmas could be obtained with ZnO nanoforests on FTO glass. Very high white light intensity, high degree of ionization, a broad spectrum and probe melting indicate hot plasmas whereas lower intensity blue light, low degree of ionization, absence of a broad continuum and no evidence of probe melting suggest colder plasmas.

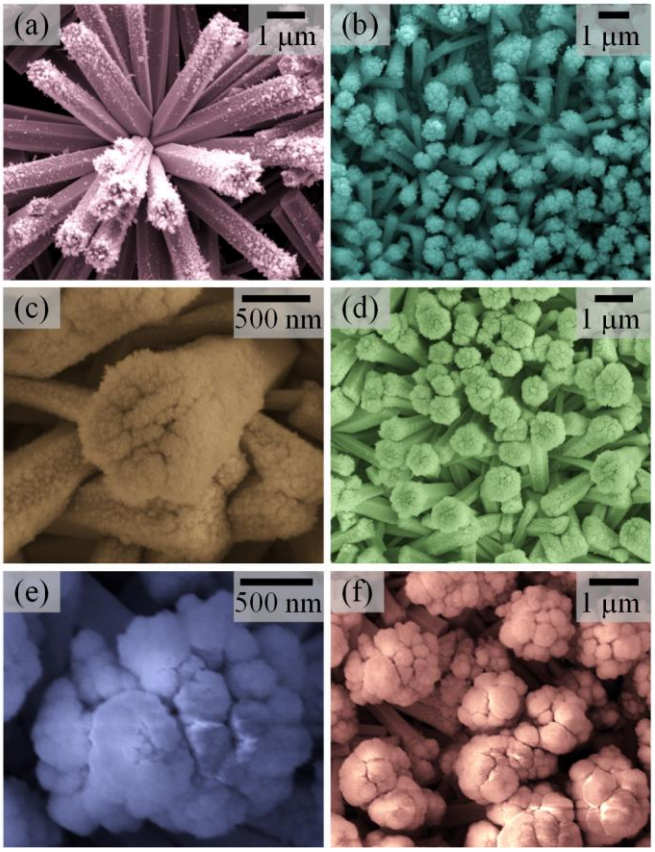


Figure 58. False colored scanning electron micrographs of ZnO nanostructures sputtered over the ZnO nanorods in the test areas during plasma generation: 'nano-sprinkles' on ZnO NRs on $p^{++}$-poly-Si (a), 'nano-flowers' on ZnO NRs on FTO glass (b), and 'nano-flowers' and 'nano-cauliflowers' on ZnO NRs on $p^{--}$-sc-Si (c-f)[92].

The confinement of the plasma within a micro-chamber to contain the evaporated material [119] together with integrated electrodes may lead to a sustainable plasma state that could be tailored for various applications. Cold ZnO microplasmas may find applications in numerous biomedical procedures whereas hot ZnO microplasmas may be useful for lighting and display device technologies as well as for nanomaterials synthesis or processing. The large surface area ZnO nanostructures sputtered near the microplasmas may also be promising to increase the efficiency of a variety of sensing or catalytic technologies including dye sensitized solar cells.

Even though many reports on light emission from ZnO refer to solid-state electroluminescence from homojunction or heterojunction structures, our results show that plasma formation can also take place with comparable electric fields and currents and can lead to blue and white light emission.

## Publications related to this work

### Journal articles

Nafisa Noor, Luca Lucera, Thomas Capuano, Venkata Manthina, Alexander G. Agrios, Helena Silva, and Ali Gokirmak. "Blue and white light emission from zinc oxide nanoforests." Beilstein journal of nanotechnology 6 (2015): 2463.

Nafisa Noor, Venkata Manthina, Kadir Cil, Lhacene Adnane, Alexander G. Agrios, Ali Gokirmak, and Helena Silva. "Atmospheric pressure microplasmas in ZnO nanoforests under high voltage stress." AIP Advances 5, no. 9 (2015): 097212.

### Conference presentations

Luca Lucera, Lhacene Adnane, Kadir Cil, Venkata Manthina, Alexander Agrios, Helena Silva, and Ali Gokirmak, "*Light emission from electrically stressed ZnO nanorods*", APS March Meeting 2012, Volume 57, Number 1, L28.0001, Boston, Massachusetts, USA, 2012.

Nafisa Noor, Thomas Capuano, Venkata Manthina, Helena Silva, Alexander G. Agrios, and Ali Gokirmak; '*Plasma in a ZnO Nano-forest: Electrical discharge, and blue and white light emission*'; 8th International Workshop on Zinc Oxide and Related Materials (IWZnO 2014), Niagara Falls, Ontario, Canada, September 2014.

Nafisa Noor, Venkata Manthina, Helena Silva, Alexander G. Agrios, and Ali Gokirmak; '*Blue and White Light Emission from ZnO Nanoforests*'; 2014 MRS Fall Meeting & Exhibit, Boston, Massachusetts, USA, December 2014.

Nafisa Noor, Venkata Manthina, Kadir Cil, Alexander G. Agrios, Helena Silva, and Ali Gokirmak; '*Blue and White Light Emission from ZnO Nanoforest Microplasmas*'; 24th Annual CMOC Symposium, Bridgeport, Connecticut, USA, April 2015.

## 8. Journal articles that resulted from this work

[21] L. Adnane, F. Dirisaglik, A. Cywar, K, Cil, Y. Zhu, C. Lam, A. F. M. Anwar, A. Gokirmak, H. Silva. "High Temperature Electrical Resistivity and Seebeck Coefficient of Ge2Sb2Te5 Thin Films" Journal of Applied Physics 2017 (*Accepted*)

[20] Z. Woods and A. Gokirmak, "Modeling of Phase Change Memory: Nucleation, Growth and Amorphization Dynamics during Set and Reset: Part I - Effective Media Approximation" *IEEE Trans. Electron Devices*, 2017 (Accepted).

[19] Z. Woods, J. Scoggin, A. Cywar, L. Adnane, and A. Gokirmak, "Modeling of Phase Change Memory: Nucleation, Growth and Amorphization Dynamics during Set and Reset: Part II – Discrete Grains," *IEEE Trans. Electron Devices*, 2017 (Accepted).

[18] L. Adnane, H. Silva, and A. Gokirmak. "High temperature Hall measurement setup for thin film characterization" Review of Scientific Instruments 87, no. 7 (2016): 075117.

[17] F. Dirisaglik, G. Bakan, Z. Jurado, S. Muneer, M. Akbulut, J. Rarey, L. Sullivan, M. Wennberg, A. King, L. Zhang, R. Nowak, C. Lam, H. Silva and A. Gokirmak, "High speed, high temperature electrical characterization of phase change materials: metastable phases, crystallization dynamics, and resistance drift," *Nanoscale, 2015,7, 16625-16630 (*2015).

[16] L. Adnane, N. Williams, H. Silva, and A. Gokirmak. "High temperature setup for measurements of Seebeck coefficient and electrical resistivity of thin films using inductive heating." Review of Scientific Instruments 86, no. 10 (2015): 105119.

[15] Nafisa Noor, Luca Lucera, Thomas Capuano, Venkata Manthina, Alexander G. Agrios, Helena Silva, and Ali Gokirmak. "Blue and white light emission from zinc oxide nanoforests." Beilstein journal of nanotechnology 6 (2015): 2463.

[14] Nafisa Noor, Venkata Manthina, Kadir Cil, Lhacene Adnane, Alexander G. Agrios, Ali Gokirmak, and Helena Silva. "Atmospheric pressure microplasmas in ZnO nanoforests under high voltage stress." AIP Advances 5, no. 9 (2015): 097212.

[13] F. Dirisaglik, G. Bakan, A. Faraclas, A. Gokirmak, and H. Silva, "Numerical modeling of thermoelectric Thomson effect in phase change memory bridge structures," *Int. J. High Speed Electron. Syst.*, vol. 23, no. 01n02, p. 1450004, Mar. 2014.

[12] A. Faraclas, G. Bakan, H. Adnane, F. Dirisaglik, N. E. Williams, A. Gokirmak, H. Silva, L. Adnane, F. Dirisaglik, N. E. Williams, A. Gokirmak, and H. Silva, "Modeling of thermoelectric effects in phase change memory cells," *IEEE Trans. Electron Devices*, vol. 61, no. 2, pp. 372–378, Feb. 2014.

[11] G. Bakan, A. Gokirmak, H. Silva, *Suppression of thermoelectric Thomson effect in silicon microwires under large electrical bias and implications for phase-change memory devices, Journal of Applied Physics* 116, 23, 234507 (2014)

[10] F. Dirisaglik, G. Bakan, A. Faraclas, A. Gokirmak, and H. Silva, "Numerical modeling of thermoelectric thomson effect in phase change memory bridge structures," *Int. J. High Speed Electron. Syst.*, vol. 23, no. 01n02, p. 1450004, Mar. 2014.

[9] G. Bakan, A. Gokirmak, H. Silva, "Suppression of thermoelectric Thomson effect in silicon microwires under large electrical bias and implications for phase-change memory devices," Journal of Applied Physics 116, 23, 234507 (2014).

[8] G. Bakan, N. Khan, H. Silva, A. Gokirmak, "High-temperature thermoelectric transport at small scales: generation, transport and recombination of minority carriers," *Scientific Reports* 3, 2724, doi:10.1038/srep02724 (2013).

[7] S. Fischer, C. Osorio, N. Williams, S. Ayas, H. Silva, A. Gokirmak, "Percolation transport and filament formation in nanocrystalline silicon nanowires," *Journal of Applied Physics* 113, 16, 164902 - 164902-5 (2013).

[6] N. Kan'an, A. Faraclas, N. Williams, H. Silva and A. Gokirmak, "Computational Analysis of Rupture Oxide Phase Change Memory Cells", *IEEE Trans. on Electron Devices*, 60, 5, 1649-1655, (2013).

[5] K. Cil, Y. Zhu, J. Li, C. H. Lam, H. Silva, "Assisted cubic to hexagonal phase transition in GeSbTe thin films on silicon nitride," *Thin Solid Films* 536, 216–219, (2013).

[4] G. Bakan, L. Adnane, A. Gokirmak, H. Silva, "Extraction of temperature dependent electrical resistivity and thermal conductivity from silicon microwires self-heated to melting temperature," *Journal of Applied Physics* 112, 063527 (2012).

[3] N. Williams, H. Silva, A. Gokirmak, "Finite Element Analysis of Scaling of Micro Thermoelectric Generators," AIP *Journal of Renewable and Sustainable Energy* 4**,** 043110 (2012).

[2] H. Silva, G. Bakan, A. Cywar, N. Williams, N. Henry, F. Dirisaglik, A. Gokirmak, "Crystallization of silicon microstructures through rapid self-heating for high-performance electronics on arbitrary substrates," *Nanoscience and Nanotechnology Letters* 4, 10, pp. 970-976(7) (2012).

[1] G. Bakan, N. Khan, A. Cywar, K. Cil, M. Akbulut, A. Gokirmak and H. Silva, "Self-heating of silicon microwires: Crystallization and thermoelectric effects," *Journal of Materials Research*, 26: 1061-1071, *Invited Feature Paper* (2011).

## 9. References


[1] E. Pop, D. Mann, Q. Wang, K. Goodson, and H. Dai, "Thermal conductance of an individual single-wall carbon nanotube above room temperature," *Nano Lett.*, vol. 6, no. 1, pp. 96–100, 2006.

[2] Y. C. Tai, C. H. Mastrangelo, and R. S. Muller, "Thermal conductivity of heavily doped low-pressure chemical vapor deposited polycrystalline silicon films," *J. Appl. Phys.*, vol. 63, no. 5, pp. 1442–1447, 1988.

[3] S. Muneer, N. Noor, G. Bakan, Y. Zhu, A. Gokirmak, and H. Silva, "Extraction of Electrical Resistivity and Thermal Conductivity of Self-heated GST Micro-bridges," in *Mat. Res. Soc. Spring Meeting*, 2013.

[4] B. Van Zeghbroeck, "Principles of semiconductor devices [Online]," *Colorado University*, 2011. [Online]. Available: http://ecee.colorado.edu/~bart/book.

[5] M. Lundstrom and R. Schuelke, "Modeling semiconductor heterojunctions in equilibrium," *Solid. State. Electron.*, 1982.

[6] Y. P. Varshni, "Temperature dependence of the energy gap in semiconductors," *Physica*, vol. 34, no. 1, pp. 149–154, 1967.

[7] C. Sah, R. Noyce, and W. Shockley, "Carrier generation and recombination in pn junctions and pn junction characteristics," *Proc. IRE*, 1957.

[8] J. Dziewior and W. Schmid, "Auger coefficients for highly doped and highly excited silicon," *Appl. Phys. Lett.*, vol. 31, no. 5, pp. 346–348, 1977.

[9] Y. Okuto and C. R. Crowell, "Threshold energy effect on avalanche breakdown voltage in semiconductor junctions," *Solid. State. Electron.*, vol. 18, no. 2, pp. 161–168, 1975.

[10] U. Lindefelt, "Heat generation in semiconductor devices," *J. Appl. Phys.*, vol. 75, no. 2, pp. 942–957, 1994.

[11] G. Bakan, N. Khan, H. Silva, and A. Gokirmak, "High-temperature thermoelectric transport at small scales: thermal generation, transport and recombination of minority carriers.," *Sci. Rep.*, vol. 3, p. 2724, 2013.

[12] V. M. Glazov, S. N. Chizhevskaya, and N. N. Glagoleva, *Liquid Semiconductors*. New York: Plenum Press, 1969.

[13] S. Raoux *et al.*, "Phase-change random access memory: A scalable technology," *IBM J. Res. Dev.*, vol. 52, no. 4–5, pp. 465–480, 2008.

[14] H.-S. P. Wong *et al.*, "Phase ChangeMemory," *Proc. IEEE*, vol. 98, no. 12, pp. 2201–2227, 2010.

[15] K. Cil, Y. Zhu, J. Li, C. H. Lam, and H. Silva, "Assisted cubic to hexagonal phase transition in GeSbTe thin films on silicon nitride," *Thin Solid Films*, vol. 536, pp. 216–219, 2013.

[16] G. Bakan, A. Cywar, H. Silva, and A. Gokirmak, "Melting and crystallization of nanocrystalline silicon microwires through rapid self-heating," *Appl. Phys. Lett.*, vol. 94, no. 25, 2009.

[17] K. Cil *et al.*, "Electrical Resistivity of Liquid Based on Thin-Film and Nanoscale Device Measurements," *Electron Devices, IEEE Trans.*, vol. 60, no. 1, pp. 433–437, 2013.

[18] F. Dirisaglik, "High-temperature Electrical Characterization of $Ge_2Sb_2Te_5$ Phase Change Memory Devices," University of Connecticut, 2014.

[19] D. Ielmini and Y. Zhang, "Analytical model for subthreshold conduction and threshold switching in chalcogenide-based memory devices," *J. Appl. Phys.*, vol. 102, p. 54517, 2007.

[20] M. Boniardi, A. Redaelli, and A. Pirovano, "A physics-based model of electrical conduction decrease with time in amorphous Ge2Sb2Te5," *J. Appl.*, 2009.

[21] A. Calderoni, M. Ferro, and D. Ielmini, "A unified hopping model for subthreshold current of phase-change memories in amorphous state," *IEEE Electron Device*, 2010.

[22] M. Wimmer, M. Kaes, C. Dellen, and M. Salinga, "Role of activation energy in resistance drift of amorphous phase change materials," *Front. Phys.*, vol. 2, Dec. 2014.

[23] D. Ielmini and Y. Zhang, "Physics-based analytical model of chalcogenide-based memories for array simulation," *Electron Devices Meet. 2006. IEDM'06.*, 2006.

[24] G. Burr, P. Tchoulfian, and T. Topuria, "Observation and modeling of polycrystalline grain formation in Ge2Sb2Te5," *J. Appl.*, 2012.

[25] J. P. Simmons, C. Shen, and Y. Wang, "Phase field modeling of simultaneous nucleation and growth by explicitly incorporating nucleation events," *Scr. Mater.*, vol. 10, no. 43, pp. 935–942, 2000.

[26] O. Cueto, V. Sousa, and G. Navarro, "Coupling the Phase-Field Method with an electrothermal solver to simulate phase change mechanisms in PCRAM cells," in *2015 International Conference on Simulation of Semiconductor Processes and Devices (SISPAD)*, 2015.

[27] Z. Fan and D. E. Laughlin, "Three dimensional crystallization simulation and recording layer thickness effect in phase change optical recording," *Jpn. J. Appl. Phys.*, vol. 42, p. 800, 2003.

[28] Y. Liu, Z. Song, Y. Ling, Y. Gong, and S. Feng, "Three-dimensional numerical simulation of phase-change memory cell with probe like bottom electrode structure," *Jpn. J. Appl. Phys.*, vol. 48, no. 2R, p. 24502, Feb. 2009.

[29] A. Faraclas *et al.*, "Modeling of Thermoelectric Effects in Phase Change Memory Cells," *IEEE Trans. Electron Devices*, vol. 61, no. 2, pp. 372–378, Feb. 2014.

[30] P. M. Cells *et al.*, "Computational Analysis of Rupture-Oxide," vol. 60, no. 5, pp. 1649–1655, 2013.

[31] A. Cywar, A. Gokirmak, and H. Silva, "Finite element modeling of a nanowire-based oscillator achieved through solid-liquid phase switching for GHz operation," in *Solid-State Electronics*, 2012, vol. 78, pp. 97–101.

[32] F. Dirisaglik *et al.*, "High speed, high temperature electrical characterization of phase change materials: metastable phases, crystallization dynamics, and resistance drift," *Nanoscale*, vol. 7, no. 40, pp. 16625–16630, 2015.

[33] F. Dirisaglik, G. Bakan, A. Faraclas, A. Gokirmak, and H. Silva, "Numerical Modeling of Thermoelectric Thomson Effect in Phase Change Memory Bridge Structures," *Int. J. High Speed Electron. Syst.*, vol. 23, no. 1, p. 1450004, 2014.

[34] A. Faraclas, N. Williams, A. Gokirmak, and H. Silva, "Modeling of set and reset operations of phase-change memory cells," *IEEE Electron Device Lett.*, vol. 32, no. 12, pp. 1737–1739, 2011.

[35] L. Adnane, N. Williams, and H. Silva, "High temperature setup for measurements of Seebeck coefficient and electrical resistivity of thin films using inductive heating," *Rev. Sci.*, 2015.

[36] J. a. Kalb, M. Wuttig, and F. Spaepen, “Calorimetric measurements of structural relaxation and glass transition temperatures in sputtered films of amorphous Te alloys used for phase change recording,” *J. Mater. Res.*, vol. 22, no. 3, pp. 748–754, 2007.

[37] A. Faraclas, N. Williams, F. Dirisaglik, K. Cil, A. Gokirmak, and H. Silva, “Operation Dynamics in Phase-Change Memory Cells and the Role of Access Devices,” in *VLSI (ISVLSI), 2012 IEEE Computer Society Annual Symposium on*, 2012, pp. 78–83.

[38] J. Y. W. Seto, “The electrical properties of polycrystalline silicon films,” *J. Appl. Phys.*, vol. 46, p. 5247, 1975.

[39] L. Adnane, F. Dirisaglik, M. Akbulut, and Y. Zhu, “High temperature seebeck coefficient and electrical resistivity of Ge2Sb2Te5 thin films,” *APS Meet.*, 2012.

[40] J. A. Kalb, “Crystallization kinetics in antimony and tellurium alloys used for phase change recording,” Ph.D. dissertation. I. Physikalisches Institut der Rheinisch-Westfälische Technische Hochschule (RWTH) Aachen, 52056 Aachen, Germany, 2006.

[41] J. M. Robertson and A. E. Owen, “Electronically-assisted thermal breakdown in chalcogenide glass,” *J. Non. Cryst. Solids*, vol. 8, no. 10, pp. 439–444, 1972.

[42] L. Adnane, N. Williams, H. Silva, and A. Gokirmak, “High temperature setup for measurements of Seebeck coefficient and electrical resistivity of thin films using inductive heating,” *Rev. Sci. Instrum.*, vol. 86, no. 10, p. 105119, 2015.

[43] G. S. Nolas, J. Sharp, J. Goldsmid, and H. J. Goldsmid, *Thermoelectrics: basic principles and new materials developments*, vol. 45. Springer Science & Business Media, 2013.

[44] R. Wolfe and G. E. Smith, “EFFECTS OF A MAGNETIC FIELD ON THE THERMOELECTRIC PROPERTIES OF A BISMUTH-ANIMONY ALLOY,” *Appl.Phys.Letters*, vol. 1, 1962.

[45] L. Adnane, A. Gokirmak, and H. Silva, “High temperature Hall measurement setup for thin film characterization,” *Rev. Sci. Instrum.*, 2016.

[46] L. J. Van der Pauw, “A method of measuring specific resistivity and Hall effect of discs of arbitrary shape,” *Philips Res.Rep.*, vol. 13, pp. 1–9, 1958.

[47] “https://www.arduino.cc/en/Main/ArduinoBoardMega2560.” .

[48] A. Standard, “No Title,” *F76, 2008," Stand. Test Methods Meas. Resist. Hall Coeff. Determ. Hall Mobil. Single-Crystal Semicond. ASTM Int. West Conshohocken, PA, 2008, DOI 10.1520/F076-08*.

[49] B. J. O’Brien and C. S. Wallace, “Ettingshausen effect and thermomagnetic cooling,” *J. Appl. Phys.*, vol. 29, no. 7, pp. 1010–1012, 1958.

[50] R. A. Lomas, M. J. Hampshire, and R. D. Tomlinson, “A sensitive method of Hall measurement,” *J. Phys. E.*, vol. 5, no. 8, p. 819, 1972.

[51] T. Kato and K. Tanaka, “Electronic Properties of Amorphous and Crystalline Ge2Sb2Te5 Films,” *Jpn. J. Appl. Phys.*, vol. 44, no. 10R, p. 7340, 2005.

[52] I. Friedrich, V. Weidenhof, W. Njoroge, P. Franz, and M. Wuttig, “Structural transformations of GeSbTe films studied by electrical resistance measurements,” *J. Appl. Phys.*, vol. 87, p. 4130, 2000.

[53] D. Fugazza, D. Ielmini, G. Montemurro, and A. L. Lacaita, "Temperature- and time-dependent conduction controlled by activation energy in PCM," in *2010 International Electron Devices Meeting*, 2010, p. 29.3.1-29.3.4.

[54] C. David Wright, M. Armand, and M. M. Aziz, "Terabit-per-square-inch data storage using phase-change media and scanning electrical nanoprobes," *IEEE Trans. Nanotechnol.*, vol. 5, no. 1, pp. 50–61, 2006.

[55] H. K. Lyeo *et al.*, "Thermal conductivity of phase-change material GeSbTe," *Appl. Phys. Lett.*, vol. 89, p. 151904, 2006.

[56] A. Vora-ud *et al.*, "Thermoelectric properties of c-GeSb0.75Te0.5 to h-GeSbTe0.5 thin films through annealing treatment effects," *J. Alloys Compd.*, vol. 649, pp. 380–386, Nov. 2015.

[57] J. Lee, T. Kodama, Y. Won, and M. Asheghi, "Phase purity and the thermoelectric properties of Ge2Sb2Te5 films down to 25 nm thickness," *J. Appl.*, 2012.

[58] T. Siegrist, P. Jost, H. Volker, M. Woda, and P. Merkelbach, "Disorder-induced localization in crystalline phase-change materials," *Nat. Mater.*, 2011.

[59] N. F. Mott and E. A. Davis, *Electronic processes in non-crystalline materials*. 1971.

[60] F. Rao *et al.*, "Investigation of changes in band gap and density of localized states on phase transition for Ge 2 Sb 2 Te 5 and Si 3.5 Sb 2 Te 3 materials," *Acta Mater.*, 2012.

[61] A. Redaelli, A. Pirovano, I. Tortorelli, D. Ielmini, and A. L. Lacaita, "A Reliable Technique for Experimental Evaluation of Crystallization Activation Energy in PCMs," *IEEE Electron Device Lett.*, vol. 29, no. 1, pp. 41–43, Jan. 2008.

[62] M. Cutler, J. Leavy, and R. Fitzpatrick, "Electronic transport in semimetallic cerium sulfide," *Phys. Rev.*, 1964.

[63] G. J. Snyder and E. S. Toberer, "Complex thermoelectric materials," *Nat. Mater.*, vol. 7, no. 2, pp. 105–114, 2008.

[64] J. P. Heremans *et al.*, "Enhancement of Thermoelectric of the Electronic Density of States," *Science (80-. ).*, vol. 321, no. July, pp. 1457–1461, 2008.

[65] D. Shin, D. Lee, and M. Jeong, "Effect of CMP on the Te Segregation in Ge 2 Sb 2 Te 5 Films," *Can. J. Phys.*, vol. 159, no. 3, pp. 349–352, Jul. 2012.

[66] J. Hong and S. Yoon, "Effect of Structural Change on Thermoelectric Properties of the Chalcogenide Ge2Sb2Te5 Thin Films," *ECS J. Solid State Sci. Technol.*, vol. 3, no. 10, pp. P298–P301, 2014.

[67] D. T. Castro *et al.*, "Evidence of the Thermo-Electric Thomson Effect and Influence on the Program Conditions and Cell Optimization in Phase-Change Memory Cells," in *IEEE International Electron Devices Meeting*, 2007, pp. 315–318.

[68] A. Faraclas *et al.*, "Modeling of Thermoelectric Effects in Phase Change Memory Cells," *Electron Devices, IEEE Trans.*, vol. 61, no. 2, pp. 372–378, Feb. 2014.

[69] K. Cil, "Temperature Dependent Characterization and Crystallization Dynamics of Ge2Sb2Te5 Thin Films and Nanoscale Structures," *Dr. Diss.*, 2015.

[70] Lord Rayleigh, "LVI. On the Infuence of Obstacles arranged in Rectangular Order upon the Properties of a Medium.," *London, Edinburgh, Dublin Philos. Mag. J. Sci.*, vol. 34, no. 211, pp.

481–502, 1892.

[71] O. Wiener, “Lamellare doppelbrechung,” *Phys. Z* , vol. 5, pp. 332–338, 1904.

[72] D. A. G. Bruggeman, “Berechnung verschiedener physikalischer Konstanten von heterogenen Substanzen. I. Dielektrizitätskonstanten und Leitfähigkeiten der Mischkörper aus isotropen Substanzen,” *Ann. Phys.*, vol. 416, no. 7, pp. 636–664, 1935.

[73] R. Landauer, “The electrical resistance of binary metallic mixtures,” *J. Appl. Phys.*, 1952.

[74] D.-H. Kim, F. Merget, M. Laurenzis, P. H. Bolivar, and H. Kurz, “Electrical percolation characteristics of Ge[sub 2]Sb[sub 2]Te[sub 5] and Sn doped Ge[sub 2]Sb[sub 2]Te[sub 5] thin films during the amorphous to crystalline phase transition,” *J. Appl. Phys.*, vol. 97, no. 8, p. 83538, 2005.

[75] R. C. McPhedran and D. R. McKenzie, “The Conductivity of Lattices of Spheres. I. The Simple Cubic Lattice,” *Proc. R. Soc. A Math. Phys. Eng. Sci.*, vol. 359, no. 1696, pp. 45–63, 1978.

[76] S. Lee, Y. Jung, and R. Agarwal, “Size-dependent surface-induced heterogeneous nucleation driven phase-change in Ge2Sb2Te5 nanowires,” *Nano Lett.*, 2008.

[77] N. Bogoslovskij and K. Tsendin, “Electronic–thermal switching and memory in chalcogenide glassy semiconductors,” *J. Non. Cryst. Solids*, 2011.

[78] K. Cil, “Temperature Dependent Characterization and Crystallization Dynamics of Ge2Sb2Te5 Thin Films and Nanoscale Structures,” 2015.

[79] D. Dimitrov and H.-P. . Shieh, “The influence of oxygen and nitrogen doping on GeSbTe phase-change optical recording media properties,” *Mater. Sci. Eng. B*, vol. 107, no. 2, pp. 107–112, 2004.

[80] N. Kato, I. Konomi, Y. Seno, and T. Motohiro, “In situ X-ray diffraction study of crystallization process of GeSbTe thin films during heat treatment,” *Appl. Surf. Sci.*, vol. 244, no. 1, pp. 281–284, 2005.

[81] Y. Yin, H. Sone, and S. Hosaka, “Dependences of electrical properties of thin GeSbTe and AgInSbTe films on annealing,” *Jpn. J. Appl. Phys.*, vol. 44, p. 6208, 2005.

[82] A. Vora–ud *et al.*, “Power factor investigation of RF magnetron sputtered c-GeSbTe thin film,” *Surf. Coatings Technol.*, vol. 291, pp. 15–20, 2016.

[83] K. S. Bang, Y. J. Oh, and S.-Y. Lee, “Effect of InP Doping on the Phase Transition of Thin GeSbTe Films,” *J. Electron. Mater.*, vol. 44, no. 8, pp. 2712–2718, Aug. 2015.

[84] C.-A. Jong *et al.*, “Mechanical Properties of Phase-change Recording Media: GeSbTe Films,” *Jpn. J. Appl. Phys.*, vol. 40, no. Part 1, No. 5A, pp. 3320–3325, May 2001.

[85] A. L. Patterson, “The Scherrer Formula for X-Ray Particle Size Determination,” *Phys. Rev.*, vol. 56, no. 10, pp. 978–982, Nov. 1939.

[86] J. I. Langford, A. J. C. Wilson, and IUCr, “Scherrer after sixty years: A survey and some new results in the determination of crystallite size,” *J. Appl. Crystallogr.*, vol. 11, no. 2, pp. 102–113, Apr. 1978.

[87] B. Cullity, “Elements of X-ray Diffraction,” 2001.

[88] Y. Hu *et al.*, “Ge 2 Sb 2 Te 5 /Sb superlattice-like thin film for high speed phase change memory

application," *Appl. Phys. Lett.*, vol. 107, no. 26, p. 263105, Dec. 2015.

[89] Y.-H. Huang, Y.-J. Huang, and T.-E. Hsieh, "A study of phase transition behaviors of chalcogenide layers using in situ alternative-current impedance spectroscopy," *J. Appl. Phys.*, vol. 111, no. 12, p. 123706, 2012.

[90] J. Sonntag, "Thermoelectric power in alloys with phase separation (composites).," *J. Phys. Condens. Matter*, 2009.

[91] H.-K. Lyeo *et al.*, "Thermal conductivity of phase-change material Ge[sub 2]Sb[sub 2]Te[sub 5]," *Appl. Phys. Lett.*, vol. 89, no. 15, p. 151904, 2006.

[92] N. Noor *et al.*, "Atmospheric pressure microplasmas in ZnO nanoforests under high voltage stress," *AIP Adv.*, vol. 5, no. 9, p. 97212, 2015.

[93] N. Noor, L. Lucera, and T. Capuano, "Blue and white light emission from zinc oxide nanoforests," *Beilstein J.*, 2015.

[94] D. Kohl, M. Henzler, and G. Heiland, "Low temperature sublimation processes from clean cleaved polar surfaces of zinc oxide crystals during first heating," *Surf. Sci.*, vol. 41, no. 2, pp. 403–411, 1974.

[95] K. Ellmer, A. Klein, and B. Rech, *Transparent conductive zinc oxide: basics and applications in thin film solar cells*, vol. 104. Berlin, Germany: Springer, 2007.

[96] Ü. Özgür *et al.*, "A comprehensive review of ZnO materials and devices," *J. Appl. Phys.*, vol. 98, no. 4, p. 41301, 2005.

[97] K. Tachibana, "Current status of microplasma research," *IEEJ Trans. Electr. Electron.*, 2006.

[98] M. Laroussi, *Plasma medicine: applications of low-temperature gas plasmas in medicine and biology*. 2012.

[99] M. Laroussi, "Low Temperature Plasma-Based Sterilization: Overview and State-of-the-Art," *Plasma Process. Polym.*, vol. 2, no. 5, pp. 391–400, 2005.

[100] E. Stoffels, Y. Sakiyama, and D. B. Graves, "Cold atmospheric plasma: charged species and their interactions with cells and tissues," *Plasma Sci. IEEE Trans.*, vol. 36, no. 4, pp. 1441–1457, 2008.

[101] C. Jiang *et al.*, "Pulsed atmospheric-pressure cold plasma for endodontic disinfection," *Plasma Sci. IEEE Trans.*, vol. 37, no. 7, pp. 1190–1195, 2009.

[102] J. G. Eden, S. J. Park, C. M. Herring, and J. M. Bulson, "Microplasma light tiles: thin sheet lamps for general illumination," *J. Phys. D. Appl. Phys.*, vol. 44, no. 22, p. 224011, 2011.

[103] K. Saji, N. Joshy, and M. Jayaraj, "Optical emission spectroscopic studies on laser ablated zinc oxide plasma," *J. Appl. Phys.*, 2006.

[104] F. Claeyssens, A. Cheesman, S. J. Henley, and M. N. R. Ashfold, "Studies of the plume accompanying pulsed ultraviolet laser ablation of zinc oxide," *J. Appl. Phys.*, vol. 92, no. 11, pp. 6886–6894, 2002.

[105] M. Hanif, M. Salik, and M. A. Baig, "Laser based optical emission studies of zinc oxide (ZnO) plasma," *Plasma Chem. Plasma Process.*, vol. 33, no. 6, pp. 1167–1178, 2013.

[106] N. Noor, V. Manthina, H. Silva, A. G. Agrios, and A. Gokirmak, "Blue and White Light Emission from ZnO Nanoforests," in *Mat. Res. Soc. Fall Meeting*, 2014, vol. O9.04.

[107] N. Noor, T. Capuano, V. Manthina, H. Silva, A. G. Agrios, and A. Gokirmak, “Plasma in a ZnO Nano-Forest: Electrical Discharge, and Blue and White Light Emission,” in *8th International Workshop on Zinc Oxide and Related Materials*, 2014, p. I11.

[108] N. Noor, V. Manthina, K. Cil, A. G. Agrios, H. Silva, and A. Gokirmak, “Blue and White Light Emission from ZnO Nanoforest Microplasmas,” in *24th Annual CMOC Symposium*, 2015.

[109] L. Lucera *et al.*, “Light emission from electrically stressed ZnO nanorods,” *Bull. Am. Phys. Soc.*, vol. 57, 2012.

[110] P. Hari, M. Baumer, W. Tennyson, and L. Bumm, “ZnO nanorod growth by chemical bath method,” *J. Non-Crystalline*, 2008.

[111] M. Willander *et al.*, “Luminescence from zinc oxide nanostructures and polymers and their hybrid devices,” *Materials (Basel).*, vol. 3, no. 4, pp. 2643–2667, 2010.

[112] D. Pavia, G. Kriz, G. Lampman, and R. Engel, *A small scale approach to organic laboratory techniques*. Cengage Learning, 2015.

[113] Y. Ryu *et al.*, “Next generation of oxide photonic devices: ZnO-based ultraviolet light emitting diodes,” *Appl.Phys.Lett.*, vol. 88, p. 241108, 2006.

[114] A. Tsukazaki *et al.*, “Blue light-emitting diode based on ZnO,” *Jpn. J. Appl. Phys.*, vol. 44, no. 5L, p. L643, 2005.

[115] X. Zhang, M. Lu, Y. Zhang, L. Chen, and Z. L. Wang, “Fabrication of a High-Brightness Blue-Light-Emitting Diode Using a ZnO-Nanowire Array Grown on p-GaN Thin Film,” *Adv. Mater.*, vol. 21, no. 27, pp. 2767–2770, 2009.

[116] A. Baltakesmez, S. Tekmen, and S. Tüzemen, “ZnO homojunction white light-emitting diodes,” *J. Appl. Phys.*, vol. 110, no. 5, p. 54502, 2011.

[117] I. I. Sobelman, *Atomic spectra and radiative transitions*. Springer-Verlag Berlin, 1979.

[118] R. Siegel, *Thermal radiation heat transfer*, vol. 1. CRC press, 2001.

[119] J. Eden and S. Park, “Microcavity plasma devices and arrays: A new realm of plasma physics and photonic applications,” *Plasma Phys. Control. fusion*, 2005.